

---

# Polynomial Neural Sheaf Diffusion: A Spectral Filtering Approach on Cellular Sheaves

---

Alessio Borgi<sup>1,2</sup> Fabrizio Silvestri<sup>1</sup> Pietro Liò<sup>2</sup>

## Abstract

Sheaf Neural Networks (SheafNNs) equip graphs with local vector spaces and learnable transport maps, offering a principled inductive bias for heterophily and oversmoothing. Yet, current Neural Sheaf Diffusion (NSD) remains largely *spatial*: it depends on SVD-based normalisation and dense per-edge restriction maps, making computation and optimisation brittle and tightly coupled to stalk dimension. We propose *Polynomial Neural Sheaf Diffusion (PolyNSD)*, the first SheafNN framework to perform diffusion *explicitly in the spectral domain*, being a *model-agnostic* operator applicable across all sheaf neural network variants. PolyNSD models propagate as a degree- $K$  polynomial of a normalised sheaf Laplacian, evaluated via a stable three-term recurrence on a spectrally rescaled operator. This yields an explicit  $K$ -hop receptive field in a single layer and a directly learnable spectral response via convex combinations of orthogonal polynomial filters. We further include *PolySpectralGNN*, a matched polynomial-spectral non-sheaf baseline mirroring PolyNSD’s spectral operator. Across homophilic and heterophilic benchmarks, PolyNSD achieves state-of-the-art performance while overturning the prevailing NSD paradigm: it reaches these results using only diagonal restriction maps, decoupling accuracy from large stalk dimensions and substantially reducing runtime and memory. We validate PolyNSD across polynomial families, heterophily levels, and present continuous-domain extensions, oversmoothing diagnostics, oversquashing probes via long-range influence decay, and spectral interpretability analyses.

---

<sup>1</sup>Department of Computer, Control and Management Engineering, Sapienza University, Rome, Italy <sup>2</sup>Department of Computer Science and Technology, University of Cambridge, Cambridge, United Kingdom. Correspondence to: Alessio Borgi <alessio.borgi@uniroma1.it, ab3352@cam.ac.uk>.

Preprint. February 4, 2026.

## 1. Introduction

Graph Neural Networks (GNNs) Goller & Kuchler (1996); Gori et al. (2005); Scarselli et al. (2008); Bruna et al. (2013); Defferrard et al. (2016); Velickovic et al. (2017); Gilmer et al. (2017) have become a standard tool for learning on relational data, yet they often underperform on *heterophilic* graphs (Zhu et al., 2020) and suffer from *oversmoothing* (Nt & Maehara, 2019; Rusch et al., 2023) when stacked deeply.

A possible solution provided by (Bi et al., 2024) is to modify the graph by rewiring the graph with homophilic edges and pruning heterophilic ones. A more principled way to avoid that, modeling heterophily in the graph’s underlying topology, is via (cellular) *sheaves* (Hansen & Gebhart, 2020; Bodnar et al., 2022): each node/edge carries a local feature space (a stalk) and edges carry linear restriction maps that specify how to align and compare features across incidences. The resulting sheaf Laplacian implements *transport-aware* diffusion that can better accommodate heterophily than conventional, isotropic graph filters. However, existing neural sheaf–diffusion layers are (i) effectively one-step propagators, (ii) rely on dense, per-edge restriction maps, (iii) require heavy normalizations or even decompositions during training, and (iv) their performance is highly dependent on the stalk’s high-dimensionality. These factors inflate parameters and runtime, couple cost and stability to the stalk dimension, and can yield brittle optimization.

We propose *Polynomial Neural Sheaf Diffusion (PolyNSD)*, which reframes neural sheaf diffusion as an explicit *spectral filtering* problem. Instead of single-step spatial updates, PolyNSD applies a learnable degree- $K$  polynomial filter of a spectrally rescaled sheaf Laplacian, evaluated via stable  $K$ -term recurrences (e.g., Chebyshev). This construction provides an explicit  $K$ -hop receptive field within a single layer and enables direct control over the diffusion behaviour (low-, band-, or high-pass). We ensure stability through spectral rescaling and convex combinations of the  $K+1$  polynomial basis responses, yielding a non-expansive propagation operator, while residual and gated pathways preserve gradient flow at depth. PolyNSD is also *parameter-efficient*: propagation is governed by only  $K+1$  scalar coefficients per layer, and reusing the learned sheaf transports, avoids dense per-edge restriction maps. For these reasons, with PolyNSD,

we manage to decouple performance from large stalk dimensions, reducing memory and runtime, while retaining the transport-aware inductive bias that mitigates oversmoothing on challenging heterophilic graphs.

**Contributions.** Our main contributions are as follows:

1. We introduce *Polynomial Neural Sheaf Diffusion (PolyNSD)*, the first sheaf-diffusion framework formulated *explicitly in the spectral domain*. PolyNSD applies orthogonal-polynomial filters to a spectrally rescaled sheaf Laplacian via stable recurrences, is *model-agnostic*, and easy to plug into existing SheafNN architectures.
2. We achieve *state-of-the-art* performance across homophilic and heterophilic benchmarks and, through ablations, demonstrate consistent gains from higher-order filters ( $K > 1$ ) over first-order NSD. We also introduce *PolySpectralGNN*, a non-sheaf baseline using the same polynomial filtering on the standard graph operator, to disentangle sheaf-specific gains from spectral filtering effects.
3. We show that *diagonal restriction maps*, combined with spectral polynomial filtering, are sufficient to match or surpass prior sheaf models, decoupling accuracy from large stalk dimensions and reducing parameters, memory, and runtime.
4. We provide a comprehensive empirical and diagnostic study, including polynomial-order and spectral-scaling ablations, depth/oversmoothing analyses, controlled synthetic stress tests (heterophily, scale, feature noise), and continuous-time extensions via neural sheaf ODEs. We further probe oversquashing via long-range influence decay and analyse learned frequency responses for spectral interpretability.

## 2. Background and Related Works

**Sheaf Neural Networks, Heterophily and Oversmoothing.** GNNs have evolved from early message-passing formulations to a family of architectures that trade off locality, expressivity, and efficiency. Canonical baselines include spectral and spatial convolutions (Defferrard et al., 2016; Bruna et al., 2013; Kipf & Welling, 2016), attention mechanisms (Velickovic et al., 2017), principled aggregates (Gilmer et al., 2020) and transformer-based versions (Yun et al., 2019; Dwivedi & Bresson, 2020). Despite this progress, two persistent pathologies limit standard GNNs. The former, *Oversmoothing* arises as layers deepen, since repeated low-pass propagation collapses node features toward a near-constant signal, eroding class margins and yielding accuracy drop-offs beyond shallow depth (Nt &

Maehara, 2019; Rusch et al., 2023). *Heterophily* further stresses isotropic message passing: when adjacent nodes belong to different classes or carry contrasting attributes, the averaging operation blurs the high-frequency signals that separate classes, and performance degrades as homophily decreases (Zhu et al., 2020). These phenomena are tightly linked in practice and motivate transport-aware architectures that decouple *who* communicates from *how* features are compared.

**Sheaf Neural Networks.** Cellular sheaf theory (Shepard, 1985; Curry, 2014) equips graphs with local feature spaces (stalks) and linear restriction/transport maps on edges, enabling transport-aware diffusion that can better handle heterophily than isotropic message passing. Sheaf Neural Networks, originally introduced using an hand-crafted sheaf with a single dimensionality in (Hansen & Gebhart, 2020) and further improved by allowing to learn the sheaf using a learnable parametric function (Bodnar et al., 2022), demonstrated strong performance under heterophily and against oversmoothing, by instantiating diffusion on the sheaf Laplacian. Subsequent works explored attention on sheaves (Barbero et al., 2022b), learning the graph connection Laplacian directly from data and at preprocessing time (Barbero et al., 2022a), sheaves-based positional encoding (He et al., 2023), introducing non-linearities in the process (Zaghen, 2024), injecting joint diffusion biases (Caralt et al., 2024), handling graph heterogeneity (Braithwaite et al., 2024), sheaf hypergraphs (Duta et al., 2023; Mule et al., 2025) and directional extensions (Fiorini et al., 2025), applications to recommendation systems (Purificato et al., 2023) and federated learning settings (Nguyen et al., 2024), and more general frameworks such as Copresheafs (Hajji et al., 2025).

**Cellular Sheaves on Graphs.** Formally, let  $\mathcal{G} = (\mathcal{V}, \mathcal{E})$  be a finite undirected graph with an arbitrary orientation on edges. A *Cellular Sheaf*  $\mathcal{F}$  on  $\mathcal{G}$  assigns a finite-dimensional inner-product space (the *stalk*)  $\mathcal{F}(v)$  to each vertex  $v \in \mathcal{V}$  and  $\mathcal{F}(e)$  to each edge  $e \in \mathcal{E}$ , together with linear *restriction/transport* maps  $\mathcal{F}_{v \triangleleft e} : \mathcal{F}(v) \rightarrow \mathcal{F}(e), \forall$  incident pair  $v \triangleleft e$ . By stacking the vertex and edge stalks, we can obtain, respectively, the 0- and 1-cochain spaces  $C^0(\mathcal{G}; \mathcal{F}) := \bigoplus_{v \in \mathcal{V}} \mathcal{F}(v), C^1(\mathcal{G}; \mathcal{F}) := \bigoplus_{e \in \mathcal{E}} \mathcal{F}(e)$ . Given the chosen orientation (e.g.,  $e = (u \rightarrow v)$ ), we can use them to construct the *sheaf coboundary*  $\delta : C^0(\mathcal{G}; \mathcal{F}) \rightarrow C^1(\mathcal{G}; \mathcal{F})$ , that acts edgewise as  $\delta(x)_e = \mathcal{F}_{v \triangleleft e} x_v - \mathcal{F}_{u \triangleleft e} x_u$ . Using the co-boundary, one can define the *Sheaf Laplacian* as  $L_{\mathcal{F}} := \delta^T \delta$ , or node-wise as  $L_{\mathcal{F}}(x)_u = \sum_{u, v \triangleleft e} \mathcal{F}_{u \triangleleft e}^T (\mathcal{F}_{u \triangleleft e} x_u - \mathcal{F}_{v \triangleleft e} x_v)$ ,

Its normalised version is obtained by reweighting the sheaf’s inner products as:  $\Delta_{\mathcal{F}} := D^{-1/2} L_{\mathcal{F}} D^{-1/2}$ , where  $D$  is the block diagonal of  $L_{\mathcal{F}}$ .

**Neural Sheaf Diffusion (NSD).** Starting from the same

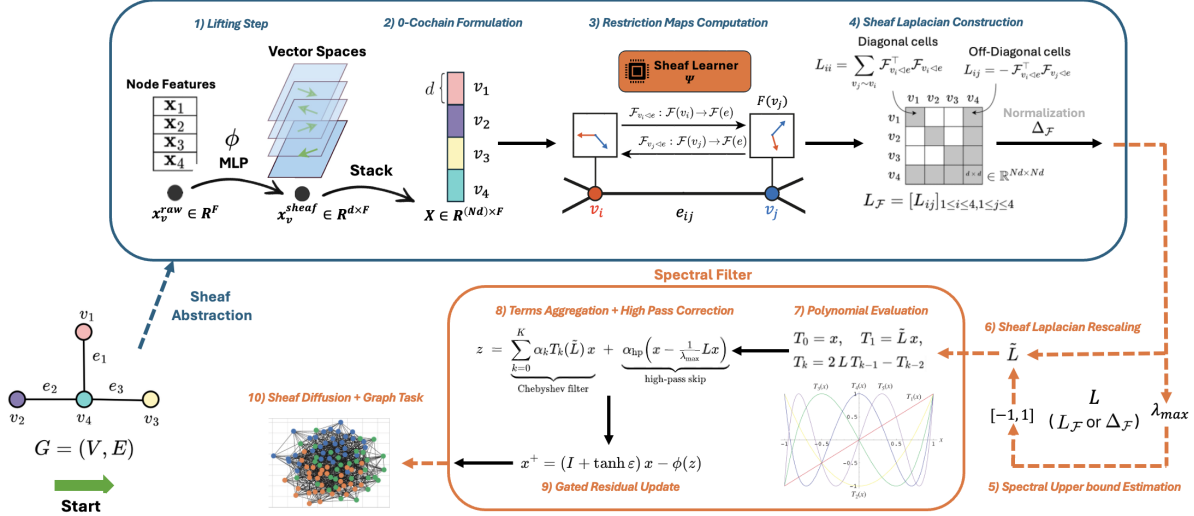


Figure 1. Polynomial Sheaf Neural Network Architecture. Graph’s raw node features are lifted to  $d$ -dimensional stalk signals and stacked into a 0-cochain. A sheaf learner predicts edge-wise restriction maps and defines the vertex sheaf Laplacian  $L$ . PolyNSD then estimates  $\lambda_{\max}$ , rescales  $L$  to  $\tilde{L} \in [-1, 1]$ , and applies a degree- $K$  spectral filter  $p_{\theta}(\tilde{L}) = \sum_{k=0}^K \alpha_k T_k(\tilde{L})$  via a stable three-term recurrence, followed by a lightweight high-pass correction and a gated residual update, yielding explicit  $K$ -hop mixing within a single diffusion layer.

undirected graph  $\mathcal{G}$ , with each node  $u \in \mathcal{V}$  carrying a  $d$ -dimensional feature vector  $x_u \in \mathcal{F}(u)$ , we can stack node features (after a projection to the stalk space), into the column  $x \in C^0(\mathcal{G}; \mathcal{F})$ , and by allowing up to  $f$  feature channels, we can collect them in a matrix  $X \in \mathbb{R}^{nd \times f}$ . Following (Bodnar et al., 2022), the edge-wise restriction/transport maps that define the sheaf at layer (or time)  $t$  are computed from incident node features via a learnable function. For  $e = (u, v)$ , we have  $\mathcal{F}_{u \leq e}^{(t)} = \Phi^{(t)}(x_u, x_v)$ ,  $\mathcal{F}_{v \leq e}^{(t)} = \Phi^{(t)}(x_v, x_u)$ , where, typically,  $F_{u \leq e}^{(t)} = \Phi^{(t)}(x_u, x_v) = \text{MLP}(x_u || x_v)$  and similarly for  $F_{v \leq e}^{(t)}$ . These can produce matrices of the appropriate shape (diagonal, bundle, or general), that can be used to build the sheaf Laplacian ( $L_{\mathcal{F}}^{(t)}$  or  $\Delta_{\mathcal{F}}^{(t)}$ ) and perform a sheaf-aware diffusion step on  $X$  as:  $X^{(t+1)} = X^{(t)} - \sigma(\Delta_{\mathcal{F}}^{(t)}(I_{nd} \otimes W_1^{(t)}) X^{(t)} W_2^{(t)})$ , where  $W_1^{(t)}$  and  $W_2^{(t)}$  are trainable weight matrices,  $I_{nd}$  is the identity,  $\otimes$  denotes the Kronecker product, and  $\sigma(\cdot)$  is a nonlinearity. Sheaf Diffusion replaces standard graph diffusion by measuring disagreements *after* transporting node features into each edge’s discourse space, and then aggregating them back to nodes via the sheaf Laplacian.

**Spectral and Polynomial Graph Filters.** A large body of approaches for GNNs, designs filters in the spectrum of the graph Laplacian, from early spectral CNNs and graph wavelets (Bruna et al., 2013; Hammond et al., 2011; Shuman et al., 2013) to localized polynomial approximations that avoid explicit eigen-decompositions (Defferrard et al., 2016; Kipf & Welling, 2016). Chebyshev-style recurrences and related rational/polynomial filters offer stable, scalable propagation and interpretable frequency responses (Levie

et al., 2018; Bianchi et al., 2021). Further developments include Lanczos-based personalized PageRank diffusion and precomputed multi-hop schemes (Liao et al., 2019; Klicpera et al., 2019; Wu et al., 2019; Rossi et al., 2020; Chien et al., 2021). These ideas established that multi-hop context and frequency selectivity can be achieved with sparse matrix–vector primitives instead of decompositions. Our work adopts this philosophy, but lifts it from the graph Laplacian to the *sheaf* Laplacian.

### 3. Polynomial Neural Sheaf Diffusion

**Problem Setting & Architectural Overview.** Polynomial Neural Sheaf Diffusion (PolyNSD) is a transport-aware graph neural architecture that performs feature propagation through a spectrally parameterised diffusion step on a learned sheaf Laplacian. Let  $G = (V, E)$  be a graph with  $N = |V|$  nodes and raw features  $\{x_v^{\text{raw}} \in \mathbb{R}^F\}_{v \in V}$ . As illustrated in Figure 1, PolyNSD first applies a lifting map  $\phi$  to embed each node into a  $d$ -dimensional stalk,  $x_v = \phi(x_v^{\text{raw}}) \in \mathbb{R}^{d \times F}$ , and stacks these into a 0-cochain  $x \in C^0(G; \mathcal{F}) \cong \mathbb{R}^{(Nd) \times F}$  (steps 1-3). A parametric sheaf learner  $\Psi$  (step 4) then predicts edge-wise restriction/transport maps  $\{\mathcal{F}_{v \leq e}\}$  (diagonal / bundle / general), which defines a symmetric positive semidefinite (vertex) sheaf Laplacian  $L \in \mathbb{R}^{Nd \times Nd}$  (either unnormalised  $L_{\mathcal{F}}$  or degree-normalised  $\Delta_{\mathcal{F}}$ ), which is the fundamental propagation primitive of sheaf neural networks measuring disagreement after transport into shared edge spaces and aggregating it back to nodes. In Neural Sheaf Diffusion (NSD) (Bodnar et al., 2022), feature propagation is implemented through a first-order diffusion operator of the form  $x \mapsto (aI + bL)x$ ,

applied repeatedly across layers. In our case, instead of applying this Laplacian through repeated local diffusion steps, PolyNSD evaluates a learnable degree- $K$  polynomial spectral filter in one shot (steps 5-10), yielding explicit  $K$ -hop mixing with controllable frequency response. The resulting filtered signal is stabilised via a lightweight high-pass correction and a gated residual update. This design decouples long-range propagation from network depth, exposes the diffusion process as an interpretable spectral operator, and remains fully compatible with existing sheaf learners and transport classes. More detailed and further explanations on the single steps can be found in [Appendix B](#).

**From Spatial Diffusion to Spectral Control.** While effective, first-order sheaf diffusion inherits two structural limitations shared by standard message-passing schemes. First, long-range interactions require stacking many layers, increasing computational cost and intensifying the over-smoothing phenomenon. Second, the spectral response of the operator is implicitly fixed: repeated applications of  $(aI + bL)$  primarily realise low-pass filtering, limiting control over which frequency components of the sheaf signal are preserved, attenuated, or amplified. We address these concerns with *PolyNSD*, by moving from a *spatial* to a *spectral* formulation of sheaf diffusion. Instead of repeatedly applying a local operator, we design a transport-aware propagation step whose action is explicitly parameterised in the spectrum of the sheaf Laplacian. This shift enables long-range mixing within one layer and exposes the diffusion process as a controllable frequency-selective operator, laying the foundation for interpretable and task-adaptive sheaf propagation. Please refer from [Appendix subsection A.1](#) to [subsection A.4](#) for further details, proofs, and explanations about *Spectral Theory* extended to *Sheaf Theory*.

**Polynomial Filters on Sheaf Laplacians.** *Polynomial Neural Sheaf Diffusion (PolyNSD)* replaces the one-step NSD diffusion core with a *learnable spectral filter* defined as a degree- $K$  polynomial in the sheaf Laplacian:

$$p(L) = \sum_{k=0}^K c_k L^k, \quad y = p(L) x \quad (1)$$

with scalar coefficients  $\{c_k\}_{k=0}^K$  shared across nodes and stalk coordinates. Since  $L$  is real symmetric PSD, there exists an eigendecomposition  $L = U\Lambda U^\top$  with  $\Lambda = \text{diag}(\lambda_1, \dots, \lambda_{nd})$  and an orthonormal basis  $U$  of *sheaf Fourier modes*. By the polynomial functional calculus, we have  $p(L) = U p(\Lambda) U^\top$ , with  $p(\Lambda) = \text{diag}(p(\lambda_1), \dots, p(\lambda_{nd}))$ . Here,  $p$  acts as a *scalar spectral multiplier*  $p(\lambda) = \sum_{k=0}^K c_k \lambda^k$  that scales the  $i$ -th sheaf Fourier mode by  $p(\lambda_i)$ , directly controlling the layer's frequency response (low-/band-/high-pass). In view of the Dirichlet-energy identity  $\langle x, Lx \rangle = \sum_i \lambda_i \hat{x}_i^2$ , designing

$p(\lambda)$  decreasing in  $\lambda$  emphasises smooth, globally aligned sheaf signals, while band-pass or high-pass choices selectively retain or amplify disagreement patterns. This extends the spectral theory of cellular sheaves ([Hansen & Ghrist, 2019](#)) to *learnable* filters and also connects with the opinion-dynamics interpretation for which PolyNSD layers implement data-driven operators  $p(L)$  that explicitly shape how agreement and disagreement propagate across the sheaf.

**K-hop Locality.** From a spatial perspective, [Equation 1](#) has an explicit  $K$ -hop receptive field: multiplying by  $L$  propagates information across edges, while  $L^k$  involves paths of length up to  $k$ . A single PolyNSD layer achieves  $K$ -hop mixing without stacking  $K$  message-passing steps.

**Proposition 1.** *Let  $L$  be a sparse block Laplacian on a graph  $G = (V, E)$  such that the off-diagonal block  $(v, u)$  is nonzero only when  $(v, u) \in E$ , and diagonal blocks are arbitrary PSD. Let  $p(L)$  be as in [Equation 1](#), then:  $(p(L))_{vu} = 0$  whenever  $\text{dist}_G(v, u) > K$ . (See proof in [Appendix subsection A.5](#)).*

**Commutation and Dirichlet Energy.** Polynomial filters in  $L$  enjoy two structural properties that make them natural diffusion operators. First, any two such filters share the same eigenbasis and therefore commute: composing  $p(L)$  and  $q(L)$  is equivalent to applying a single polynomial  $(pq)(L)$ . This translates to the fact that if we stack linear PolyNSD layers without nonlinearities or parameter changes does not create a new operator types beyond a higher-degree polynomial in  $L$ . Second, if the scalar multiplier  $p(\lambda)$  is pointwise bounded by  $0 \leq p(\lambda) \leq 1$  on the spectrum, then  $p(L)$  can only decrease the Dirichlet energy, meaning that it damps disagreement modes and never amplifies them.

**Proposition 2.** *Let  $L$  be a symmetric PSD sheaf Laplacian and  $p, q$  be real polynomials. Then:  $p(L)q(L) = q(L)p(L) = (pq)(L)$ . Moreover, if  $L = U\Lambda U^\top$ ,  $x = U\hat{x}$  and  $p(\lambda)$  satisfies  $0 \leq p(\lambda) \leq 1$  on  $\sigma(L)$ , then:*

$$\begin{aligned} \langle p(L)x, Lp(L)x \rangle &= \sum_{i=1}^{nd} \lambda_i p(\lambda_i)^2 \hat{x}_i^2 \\ &\leq \sum_{i=1}^{nd} \lambda_i \hat{x}_i^2 = \langle x, Lx \rangle \end{aligned} \quad (2)$$

(See proof in [Appendix subsection A.5](#)).

**Choice of Basis and Chebyshev Parameterisation.** Directly learning the monomial coefficients  $\{c_k\}$  in [Equation 1](#) is theoretically sound but, at the same time, numerically fragile since the associated Vandermonde systems are exponentially ill-conditioned in  $K$  on any nontrivial interval. We therefore decide to follow classical spectral-approximation practice and expand  $p$  in an *orthogonal polynomial basis* on

a compact interval. More in concrete, let  $\sigma(L) \subset [0, \lambda_{\max}]$  and define the affine rescaling:

$$\tilde{L} = \frac{2}{\lambda_{\max}} L - I, \quad \sigma(\tilde{L}) \subset [-1, 1] \quad (3)$$

Here,  $\lambda_{\max}$  denotes the spectrum of  $L$  upper-bound, and can be set in this way: for the degree-normalised sheaf Laplacian  $\Delta_{\mathcal{F}}$  we use the canonical bound  $\lambda_{\max} = 2$ , while for the unnormalised  $L_{\mathcal{F}}$  we either adopt a fast Gershgorin-type analytic bound or a short power iteration (see further in Appendix subsection B.4). This rescaling is a structural requirement for Chebyshev parameterisations. First-kind Chebyshev polynomials, in particular, satisfy  $T_k(\xi) = \cos(k \arccos \xi)$  for  $|\xi| \leq 1$ , hence  $|T_k(\xi)| \leq 1$  on  $[-1, 1]$ , while for  $|\xi| > 1$  they grow exponentially. By operating in the regime where  $|T_k(\xi)| \leq 1$ , convex mixtures of  $\{T_k\}$  induce uniformly bounded spectral multipliers and, in turn, stable diffusion operators. More generally, we can then write  $p$  as follows:

$$p(\lambda) = \sum_{k=0}^K \theta_k B_k(\xi(\lambda)), \quad \xi(\lambda) = \frac{2}{\lambda_{\max}} \lambda - 1 \quad (4)$$

where  $\{B_k\}_{k=0}^K$  is an orthogonal basis (not necessarily a Chebyshev-based one) on  $[-1, 1]$  (see Appendix subsection A.6), and  $K$  indicates the degree of the polynomial. In our default instantiation we choose first-kind Chebyshev polynomials  $B_k(\xi) = T_k(\xi)$ , and parameterise  $\theta$  as a *convex mixture* via  $\theta = \text{softmax}(\eta)$ ,  $\eta \in \mathbb{R}^{K+1}$ . However, the implementation is basis-agnostic, and other polynomials can be employed as well.

**High-Pass Skip and Gated Residual.** To mitigate the intrinsic low-pass bias of diffusion, we augment the polynomial response with a *high-pass correction* and a *gated residual*. Given  $\lambda_{\max}$  and  $L$  we define:

$$h_{\text{hp}} = x - \lambda_{\max}^{-1} Lx, \quad z = p_{\theta}(\tilde{L})x + \alpha_{\text{hp}} h_{\text{hp}} \quad (5)$$

with learned scalar  $\alpha_{\text{hp}} \in \mathbb{R}$ , and apply a 1-Lipschitz nonlinearity  $\phi$  and a diagonal residual gate  $\varepsilon$ :  $x^+ = (I + \tanh \varepsilon)x - \phi(z)$  Here, since,  $\tilde{L}$  is an affine function of  $L$ , it commutes with  $L$  and shares the same eigenvectors. Writing  $L = U\Lambda U^T$ , the pre-nonlinearity linear map  $x \mapsto p_{\theta}(\tilde{L})x + \alpha_{\text{hp}} h_{\text{hp}}$  acts diagonally in the eigenbasis with per-eigenvalue multiplier  $m(\lambda) = p_{\theta}\left(\frac{2\lambda}{\lambda_{\max}} - 1\right) + \alpha_{\text{hp}}\left(1 - \frac{\lambda}{\lambda_{\max}}\right)$ ,  $\lambda \in \sigma(L)$ . The second term here is a linear spectral profile that can *deform* the polynomial response, by changing low vs. high modes in a controlled and analytically transparent way using a single scalar  $\alpha_{\text{hp}}$ . Moreover, if  $p_{\theta}(\xi) \geq 0$  on  $[-1, 1]$  and  $\alpha_{\text{hp}} > 0$ , then  $m(\lambda) > 0$  for all  $\lambda \in [0, \lambda_{\max})$ , so no non-harmonic mode can be accidentally annihilated by the learned filter.

Speaking instead of the (*global Lipschitz control*) we add for stability, using submultiplicativity,  $\|p_{\theta}(\tilde{L})\|_2 \leq 1$  and  $\|I - \lambda_{\max}^{-1} L\|_2 \leq 1$  whenever  $\lambda_{\max}$  upper-bounds  $\sigma(L)$ , the overall update satisfies the explicit bound and in particular  $\|I + \tanh \varepsilon\|_2 \leq 1 + \|\tanh \varepsilon\|_{\infty}$ . Here,  $\varepsilon$  controls how far the residual branch deviates from the identity, while  $\alpha_{\text{hp}}$  controls how aggressively the spectrum is reshaped, with a *linear and explicit* impact on the worst-case Lipschitz constant. (see further details and proofs in Appendix subsection B.5).

**PolyNSD and NSD Comparison.** PolyNSD is a strict generalisation of Neural Sheaf Diffusion: for  $K=1$  the update reduces to an operator of the form  $aI + bL$  acting on  $x$ , recovering the first-order diffusion step of NSD up to normalisation, while  $K>1$  yields genuine higher-order polynomials in  $L$  with an explicit  $K$ -hop receptive field. A degree- $K$  PolyNSD layer therefore requires  $K$  sparse-dense multiplications with  $L$  (or  $\tilde{L}$ ), for a cost  $O(K \text{nnz}(L) C)$ , matching the asymptotic cost of stacking  $K$  NSD layers but without repeated sheaf prediction and Laplacian re-assembly. (see Appendix subsection B.6 for more details).

**PolySpectralGNN: Polynomial Spectral non-Sheaf Baseline.** To isolate the benefit of *spectral polynomial filtering* from the additional expressivity of learnable sheaf transports, we also introduce a non-sheaf baseline, *PolySpectralGNN*, a model applying the *same Chebyshev polynomial filtering mechanism* used in PolyNSD, but on the *scalar* normalised graph Laplacian. Given adjacency  $\mathbf{A}$  and degree  $\mathbf{D}$ , we form the symmetrically normalised operator  $\mathbf{S} = \mathbf{D}^{-1/2} \mathbf{A} \mathbf{D}^{-1/2}$  and  $\mathbf{L}_{\text{sym}} = \mathbf{I} - \mathbf{S}$ , rescale  $\mathbf{L}_{\text{sym}}$  as  $\tilde{\mathbf{L}} = \frac{2}{\lambda_{\max}} \mathbf{L}_{\text{sym}} - \mathbf{I}$ , and compute the Chebyshev Type-1 iteration. The single layer outputs a learnable mixture  $\sum_{k=0}^K w_k \mathbf{T}_k(\tilde{\mathbf{L}}) \mathbf{h}$ , augmented with a high-pass correction and a gated residual. This means that *PolySpectralGNN* corresponds to the PolyNSD model with stalk dimension = 1 and transport = identity.

## 4. Experimental Evaluation

We evaluate *Polynomial Neural Sheaf Diffusion (PolyNSD)* on standard real-world and synthetic *node-classification* benchmarks, complementing accuracy with additional diagnostics. We probe *oversmoothing* via depth sweeps and Dirichlet-energy trajectories, *oversquashing* via long-range influence decay, assess a *continuous-depth* extension through Neural Sheaf ODEs, and study *spectral interpretability* over the learned frequency responses. These experiments test four claims: (i) strong performance across both homophilic and heterophilic regimes, (ii) improved robustness to increasing depth with reduced oversmoothing, (iii) gains from higher-order spectral filtering ( $K > 1$ ) over first-order diffusion, and (iv) a more favourable accuracy-

Table 1. PolyNSD discrete node classification benchmark results. The top three models for each dataset are coloured by **First**, **Second** and **Third**, respectively.

	Texas	Wisconsin	Film	Squirrel	Chameleon	Cornell	Citeseer	Pubmed	Cora
<i>Homophily level</i>	<b>0.11</b>	<b>0.21</b>	<b>0.22</b>	<b>0.22</b>	<b>0.23</b>	<b>0.30</b>	<b>0.74</b>	<b>0.80</b>	<b>0.81</b>
#Nodes	183	251	7,600	5,201	2,277	183	3,327	18,717	2,708
#Edges	295	466	26,752	198,493	31,421	280	4,676	44,327	5,278
#Classes	5	5	5	5	5	5	7	3	6
<b>DiagPolySD</b>	<b>90.00±4.68</b>	88.63±3.59	37.31±0.98	<b>56.61±2.06</b>	<b>71.45±2.03</b>	<b>86.49±5.54</b>	<b>77.74±1.26</b>	89.70±0.32	<b>88.79±1.13</b>
<b>BundlePolySD</b>	<b>89.74±5.32</b>	<b>89.41±4.04</b>	37.47±0.86	55.76±2.02	<b>71.18±1.46</b>	<b>86.76±4.90</b>	<b>77.57±1.55</b>	<b>89.75±0.34</b>	88.33±1.34
<b>GeneralPolySD</b>	<b>89.21±5.05</b>	88.82±4.89	37.34±1.13	<b>55.79±2.52</b>	69.62±1.85	<b>86.49±5.80</b>	77.21±1.58	89.73±0.41	<b>88.47±1.19</b>
<b>PolySpectralGNN</b>	64.59±6.40	58.62±6.04	25.50±0.85	51.72±1.76	62.65±3.03	54.59±6.26	60.4±0.89	78.7±0.56	76.2±0.67
RiSNN - NoT	87.89±4.28	88.04±2.39	N/A	51.24±1.71	66.58±1.81	82.97±6.17	75.07±1.56	87.91±0.55	85.86±1.31
RiSNN	86.84±3.72	87.84±2.60	N/A	53.30±3.30	65.15±2.40	85.95±6.14	76.23±1.81	88.00±0.42	85.27±1.11
JdSNN - NoW	87.30±4.53	88.43±2.83	N/A	51.28±1.80	66.45±3.46	84.59±6.95	75.93±1.41	88.09±0.49	84.39±1.47
JdSNN	87.37±5.10	<b>89.22±3.42</b>	N/A	49.89±1.71	66.40±2.33	85.41±4.55	73.27±1.86	88.19±0.55	85.43±1.73
Conn - NSD	86.16±2.24	88.73±4.47	<b>37.91±1.28</b>	45.19±1.57	65.21±2.04	85.95±7.72	75.61±1.93	89.28±0.38	83.74±2.19
SAN	84.05±5.33	86.47±3.87	37.09±1.18	50.96±1.40	67.46±1.90	84.32±5.64	72.57±1.50	87.12±0.30	85.90±1.85
ANSD	85.68±4.69	87.45±3.19	37.66±1.40	54.39±1.76	68.38±2.14	84.59±5.93	76.81±1.82	89.21±0.37	87.20±1.03
Diag - NSD	85.67±6.95	88.63±2.75	37.79±1.01	54.78±1.81	68.68±1.73	86.49±7.35	77.14±1.85	89.42±0.43	87.14±1.06
O(d) - NSD	85.95±5.51	<b>89.41±4.74</b>	<b>37.81±1.15</b>	<b>56.34±1.32</b>	68.04±1.58	84.86±4.71	76.70±1.57	89.49±0.40	86.90±1.13
Gen - NSD	82.97±5.13	89.21±3.84	<b>37.80±1.22</b>	53.17±1.31	67.93±1.58	85.68±6.51	76.32±1.65	89.33±0.35	87.30±1.15
GGCN	84.86±4.55	86.86±3.29	37.54±1.56	55.17±1.58	<b>71.14±1.84</b>	85.68±6.63	77.14±1.45	89.15±0.37	87.95±1.05
H2GCN	84.86±7.23	87.65±4.98	35.70±1.00	36.48±1.86	60.11±2.15	82.70±5.28	77.11±1.57	89.49±0.38	87.87±1.20
GPRGNN	78.38±4.36	82.94±4.21	34.63±1.22	31.61±1.24	46.58±1.71	80.27±8.11	77.13±1.67	87.54±0.38	87.95±1.18
FAGCN	82.43±6.89	82.94±7.95	34.87±1.25	42.59±0.79	55.22±3.19	79.19±9.79	N/A	N/A	N/A
MixHop	77.84±7.73	75.88±4.90	32.22±2.34	48.30±1.48	60.50±2.53	73.51±6.34	76.26±1.33	85.31±0.61	87.61±0.85
GCNII	77.57±3.83	80.39±3.40	37.44±1.30	38.47±1.58	63.86±3.04	77.86±3.79	77.33±1.48	<b>90.15±0.43</b>	<b>88.37±1.25</b>
Geom - GCN	66.76±2.72	64.51±3.66	31.59±1.15	38.15±0.92	60.00±2.81	60.54±3.67	<b>78.02±1.15</b>	<b>89.95±0.47</b>	85.35±1.57
PairNorm	60.27±4.34	48.43±6.14	27.40±1.24	50.44±2.04	62.74±2.82	58.92±3.15	73.59±1.47	87.53±0.44	85.79±1.01
GraphSAGE	82.43±6.14	81.18±5.56	34.23±0.99	41.61±0.74	58.73±1.68	75.95±5.01	76.04±1.30	88.45±0.50	86.90±1.04
GCN	55.14±5.16	51.76±3.06	27.32±1.10	53.43±2.01	64.82±2.24	60.54±5.30	76.50±1.36	88.42±0.50	86.98±1.27
GAT	52.16±6.63	49.41±4.09	27.44±0.89	40.72±1.55	60.26±2.50	61.89±5.05	76.55±1.23	87.30±1.10	86.33±0.48
MLP	80.81±4.75	85.29±3.31	36.53±0.70	28.77±1.56	46.21±2.99	81.89±6.40	74.02±1.90	75.69±2.00	87.16±0.37

efficiency trade-off than spatial NSD by reusing a single learned sheaf Laplacian per layer (rather than repeatedly predicting transports and re-assembling Laplacians across propagation steps).

**Datasets, Splits, Metrics and Models.** We follow the sheaf-learning literature, evaluating on the standard *real-world node-classification benchmarks* (Sen et al., 2008; Tang et al., 2009; Namata et al., 2012; Pei et al., 2020; Rozemberczki et al., 2021). We adopt the fixed per-class split protocol used in prior work (Bodnar et al., 2022): 48%/32%/20% train/validation/test, and report test accuracy (mean  $\pm$  std) over 10 fixed splits. For *synthetic experiments*, instead, we use the controlled benchmark of (Caralt et al., 2024), which decouples feature complexity from graph connectivity by tuning: feature noise, heterophily coefficient *het*, and data scale ( $N, K, n_c$ ). Further details can be found in subsection C.1 and subsection C.2. We evaluate three PolyNSD variants, *DiagPolyNSD*, *BundlePolyNSD*, and *GeneralPolyNSD*, together with *PolySpectralGNN* that serves as an additional baseline to isolate the effect of *sheaf structure* from that of *spectral polynomial filtering*. These models are compared to multiple families of baselines: *Classical GNNs* like GCN (Kipf & Welling, 2016), GAT (Velickovic et al., 2017), GraphSAGE (Hamilton et al., 2017), *Heterophily-oriented GNNs* such as GGCN (Yan et al., 2022), Geom-GCN (Pei et al., 2020), H2GCN (Zhu et al., 2020), GPRGNN (Chien et al., 2020), FAGCN (Bo et al., 2021), MixHop (Abu-El-Haija et al., 2019), *Oversmoothing remedies* including GCNII (Chien

et al., 2020), PairNorm (Chen et al., 2020), and other *Sheaf-based models* like NSD (Bodnar et al., 2022), sheaf-attention models (SAN, ANSD)(Barbero et al., 2022b), connection-based sheaves (Conn-NSD)(Barbero et al., 2022a), and joint-diffusion sheaf (RiSNN, JdSNN) (Caralt et al., 2024).

### Node Classification under Heterophily: Real World and Synthetic Benchmarks.

We first compare PolyNSD to the sheaf and non-sheaf baselines across the nine real-world benchmarks, ordered by increasing homophily, in Table 1. We provide a condensed summary here and defer the full analysis to Appendix subsection C.10, where we ablate the polynomial basis (Chebyshev Types I–IV, Chebyshev interpolation, Legendre, Gegenbauer, Jacobi) and find that performance is largely *basis-agnostic* and stable across orthogonal families. *PolyNSD* matches or improves upon state-of-the-art sheaf models, achieving top-3 performance in almost all cases, both heterophilic and homophilic. Endowing NSD with a *learnable spectral response* via a degree- $K$  polynomial filter  $p_K(\hat{L})$  yields consistent gains, confirming that explicitly controlling the frequency response is beneficial beyond first-order diffusion. Moreover, the sheaf abstraction is fundamental, as confirmed by comparing the results obtained by *PolyNSD* models with those of *PolySpectralGNN*. Interestingly, *PolyNSD often attains its best accuracy with diagonal restriction maps*: contrary to the prevailing NSD choice of dense per-edge maps (bundle/general), simple diagonal transports combined with spectral filtering suffice for state-of-the-art accuracy while substantially reducing parameters and complexity. In addition to that, *PolyNSD*

Table 2. *Spectral-response diagnostics*. Statistics aggregated per dataset over all runs in the grid (all transport classes,  $L \in \{2, 3, 4\}$ ,  $d \in \{2, 3, 4\}$ , seeds  $\{0, 1, 2\}$ , with fixed polynomial order  $K = 3$ ).

Dataset	$\alpha_{\text{hp}}$	$\Delta G$	$\Pr[G_{\text{low}} > 0]$	Non-mono.
CHAMELEON	$-0.21 \pm 0.04$	$0.41 \pm 0.08$	54.4%	2.00
SQUIRREL	$-0.29 \pm 0.09$	$0.50 \pm 0.17$	23.2%	2.00
CITSEER	$-0.67 \pm 0.20$	$0.79 \pm 0.30$	0.0%	1.79
PUBMED	$-1.29 \pm 0.30$	$1.31 \pm 0.18$	0.0%	1.58

achieves strong results at *low stalk dimensions* (see Appendix subsection C.3), showing that improvements do not rely on inflating stalk size, and directly translate into lower memory footprint and runtime. We further validate these conclusions with the controlled synthetic studies. As heterophily level, scalability, and feature noise grow, classical GNNs degrade sharply, whereas sheaf models remain more stable with PolyNSD variants consistently tracing the upper envelope of accuracy across regimes (refer to Appendix subsection C.11 for full results and plots).

**Spectral-Response Diagnostics.** To complement accuracy experiments and make PolyNSD’s *spectral* behaviour explicit, we inspect the learned frequency response of its filters. For a sheaf Laplacian eigenpair  $Lu = \lambda u$ , PolyNSD acts as  $p(L)u = p(\lambda)u$  with  $\xi(\lambda) = 2\lambda/\lambda_{\text{max}} - 1$ , and the discrete layer’s high-pass reinjection yields an interpretable combined response:

$$m(\lambda) := p(\xi(\lambda)) + \alpha_{\text{hp}} \left(1 - \frac{\lambda}{\lambda_{\text{max}}}\right) \quad (6)$$

We visualise  $m(\lambda)$  at the best checkpoint and summarise it via low/high gains  $G_{\text{low}}, G_{\text{high}}$  (means over the lowest/highest 20% of  $\lambda$ ), separation  $\Delta G := G_{\text{high}} - G_{\text{low}}$ , and a non-monotonicity score (sign changes of  $\frac{d}{d\lambda}m(\lambda)$ ). Across datasets and hyperparameter grids, the diagnostics reveal a consistent regime split (refer to Table 2 and to Appendix subsection C.8 for full details): *homophilic* graphs learn stronger low–high separation and larger-magnitude HP reinjection, while *heterophilic* graphs more often learn non-monotone (band-pass-like) responses with milder separation, aligning with the need to mix information across multiple radii rather than primarily smooth.

**Depth Robustness and Oversmoothing.** We next study depth scaling and oversmoothing by sweeping the number of layers  $L \in \{2, 4, 8, 16, 32\}$  on a subset of homophilous and heterophilous benchmarks, reporting test accuracy mean $\pm$ std. We report the full table in Appendix subsection C.4. As depth increases, *classical GNNs degrade rapidly*, often collapsing on heterophily or becoming numerically unstable at high depth. While some of the *deep baselines* remain competitive, *PolyNSD combines depth robustness with controlled propagation*: PolyNSD variants

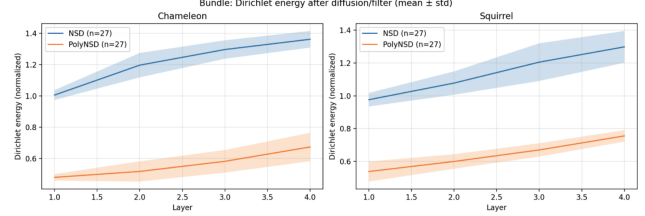


Figure 2. *Dirichlet energy trajectories diagnostics on Heterophily*.

stay stable and attain top results up to  $L = 32$ . To explain these trends beyond accuracy, we complement the sweep with a representation-level *Dirichlet-energy diagnostic*, tracking the channel-averaged normalised energy of intermediate signals  $x_\ell \in \mathbb{R}^{(Nd)} \times C$  under the learned operator  $L$ ,  $E_{\text{norm}}(x_\ell) = \frac{\langle x_\ell, Lx_\ell \rangle}{\langle x_\ell, x_\ell \rangle}$ ,  $\ell = 1, \dots, L$ , aggregated across seeds, stalk dimensions, depths, and transport classes. We observe a consistent separation: *NSD exhibits energy amplification with depth* (monotonically increasing  $E_{\text{norm}}$ ), whereas *PolyNSD yields substantially lower and more stable trajectories* across transport classes, indicating better-conditioned spectral behaviour and tighter control of depth-wise dynamics (see Figure 2). Together, these results support that PolyNSD sustains deep propagation without the instability/degeneration observed in spatial NSD and classical message passing.

**Oversquashing Probes over Long-Range Influence.** Beyond depth/energy diagnostics, we probe *oversquashing* via gradient-based *influence decay*. For a target node  $v$ , let  $s_v(x)$  be its scalar score and define  $d(u, v) := \text{dist}(u, v)$  and  $\mathcal{N}_d(v) := \{u : d(u, v) = d\}$ . The influence of a source node  $u$  on  $v$  is measured through the gradient magnitude:  $G_{uv} := \left\| \frac{\partial s_v}{\partial x_u} \right\|_2$ . We then aggregate influence by hop distance  $d$  as follows:

$$I(d) := \mathbb{E}_{v \in \mathcal{T}} \left[ \frac{1}{|\mathcal{N}_d(v)|} \sum_{u \in \mathcal{N}_d(v)} G_{uv} \right] \quad (7)$$

We compute  $\tilde{I}(d) := \frac{I(d)}{I(0)}$  up to  $D = 10$ , comparing NSD vs. PolyNSD across all transport classes across a subset of real-world datasets. As shown in Figure 3, *NSD exhibits rapid long-range influence decay* (see the entire set of examples on Appendix subsection C.5), indicating indeed vanishing sensitivity to distant nodes, a hallmark of oversquashing. In contrast, *PolyNSD consistently preserves substantially stronger long-range influence*:  $\tilde{I}(d)$  decays markedly more slowly and remains separated from NSD by multiple orders of magnitude at large  $d$  (notice the log-scale on the y-axis), indicating improved gradient flow and sensitivity to distant evidence.

**Chebyshev Order and Accuracy–Efficiency Ablations.** Beyond the main leaderboard, we probe *when* higher-order

Table 3. PolyNSD continuous-time results on node classification. Top three models are coloured by **First**, **Second** and **Third**, respectively.

	Texas	Wisconsin	Film	Squirrel	Chameleon	Cornell	Citeseer	PubMed	Cora
Homophily	<b>0.11</b>	<b>0.21</b>	<b>0.22</b>	<b>0.22</b>	<b>0.23</b>	<b>0.30</b>	<b>0.74</b>	<b>0.80</b>	<b>0.81</b>
#Nodes	183	251	7,600	5,201	2,277	183	3,327	18,717	2,708
#Edges	295	466	26,752	198,493	31,421	280	4,676	44,327	5,278
#Classes	5	5	5	5	5	5	7	3	6
Cont DiagChebySD	86.58±5.45	88.04±3.45	36.80±1.01	53.76±1.78	65.74±3.50	84.86±5.30	76.71±1.63	89.58±0.46	87.83±1.19
Cont BundleChebySD	86.84±7.16	86.47±6.17	37.42±1.12	52.34±2.43	66.49±1.55	84.59±5.27	75.66±1.60	89.70±0.31	87.73±1.26
Cont GeneralChebySD	83.42±5.53	86.86±3.40	36.76±0.96	52.87±1.89	64.10±2.35	84.86±4.22	76.01±2.03	89.32±0.38	87.79±1.34
Cont Diag-NSD	82.97±4.37	86.47±2.55	36.85±1.21	38.17±9.29	62.06±3.84	80.06±6.07	76.56±1.19	89.47±0.42	86.88±1.21
Cont O(d)-NSD	82.43±5.95	84.50±4.34	36.39±1.37	40.40±2.01	63.18±1.69	72.16±10.40	75.19±1.67	89.12±0.30	86.70±1.24
Cont Gen-NSD	83.78±6.62	85.29±3.31	37.28±0.74	52.57±2.82	66.40±2.28	84.60±4.68	77.54±1.72	89.67±0.40	87.45±0.99
BLEND	83.24±4.65	84.12±3.58	35.63±0.89	43.06±1.39	60.11±2.09	85.95±6.82	76.63±1.60	89.24±0.42	88.09±1.22
GRAND	75.68±7.25	79.41±3.64	35.62±1.01	40.05±1.50	54.67±2.54	82.16±7.09	76.46±1.77	89.02±0.52	87.36±0.96
CGNN	71.35±4.05	74.31±7.26	35.95±0.86	29.24±1.09	46.89±1.69	66.22±7.62	76.91±1.81	87.70±0.49	87.10±1.35

spectral filtering helps and *how* it trades accuracy for parameters. We first perform a controlled *Chebyshev order* sweep, fixing the best shared configuration across all datasets (stalk dimension  $d=4$ , depth  $L=2$ , hidden channels 16) and varying the polynomial order  $K \in \{1, 2, 4, 8, 12, 16\}$  together with the spectral scaling strategy (analytic vs. iterative  $\lambda_{\max}$  estimation). As shown in subsection C.6, *the best PolyNSD setting always satisfies  $K > 1$* , i.e., higher-order filters strictly improve over the NSD-equivalent  $K=1$  case at fixed depth and width. The optimal order is regime-dependent: on homophilous citation graphs, moderate orders ( $K \approx 4-8$ ) are typically sufficient, while on strongly heterophilous graphs, the optimum shifts toward larger values ( $K \approx 8-16$ ), consistent with the need for longer-range, multi-frequency mixing. We then quantify the *accuracy–efficiency frontier* against spatial NSD via two complementary sweeps: a *depth sweep* for NSD ( $L \in \{2, 4, 8, 16, 32\}$ ) compared to PolyNSD at fixed depth  $L=2$  while selecting  $K$ , and a *width sweep* for NSD (hidden  $\in \{16, 32, 64, 128, 256\}$ ) at fixed  $L=2$ . The detailed results in subsection C.7 show that *PolyNSD matches or improves NSD with substantially fewer resources*. On homophilous graphs, it is competitive at comparable or smaller parameter counts, while on heterophilous cases, it yields large gains up to  $\sim +20\%$  when comparing equal propagation power, despite using fewer layers or dramatically fewer hidden channels.

### Continuous-Time PolyNSD via Neural Sheaf ODEs.

We also extend *PolyNSD* beyond discrete layers, admitting a *continuous-depth* formulation by parameterising sheaf diffusion as a Neural Sheaf ODE. Given time-varying features  $X(t) \in \mathbb{R}^{nd \times f}$ , we predict a sheaf  $(G, \mathcal{F}(t))$  from  $X(t)$ , build its (normalised) sheaf Laplacian  $\Delta_{\mathcal{F}(t)}$ , and define the infinitesimal diffusion field by replacing the NSD affine generator with a learnable degree- $K$  polynomial  $q_\theta(\cdot)$ :

$$\dot{X}(t) = -\sigma\left(q_\theta(\Delta_{\mathcal{F}(t)})(I_n \otimes W_1) X(t) W_2\right) \quad (8)$$

where  $W_1, W_2$  are trainable weights,  $\sigma$  is a (typically 1-Lipschitz) nonlinearity, and  $q_\theta$  is implemented as a Chebyshev polynomial (e.g., a convex mixture) evaluated via a

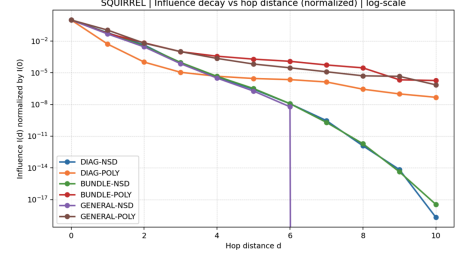


Figure 3. Oversquashing diagnostics: PolyNSD vs NSD long-range influence decay.

stable three-term recurrence on a spectrally rescaled Laplacian. For fixed sheaf structure, linear activations, and time-independent  $q_\theta$ , the dynamics  $\dot{X}(t) = -q_\theta(\Delta_{\mathcal{F}})X(t)$  has the closed-form solution  $X(T) = \exp(-T q_\theta(\Delta_{\mathcal{F}}))X(0)$ ; thus each spectral mode with eigenvalue  $\lambda$  is scaled by  $\exp(-T q_\theta(\lambda))$ , generalising continuous NSD where  $q_\theta(\lambda)$  is effectively affine in  $\lambda$ . We instantiate the same transport classes as in discrete time and integrate Equation 8 with a fixed-step solver over a horizon  $T$ , so that  $(K, T, N_{\text{steps}})$  jointly controls effective depth and spectral behaviour. Empirically, introducing polynomial spectral control in continuous time is consistently beneficial in all regimes, with PolyNSD variants frequently achieving *top-three* performance with *diagonal* variant being a strong default and suggesting a complementary interplay between *spectral shaping* (via  $q_\theta$ ) and *geometric alignment* (via transports). (See Appendix subsection C.9 for the full formulation and results).

## 5. Conclusions

We introduced *Polynomial Neural Sheaf Diffusion* (PolyNSD), a decomposition-free spectral extension of Neural Sheaf Diffusion that replaces first-order propagation with a learnable degree- $K$  orthogonal-polynomial filter  $p_K(\tilde{L})$  of a spectrally rescaled sheaf Laplacian, evaluated via stable recurrences. PolyNSD yields an explicit  $K$ -hop receptive field per layer, a learnable frequency response which reuses the learned transports without SVD-based normalisation. Across homophilic and heterophilic node-classification benchmarks, PolyNSD improves the s.o.t.a., often with *diagonal* restriction maps and moderate stalk dimensions, delivering a stronger accuracy–efficiency trade-off than spatial NSD. A non-sheaf polynomial baseline (PolySpectralGNN) isolates gains due to sheaf structure, while ablations confirm robustness across polynomial families and consistent benefits from higher-order filtering ( $K > 1$ ). Diagnostics further show controlled depth-wise energy behaviour, improved long-range influence (reduced oversquashing), and interpretable learned spectral responses, with continuous-depth variants via neural sheaf ODEs remaining competitive.

## Impact Statement

This paper presents work whose goal is to advance the field of Machine Learning. There are many potential societal consequences of our work, none which we feel must be specifically highlighted here.

## References

- Abu-El-Haija, S., Perozzi, B., Kapoor, A., Alipourfard, N., Lerman, K., Harutyunyan, H., Ver Steeg, G., and Galstyan, A. Mixhop: Higher-order graph convolutional architectures via sparsified neighborhood mixing. In *international conference on machine learning*, pp. 21–29. PMLR, 2019.
- Barbero, F., Bodnar, C., de Ocáriz Borde, H. S., Bronstein, M., Veličković, P., and Liò, P. Sheaf neural networks with connection laplacians. In *Topological, Algebraic and Geometric Learning Workshops 2022*, pp. 28–36. PMLR, 2022a.
- Barbero, F., Bodnar, C., de Ocáriz Borde, H. S., and Lio, P. Sheaf attention networks. In *NeurIPS 2022 Workshop on Symmetry and Geometry in Neural Representations*, 2022b.
- Bi, W., Du, L., Fu, Q., Wang, Y., Han, S., and Zhang, D. Make heterophilic graphs better fit gnn: A graph rewiring approach. *IEEE Transactions on Knowledge and Data Engineering*, 36(12):8744–8757, 2024. doi: 10.1109/TKDE.2024.3441766.
- Bianchi, F. M., Grattarola, D., Livi, L., and Alippi, C. Graph neural networks with convolutional arma filters. *IEEE Transactions on Pattern Analysis and Machine Intelligence*, 2021.
- Bo, D., Wang, X., Shi, C., and Shen, H. Beyond low-frequency information in graph convolutional networks. In *Proceedings of the AAAI conference on artificial intelligence*, volume 35, pp. 3950–3957, 2021.
- Bodnar, C., Di Giovanni, F., Chamberlain, B., Lio, P., and Bronstein, M. Neural sheaf diffusion: A topological perspective on heterophily and oversmoothing in gnns. *Advances in Neural Information Processing Systems*, 35: 18527–18541, 2022.
- Braithwaite, L., Duta, I., and Liò, P. Heterogeneous sheaf neural networks. *arXiv preprint arXiv:2409.08036*, 2024.
- Bruna, J., Zaremba, W., Szlam, A., and LeCun, Y. Spectral networks and locally connected networks on graphs. *arXiv preprint arXiv:1312.6203*, 2013.
- Caralt, F. H., Gil, G. B., Duta, I., Liò, P., and Cot, E. A. Joint diffusion processes as an inductive bias in sheaf neural networks. *arXiv preprint arXiv:2407.20597*, 2024.
- Chen, M., Wei, Z., Huang, Z., Ding, B., and Li, Y. Simple and deep graph convolutional networks. In *International conference on machine learning*, pp. 1725–1735. PMLR, 2020.
- Chien, E., Peng, J., Li, P., and Milenkovic, O. Adaptive universal generalized pagerank graph neural network. *arXiv preprint arXiv:2006.07988*, 2020.
- Chien, E., Pan, J., et al. Adaptive universal generalized pagerank graph neural network. In *ICLR*, 2021.
- Curry, J. M. *Sheaves, cosheaves and applications*. University of Pennsylvania, 2014.
- Defferrard, M., Bresson, X., and Vandergheynst, P. Convolutional neural networks on graphs with fast localized spectral filtering. *Advances in neural information processing systems*, 29, 2016.
- Duta, I., Cassarà, G., Silvestri, F., and Liò, P. Sheaf hypergraph networks. *Advances in Neural Information Processing Systems*, 36:12087–12099, 2023.
- Dwivedi, V. P. and Bresson, X. A generalization of transformer networks to graphs. *arXiv preprint arXiv:2012.09699*, 2020.
- Fiorini, S., Aktas, H., Duta, I., Coniglio, S., Morerio, P., Bue, A. D., and Liò, P. Sheaves reloaded: A directional awakening, 2025.
- Gilmer, J., Schoenholz, S. S., Riley, P. F., Vinyals, O., and Dahl, G. E. Neural message passing for quantum chemistry. In *International conference on machine learning*, pp. 1263–1272. Pmlr, 2017.
- Gilmer, J., Schoenholz, S. S., Riley, P. F., Vinyals, O., and Dahl, G. E. Message passing neural networks. In *Machine learning meets quantum physics*, pp. 199–214. Springer, 2020.
- Goller, C. and Kuchler, A. Learning task-dependent distributed representations by backpropagation through structure. In *Proceedings of international conference on neural networks (ICNN'96)*, volume 1, pp. 347–352. IEEE, 1996.
- Gori, M., Monfardini, G., and Scarselli, F. A new model for learning in graph domains. In *Proceedings. 2005 IEEE international joint conference on neural networks, 2005.*, volume 2, pp. 729–734. IEEE, 2005.
- Hajj, M., Bastian, L., Osentoski, S., Kabaria, H., Davenport, J. L., Dawood, S., Cherukuri, B., Kocheemoolayil, J. G., Shahmansouri, N., Lew, A., Papamarkou, T., and Birdal, T. Copresheaf topological neural networks: A generalized deep learning framework, 2025.

- Hamilton, W. L., Ying, R., and Leskovec, J. Representation learning on graphs: Methods and applications. *arXiv preprint arXiv:1709.05584*, 2017.
- Hammond, D. K., Vandergheynst, P., and Gribonval, R. Wavelets on graphs via spectral graph theory. *Applied and Computational Harmonic Analysis*, 2011.
- Hansen, J. and Gebhart, T. Sheaf neural networks. *arXiv preprint arXiv:2012.06333*, 2020.
- Hansen, J. and Ghrist, R. Toward a spectral theory of cellular sheaves. *Journal of Applied and Computational Topology*, 3(4):315–358, 2019.
- Hansen, J. and Ghrist, R. Opinion dynamics on discourse sheaves. *SIAM Journal on Applied Mathematics*, 81(5):2033–2060, 2021.
- He, Y., Bodnar, C., and Lio, P. Sheaf-based positional encodings for graph neural networks. In *NeurIPS 2023 Workshop on Symmetry and Geometry in Neural Representations*, volume 9, 2023.
- Kipf, T. N. and Welling, M. Semi-supervised classification with graph convolutional networks. *arXiv preprint arXiv:1609.02907*, 2016.
- Klicpera, J., Bojchevski, A., and Günnemann, S. Predict then propagate: Graph neural networks meet personalized pagerank. In *ICLR*, 2019.
- Levie, R., Monti, F., Bresson, X., and Bronstein, M. M. Cayleynets: Graph convolutional neural networks with complex rational spectral filters. In *ICLR*, 2018.
- Liao, R., Brockschmidt, M., et al. Lanczosnet: Multi-scale deep graph convolutional networks. In *ICLR*, 2019.
- Mule, E., Fiorini, S., Purificato, A., Siciliano, F., Coniglio, S., and Silvestri, F. Directional sheaf hypergraph networks: Unifying learning on directed and undirected hypergraphs. *arXiv preprint arXiv:2510.04727*, 2025.
- Namata, G., London, B., Getoor, L., Huang, B., and Edu, U. Query-driven active surveying for collective classification. In *10th international workshop on mining and learning with graphs*, volume 8, pp. 1, 2012.
- Nguyen, B., Sani, L., Qiu, X., Liò, P., and Lane, N. D. Sheaf hypernetworks for personalized federated learning. *arXiv preprint arXiv:2405.20882*, 2024.
- Nt, H. and Maehara, T. Revisiting graph neural networks: All we have is low-pass filters. *arXiv preprint arXiv:1905.09550*, 2019.
- Pei, H., Wei, B., Chang, K. C.-C., Lei, Y., and Yang, B. Geom-gcn: Geometric graph convolutional networks. *arXiv preprint arXiv:2002.05287*, 2020.
- Purificato, A., Cassarà, G., Siciliano, F., Liò, P., and Silvestri, F. Sheaf4rec: Sheaf neural networks for graph-based recommender systems. *ACM Transactions on Recommender Systems*, 2023.
- Rossi, E., Frasca, F., et al. Sign: Scalable inception graph neural networks. In *ICLR Workshop on Representation Learning on Graphs and Manifolds*, 2020.
- Rozemberczki, B., Allen, C., and Sarkar, R. Multi-scale attributed node embedding. *Journal of Complex Networks*, 9(2):cnab014, 2021.
- Rusch, T. K., Bronstein, M. M., and Mishra, S. A survey on oversmoothing in graph neural networks. *arXiv preprint arXiv:2303.10993*, 2023.
- Scarselli, F., Gori, M., Tsoi, A. C., Hagenbuchner, M., and Monfardini, G. The graph neural network model. *IEEE transactions on neural networks*, 20(1):61–80, 2008.
- Sen, P., Namata, G., Bilgic, M., Getoor, L., Galligher, B., and Eliassi-Rad, T. Collective classification in network data. *AI magazine*, 29(3):93–93, 2008.
- Shepard, A. D. *A cellular description of the derived category of a stratified space*. Brown University, 1985.
- Shuman, D. I., Narang, S. K., Frossard, P., Ortega, A., and Vandergheynst, P. The emerging field of signal processing on graphs: Extending high-dimensional data analysis to networks and other irregular domains. *IEEE Signal Processing Magazine*, 2013.
- Tang, J., Sun, J., Wang, C., and Yang, Z. Social influence analysis in large-scale networks. In *Proceedings of the 15th ACM SIGKDD international conference on Knowledge discovery and data mining*, pp. 807–816, 2009.
- Velickovic, P., Cucurull, G., Casanova, A., Romero, A., Lio, P., Bengio, Y., et al. Graph attention networks. *stat*, 1050(20):10–48550, 2017.
- Wu, F., Souza, A., Zhang, T., Fifty, C., et al. Simplifying graph convolutional networks. In *ICML*, 2019.
- Yan, Y., Hashemi, M., Swersky, K., Yang, Y., and Koutra, D. Two sides of the same coin: Heterophily and oversmoothing in graph convolutional neural networks. In *2022 IEEE International Conference on Data Mining (ICDM)*, pp. 1287–1292. IEEE, 2022.
- Yun, S., Jeong, M., Kim, R., Kang, J., and Kim, H. J. Graph transformer networks. *Advances in neural information processing systems*, 32, 2019.
- Zaghen, O. Nonlinear sheaf diffusion in graph neural networks. *arXiv preprint arXiv:2403.00337*, 2024.

Zhu, J., Yan, Y., Zhao, L., Heimann, M., Akoglu, L., and Koutra, D. Beyond homophily in graph neural networks: Current limitations and effective designs. *Advances in neural information processing systems*, 33:7793–7804, 2020.

## A. Spectral Theory applied to Sheaf Laplacians

This appendix is meant to better explain and justify the spectral viewpoint adopted in [section 3](#). We make explicit the role of the sheaf Laplacian as a real symmetric positive semidefinite operator on  $C^0(\mathcal{G}; \mathcal{F})$ , introduce the associated *sheaf Fourier transform*, and explain how spectral multipliers  $f(L_{\mathcal{F}})$  implement frequency-selective filters on sheaf signals. We also clarify why small eigenvalues correspond to smooth, globally aligned sheaf signals, while large eigenvalues capture oscillatory disagreement patterns, connecting to the opinion-dynamics interpretation of ([Hansen & Gebhart, 2020](#)) and the spectral theory of cellular sheaves developed in Definition ([Hansen & Ghrist, 2019](#)). Throughout,  $\mathcal{G} = (\mathcal{V}, \mathcal{E})$  is a finite undirected graph equipped with a cellular sheaf  $\mathcal{F}$ , and  $L_{\mathcal{F}}$  denotes the (vertex) sheaf Laplacian.

### A.1. Self-adjointness and Positive Semidefiniteness

We first collect the basic operator-theoretic properties of the vertex sheaf Laplacian. Throughout,  $C^0(\mathcal{G}; \mathcal{F}) \cong \mathbb{R}^{nd}$  and  $C^1(\mathcal{G}; \mathcal{F}) \cong \mathbb{R}^{|\mathcal{E}|d_e}$  are equipped with the canonical Euclidean inner product induced by the inner products on the stalks.

**Lemma 1 (Sheaf Coboundary and Laplacian).** *Let  $\delta : C^0(\mathcal{G}; \mathcal{F}) \rightarrow C^1(\mathcal{G}; \mathcal{F})$  be the sheaf coboundary associated with  $\mathcal{F}$  and the chosen orientation, and let  $L_{\mathcal{F}} := \delta^\top \delta$ . Then:*

1.  $L_{\mathcal{F}}$  is symmetric (self-adjoint) with respect to the canonical inner product on  $C^0(\mathcal{G}; \mathcal{F})$ .
2.  $L_{\mathcal{F}}$  is positive semidefinite (PSD), i.e.  $\langle x, L_{\mathcal{F}}x \rangle \geq 0$  for all  $x \in C^0(\mathcal{G}; \mathcal{F})$ .

*Proof.* For the first point, by definition,  $\delta^\top$  denotes the adjoint of  $\delta$  with respect to the inner products on  $C^0$  and  $C^1$ . Hence  $L_{\mathcal{F}} = \delta^\top \delta$  satisfies: for all  $x, y \in C^0$ :

$$\langle x, L_{\mathcal{F}}y \rangle = \langle x, \delta^\top \delta y \rangle = \langle \delta x, \delta y \rangle = \langle \delta^\top \delta x, y \rangle = \langle L_{\mathcal{F}}x, y \rangle, \quad (9)$$

which is exactly self-adjointness. For the second point, for any  $x \in C^0(\mathcal{G}; \mathcal{F})$ ,  $L_{\mathcal{F}}$  is PSD because:

$$\langle x, L_{\mathcal{F}}x \rangle = \langle x, \delta^\top \delta x \rangle = \langle \delta x, \delta x \rangle = \|\delta x\|^2 \geq 0. \quad (10)$$

□

**Lemma 1** shows that the sheaf Laplacian is the canonical “energy” operator associated with the coboundary: it is self-adjoint because it is built as an adjoint composition, and it is positive semidefinite because it always measures a squared norm of edge-wise discrepancies. Since  $C^0(\mathcal{G}; \mathcal{F})$  is finite-dimensional and  $L_{\mathcal{F}}$  is real symmetric PSD, the *Spectral Theorem* applies.

**Proposition 3 (Spectral Decomposition of  $L_{\mathcal{F}}$ ).** *There exists an orthonormal basis of  $C^0(\mathcal{G}; \mathcal{F})$  consisting of eigenvectors of  $L_{\mathcal{F}}$ . Equivalently, there is an orthogonal matrix  $U \in \mathbb{R}^{nd \times nd}$  and a diagonal matrix  $\Lambda = \text{diag}(\lambda_1, \dots, \lambda_{nd})$  with  $\lambda_i \geq 0$  s.t.  $L_{\mathcal{F}} = U\Lambda U^\top$ . We call the columns of  $U$  the sheaf Fourier modes.*

**Sheaf-Graph Laplacians Relation.** **Theorem 3** is the sheaf analogue of the usual spectral decomposition of the graph Laplacian. In the trivial-sheaf case ( $d=1$  and scalar weights on edges),  $L_{\mathcal{F}}$  reduces to the standard (combinatorial) Laplacian and  $U$  is the familiar basis of graph Fourier modes. In the general sheaf case, stalks can have dimension  $d > 1$  and edge restriction maps can perform anisotropic transports between local feature spaces, but the same spectral picture survives.

### A.2. Sheaf Fourier Transform, Plancherel Identity and Dirichlet Energy in the Spectral Domain

Once the spectral decomposition  $L_{\mathcal{F}} = U\Lambda U^\top$  is available (**Theorem 3**), it is natural to regard the columns of  $U$  as an orthonormal “frequency” basis for sheaf signals. In complete analogy with the classical graph Laplacian, any  $x \in C^0(\mathcal{G}; \mathcal{F})$  can be expanded in this eigenbasis, and the corresponding coefficients play the role of *sheaf Fourier coefficients*. The change of coordinates  $x \mapsto \hat{x} = U^\top x$  is therefore the sheaf analogue of the graph Fourier transform: it expresses  $x$  as a linear combination of sheaf Fourier modes ordered by their associated eigenvalues. This spectral viewpoint is convenient for two reasons: (i) the Euclidean norm is preserved by this change of basis (Plancherel identity), so energy computations can be carried out either in the original or in the spectral domain; and (ii) the Dirichlet energy  $\langle x, L_{\mathcal{F}}x \rangle$  becomes a simple weighted sum of squared Fourier coefficients, where the weights are precisely the eigenvalues  $\lambda_i$ . This makes explicit how each mode contributes to the total “disagreement” on the sheaf and underpins the interpretation of small eigenvalues as smooth

directions. We now formalise the *sheaf Fourier transform* and the representation of Dirichlet energy in the spectral domain.

**Definition 1 (Sheaf Fourier Transform).** Let  $L_{\mathcal{F}} = U\Lambda U^{\top}$  be as in [Theorem 3](#). For a sheaf signal  $x \in C^0(\mathcal{G}; \mathcal{F}) \cong \mathbb{R}^{nd}$  we define  $\widehat{x} := U^{\top}x \in \mathbb{R}^{nd}$  as the sheaf Fourier transform of  $x$ . The inverse transform is then defined as  $x = U\widehat{x}$ .

**Lemma 2 (Parseval/Plancherel Identity).** For all  $x, y \in C^0(\mathcal{G}; \mathcal{F})$  (with  $\|x\|_2 = \|\widehat{x}\|_2$ ), we have:  $\langle x, y \rangle = \langle \widehat{x}, \widehat{y} \rangle$ .

*Proof.* We have  $x = U\widehat{x}$ ,  $y = U\widehat{y}$ , with  $\widehat{x} = U^{\top}x$ ,  $\widehat{y} = U^{\top}y$ . Since  $U$  is orthogonal, we have:

$$\langle x, y \rangle = \langle U\widehat{x}, U\widehat{y} \rangle = \widehat{x}^{\top} U^{\top} U \widehat{y} = \widehat{x}^{\top} \widehat{y} = \langle \widehat{x}, \widehat{y} \rangle \quad (11)$$

Taking  $y = x$  gives  $\|x\|_2^2 = \|\widehat{x}\|_2^2$ . □

**Proposition 4 (Dirichlet Energy in the Spectral Domain).** Let  $x \in C^0(\mathcal{G}; \mathcal{F})$  and  $\widehat{x} = U^{\top}x$ . Then the Dirichlet Energy of  $x$  with respect to  $L_{\mathcal{F}}$  can be written as:

$$\mathcal{E}(x) := \langle x, L_{\mathcal{F}}x \rangle = \sum_{i=1}^{nd} \lambda_i \widehat{x}_i^2. \quad (12)$$

*Proof.* Using  $L_{\mathcal{F}} = U\Lambda U^{\top}$  and  $x = U\widehat{x}$ ,

$$\langle x, L_{\mathcal{F}}x \rangle = x^{\top} L_{\mathcal{F}}x = \widehat{x}^{\top} U^{\top} U \Lambda U^{\top} U \widehat{x} = \widehat{x}^{\top} \Lambda \widehat{x} = \sum_{i=1}^{nd} \lambda_i \widehat{x}_i^2.$$

□

[Equation 12](#) can now be interpreted in two complementary ways: edge-wise and spectral perspective.

**Edge-wise Viewpoint: Energy as Disagreement.** Recall that, by definition of the Sheaf Laplacian, we have:

$$\mathcal{E}(x) = \langle x, L_{\mathcal{F}}x \rangle = \|\delta x\|^2 = \sum_{e=(u,v) \in \mathcal{E}} \|\mathcal{F}_{u \triangleleft e} x_u - \mathcal{F}_{v \triangleleft e} x_v\|^2 \quad (13)$$

Thus,  $\mathcal{E}(x)$  is literally the sum of squared *disagreements* between the incident opinions transported into each edge's discourse space. If  $x$  is *perfectly consistent* with the sheaf (every incident pair agrees after transport), then  $\delta x = 0$  and  $\mathcal{E}(x) = 0$ .

**Spectral Viewpoint: Eigenvalues as Smoothness Penalties.** In the eigenbasis of  $L_{\mathcal{F}}$ , from [Theorem 4](#), we have that each sheaf Fourier mode (eigenvector) contributes to the total energy according to its eigenvalue  $\lambda_i$ . From this, depending on the value that the eigenvalue assumes, we have:

- If  $\lambda_i = 0$ , then any component along the  $i$ -th eigenvector contributes with *no* energy. These eigenvectors span  $\ker(L_{\mathcal{F}})$  and coincide with discrete *harmonic* sheaf signals (i.e., the global sections). They satisfy  $\delta x = 0$  and are perfectly aligned across edges.
- For  $\lambda_i > 0$ , the contribution of mode  $i$  is  $\lambda_i \widehat{x}_i^2$ : to achieve a large coefficient  $\widehat{x}_i$  without incurring a large energy cost, the eigenvalue  $\lambda_i$  must be small. Conversely, modes with large  $\lambda_i$  are heavily penalised and can only appear with substantial energy if they encode strong edge-wise disagreements.

This leads to the usual notion of *smoothness* on the sheaf: eigenvectors with small eigenvalues are those directions along which one can vary the signal  $x$  without creating much disagreement on edges (small  $\|\delta x\|$ ), so they represent slowly varying, globally aligned opinion profiles. Eigenvectors with large eigenvalues, instead, necessarily create large contributions to  $\|\delta x\|^2$  and thus correspond to highly *oscillatory* patterns of disagreement across incidences. In other words, the spectrum of  $L_{\mathcal{F}}$  orders sheaf Fourier modes from smooth, globally consistent patterns (low  $\lambda$ ) to rapidly varying, strongly conflicting ones (high  $\lambda$ ), exactly mirroring the role of the graph Laplacian spectrum in classical spectral graph theory but now in the richer, transport-aware sheaf setting.

### A.3. Spectral Multipliers and Functional Calculus

Once the spectral decomposition  $L_{\mathcal{F}} = U\Lambda U^{\top}$  is available, it becomes natural to ask how to apply a *function*  $f$  to the operator  $L_{\mathcal{F}}$  itself. Intuitively, since  $U$  diagonalises  $L_{\mathcal{F}}$ , we can move to the eigenbasis, modify each eigenmode by a scalar factor  $f(\lambda_i)$ , and then move back. In other words,  $f$  acts as a *frequency response* that scales each sheaf Fourier mode according to its eigenvalue, exactly as in classical spectral graph theory. For polynomials  $p$ , this idea coincides with the  $p(L_{\mathcal{F}}) = \sum_k c_k L_{\mathcal{F}}^k$  definition. The spectral theorem guarantees that this polynomial action is equivalent to applying  $p$  entrywise on the eigenvalues:  $p(L_{\mathcal{F}}) = U p(\Lambda) U^{\top}$ . More generally, by uniform approximation of continuous functions with polynomials, one can extend this construction from polynomials to arbitrary continuous  $f$  on the spectrum of  $L_{\mathcal{F}}$ , leading to the standard *continuous functional calculus*. In this framework, diffusion semigroups, heat kernels, and our polynomial sheaf filters all appear as particular choices of spectral multipliers  $f(\lambda)$ .

**Lemma 3 (Polynomial Functional Calculus).** *Let  $p(\lambda) = \sum_{k=0}^K c_k \lambda^k$  be a real polynomial and  $L_{\mathcal{F}} = U\Lambda U^{\top}$  as above. Let's define  $p(L_{\mathcal{F}}) := \sum_{k=0}^K c_k L_{\mathcal{F}}^k$ . Then:*

$$p(L_{\mathcal{F}}) = U p(\Lambda) U^{\top}, \quad p(\Lambda) = \text{diag}(p(\lambda_1), \dots, p(\lambda_{nd})). \quad (14)$$

*Proof.* From  $L_{\mathcal{F}} = U\Lambda U^{\top}$  we obtain by induction  $L_{\mathcal{F}}^k = U\Lambda^k U^{\top}$  for all  $k \geq 0$ . Indeed, for  $k = 0$  we have  $L_{\mathcal{F}}^0 = I = U I U^{\top} = U\Lambda^0 U^{\top}$ . Assume the identity now holds for some  $k \geq 0$ , then:

$$L_{\mathcal{F}}^{k+1} = L_{\mathcal{F}} L_{\mathcal{F}}^k = (U\Lambda U^{\top})(U\Lambda^k U^{\top}) = U\Lambda(U^{\top}U)\Lambda^k U^{\top} = U\Lambda^{k+1} U^{\top} \quad (15)$$

By induction the claim holds for all  $k$ . Thus:

$$p(L_{\mathcal{F}}) = \sum_{k=0}^K c_k L_{\mathcal{F}}^k = \sum_{k=0}^K c_k U\Lambda^k U^{\top} = U \left( \sum_{k=0}^K c_k \Lambda^k \right) U^{\top} \quad (16)$$

Since  $\Lambda$  is diagonal,  $\Lambda^k$  is also diagonal with entries  $\lambda_i^k$ , and therefore, we have:

$$\sum_{k=0}^K c_k \Lambda^k = \text{diag} \left( \sum_{k=0}^K c_k \lambda_1^k, \dots, \sum_{k=0}^K c_k \lambda_{nd}^k \right) = \text{diag}(p(\lambda_1), \dots, p(\lambda_{nd})) = p(\Lambda) \quad (17)$$

Substituting back yields (14).  $\square$

**Proposition 5 (Continuous functional Calculus and Operator Norm).** *Let  $f : [0, \infty) \rightarrow \mathbb{R}$  be continuous on an interval containing  $\sigma(L_{\mathcal{F}})$ . Then there exists an operator  $f(L_{\mathcal{F}})$  defined by:*

$$f(L_{\mathcal{F}}) := U f(\Lambda) U^{\top}, \quad f(\Lambda) = \text{diag}(f(\lambda_1), \dots, f(\lambda_{nd})) \quad (18)$$

*which is the uniform limit (in operator norm) of polynomial approximants  $p^{(m)}(L_{\mathcal{F}})$ . Moreover:*

$$\|f(L_{\mathcal{F}})\|_2 = \max_{\lambda \in \sigma(L_{\mathcal{F}})} |f(\lambda)|. \quad (19)$$

*Proof.* We split the proof into several steps.

*Step 1: Polynomial approximation of  $f$ .* Let  $\lambda_{\max} := \max \sigma(L_{\mathcal{F}})$ . Since  $\sigma(L_{\mathcal{F}}) \subset [0, \lambda_{\max}]$  and  $f$  is continuous on an interval containing this set, the restriction of  $f$  to  $[0, \lambda_{\max}]$  is continuous. By the Weierstrass approximation theorem, there exists a sequence of real polynomials  $(p^{(m)})_{m \in \mathbb{N}}$  such that:

$$\sup_{\lambda \in [0, \lambda_{\max}]} |p^{(m)}(\lambda) - f(\lambda)| \xrightarrow{m \rightarrow \infty} 0. \quad (20)$$

*Step 2: Induced convergence in operator norm.* For each  $m$ , define  $p^{(m)}(L_{\mathcal{F}})$  via Lemma 3:

$$p^{(m)}(L_{\mathcal{F}}) = U p^{(m)}(\Lambda) U^{\top}, \quad p^{(m)}(\Lambda) = \text{diag}(p^{(m)}(\lambda_1), \dots, p^{(m)}(\lambda_{nd})).$$

We first show that the family  $(p^{(m)}(L_{\mathcal{F}}))_m$  is Cauchy in operator norm. Let  $m, n \in \mathbb{N}$ . Then:

$$p^{(m)}(L_{\mathcal{F}}) - p^{(n)}(L_{\mathcal{F}}) = U(p^{(m)}(\Lambda) - p^{(n)}(\Lambda))U^{\top}. \quad (21)$$

Since  $U$  is orthogonal, conjugation by  $U$  preserves the spectral (operator) norm:

$$\|p^{(m)}(L_{\mathcal{F}}) - p^{(n)}(L_{\mathcal{F}})\|_2 = \|p^{(m)}(\Lambda) - p^{(n)}(\Lambda)\|_2. \quad (22)$$

Now  $p^{(m)}(\Lambda) - p^{(n)}(\Lambda)$  is diagonal, with  $i$ -th diagonal entry  $p^{(m)}(\lambda_i) - p^{(n)}(\lambda_i)$ . The operator norm of a real diagonal matrix is the maximum of the absolute values of its diagonal entries, hence:

$$\|p^{(m)}(\Lambda) - p^{(n)}(\Lambda)\|_2 = \max_{1 \leq i \leq nd} |p^{(m)}(\lambda_i) - p^{(n)}(\lambda_i)|. \quad (23)$$

Combining (22) and (23) we obtain:

$$\|p^{(m)}(L_{\mathcal{F}}) - p^{(n)}(L_{\mathcal{F}})\|_2 = \max_{\lambda \in \sigma(L_{\mathcal{F}})} |p^{(m)}(\lambda) - p^{(n)}(\lambda)|. \quad (24)$$

Since  $\sigma(L_{\mathcal{F}}) \subset [0, \lambda_{\max}]$ , the right-hand side is bounded by the uniform difference on the whole interval:

$$\max_{\lambda \in \sigma(L_{\mathcal{F}})} |p^{(m)}(\lambda) - p^{(n)}(\lambda)| \leq \sup_{\lambda \in [0, \lambda_{\max}]} |p^{(m)}(\lambda) - p^{(n)}(\lambda)|.$$

By (20),  $(p^{(m)})_m$  is Cauchy in the uniform norm on  $[0, \lambda_{\max}]$ , so the right-hand side tends to zero as  $m, n \rightarrow \infty$ . Hence  $(p^{(m)}(L_{\mathcal{F}}))_m$  is Cauchy in operator norm and therefore convergent in the finite-dimensional space of operators on  $C^0(\mathcal{G}; \mathcal{F})$ .

*Step 3: Identification of the limit with  $Uf(\Lambda)U^{\top}$ .* Let's define the diagonal matrix  $f(\Lambda) = \text{diag}(f(\lambda_1), \dots, f(\lambda_{nd}))$  and the operator  $f(L_{\mathcal{F}}) := Uf(\Lambda)U^{\top}$ . We claim that  $p^{(m)}(L_{\mathcal{F}}) \rightarrow f(L_{\mathcal{F}})$  in operator norm. Indeed, similarly to (24), we have:

$$\|p^{(m)}(L_{\mathcal{F}}) - f(L_{\mathcal{F}})\|_2 = \|U(p^{(m)}(\Lambda) - f(\Lambda))U^{\top}\|_2 = \|p^{(m)}(\Lambda) - f(\Lambda)\|_2 = \max_{1 \leq i \leq nd} |p^{(m)}(\lambda_i) - f(\lambda_i)| \quad (25)$$

Again using  $\sigma(L_{\mathcal{F}}) \subset [0, \lambda_{\max}]$  and (20), we bound  $\max_{1 \leq i \leq nd} |p^{(m)}(\lambda_i) - f(\lambda_i)| \leq \sup_{\lambda \in [0, \lambda_{\max}]} |p^{(m)}(\lambda) - f(\lambda)| \xrightarrow{m \rightarrow \infty} 0$ . Hence, we get:

$$p^{(m)}(L_{\mathcal{F}}) \xrightarrow[m \rightarrow \infty]{\|\cdot\|_2} f(L_{\mathcal{F}}) \quad (26)$$

This shows both that  $f(L_{\mathcal{F}})$  is the operator-theoretic limit of  $p^{(m)}(L_{\mathcal{F}})$  and that the operator is independent of the particular approximating sequence  $(p^{(m)})_m$ , since any two such sequences will converge to the same diagonal  $f(\Lambda)$  entrywise on the eigenvalues.

*Step 4: Operator norm identity.* We now prove that:

$$\|f(L_{\mathcal{F}})\|_2 = \max_{\lambda \in \sigma(L_{\mathcal{F}})} |f(\lambda)|. \quad (27)$$

First, using the orthogonal invariance of the spectral norm, we have:

$$\|f(L_{\mathcal{F}})\|_2 = \|Uf(\Lambda)U^{\top}\|_2 = \|f(\Lambda)\|_2. \quad (28)$$

Thus it suffices to compute the operator norm of the diagonal matrix  $f(\Lambda)$ . Let  $\mu_i := f(\lambda_i)$  denote its diagonal entries. For any vector  $y \in \mathbb{R}^{nd}$  with  $\|y\|_2 = 1$  we have:

$$\|f(\Lambda)y\|_2^2 = \sum_{i=1}^{nd} \mu_i^2 y_i^2 \leq \left( \max_i |\mu_i|^2 \right) \sum_{i=1}^{nd} y_i^2 = \left( \max_i |\mu_i| \right)^2. \quad (29)$$

Taking square roots and the supremum over all  $\|y\|_2 = 1$  yields  $\|f(\Lambda)\|_2 \leq \max_i |\mu_i| = \max_i |f(\lambda_i)|$ . To see that equality holds, pick an index  $j$  such that  $|\mu_j| = \max_i |\mu_i|$ , and let  $e_j$  be the  $j$ -th standard basis vector in  $\mathbb{R}^{nd}$  (which has norm 1). ,  $\|f(\Lambda)e_j\|_2 = |\mu_j| = \max_i |f(\lambda_i)|$ . Therefore, we have:

$$\|f(\Lambda)\|_2 = \sup_{\|y\|_2=1} \|f(\Lambda)y\|_2 \geq \|f(\Lambda)e_j\|_2 = \max_i |f(\lambda_i)|. \quad (30)$$

Combining the upper and lower bounds, we conclude that  $\|f(\Lambda)\|_2 = \max_i |f(\lambda_i)|$ . Hence, we can prove the claimed norm identity:

$$\|f(L_{\mathcal{F}})\|_2 = \|f(\Lambda)\|_2 = \max_{1 \leq i \leq nd} |f(\lambda_i)| = \max_{\lambda \in \sigma(L_{\mathcal{F}})} |f(\lambda)|. \quad (31)$$

□

In particular, taking  $f(\lambda) = p(\lambda)$  a polynomial recovers [Lemma 3](#). Taking  $f(\lambda) = e^{-t\lambda}$  gives the *sheaf heat kernel*  $e^{-tL_{\mathcal{F}}}$ , i.e. the diffusion semigroup at time  $t$ , which contracts each sheaf Fourier mode by  $e^{-t\lambda_i}$ .

#### A.4. Smoothness, Global Sections and Opinion Dynamics

The spectral decomposition of  $L_{\mathcal{F}}$ , in addition to provide a convenient basis, it organises sheaf signals according to how *globally consistent* or *disagreeing* they are with respect to the underlying transports. At one extreme, vectors in the kernel of  $L_{\mathcal{F}}$  generate perfectly aligned sheaf sections that incur no edge-wise disagreement. At the other, eigenvectors with large eigenvalues necessarily create strong local conflicts after transport. Between these two extremes lies the full spectrum of ‘‘almost harmonic’’ modes, whose small but positive eigenvalues encode smooth, slowly varying patterns of opinion. This viewpoint is made precise by the Dirichlet energy identity ([Theorem 4](#)) and matches the linear opinion-dynamics models where diffusion driven by  $L_{\mathcal{F}}$  relaxes arbitrary initial profiles toward globally consistent sections. We now connect the spectrum of  $L_{\mathcal{F}}$  with smoothness and global consistency of sheaf signals, as well as with the opinion-dynamics viewpoint.

**Zero Modes and Global Sections.** The kernel of  $L_{\mathcal{F}}$  encodes *discrete harmonic* 0-cochains for the sheaf: by [Lemma 1](#), we have  $L_{\mathcal{F}}x = 0 \iff \delta x = 0$ , i.e.,  $x$  is a 0-cocycle (i.e., a 0-cochain whose coboundary is zero). When the sheaf is suitably regular, ([Hansen & Ghrist, 2019](#)) shows that  $\ker L_{\mathcal{F}}$  is isomorphic to the space of *global sections* (or 0-th cohomology)  $H^0(\mathcal{G}; \mathcal{F})$ , meaning that  $\dim \ker L_{\mathcal{F}} = \dim H^0(\mathcal{G}; \mathcal{F})$ . Intuitively, eigenvectors with  $\lambda_i = 0$  are perfectly consistent sheaf signals that incur zero disagreement on every edge, and therefore correspond to globally aligned opinion profiles across the network.

**Opinion Dynamics and Diffusion.** In the linearised opinion-dynamics model of ([Hansen & Ghrist, 2021](#)), node opinions  $x_t \in C^0(\mathcal{G}; \mathcal{F})$  evolve according to a (discrete or continuous) diffusion equation driven by  $L_{\mathcal{F}}$ , such as  $x_{t+1} = x_t - \eta L_{\mathcal{F}}x_t$ , or  $\dot{x}(t) = -L_{\mathcal{F}}x(t)$ , for some step size  $\eta > 0$ . In the eigenbasis of  $L_{\mathcal{F}}$ , each mode evolves independently as:

$$\hat{x}_{t+1}(\lambda_i) = (1 - \eta\lambda_i)\hat{x}_t(\lambda_i) \quad \text{or} \quad \hat{x}(t, \lambda_i) = e^{-\lambda_i t}\hat{x}(0, \lambda_i) \quad (32)$$

so low-frequency modes (small  $\lambda_i$ ) decay slowly and persist, while high-frequency (large- $\lambda_i$ ) disagreement patterns decay quickly. In steady state, only the kernel modes survive, corresponding to globally consistent sections. This directly supports the interpretation used in the main text: small eigenvalues correspond to smooth, globally aligned sheaf signals, and large eigenvalues to oscillatory disagreement patterns.

**Spectral Filters as Opinion Shapers.** Given a spectral multiplier  $p(L_{\mathcal{F}})$  as in [Lemma 3](#), the response of the  $i$ -th sheaf Fourier mode is scaled by  $p(\lambda_i)$ . Choosing  $p(\lambda)$  decreasing in  $\lambda$  emphasises smooth, consensus-like profiles (low-pass); band-pass choices emphasise intermediate disagreement patterns; and choices increasing in  $\lambda$  can highlight highly localised conflicts. In this sense, the learned polynomial filters  $p(L_{\mathcal{F}})$  in PolyNSD explicitly shape how opinion profiles are smoothed, sharpened or selectively amplified across the sheaf spectrum, while remaining decomposition-free and implementable via sparse matrix–vector products.

#### A.5. Polynomial Filters: K-hop Locality and Energy Monotonicity

In this subsection we justify the structural properties of polynomial sheaf filters used in [section 3](#), namely *K-hop Locality* ([Theorem 1](#)) and a *non-increasing Dirichlet Energy* for diffusion-like multipliers ([Theorem 2](#)). Throughout,  $L$  denotes a

symmetric positive semidefinite (vertex) sheaf Laplacian on a finite graph  $G = (V, E)$ , with the usual block sparsity pattern induced by edges, and  $p, q$  denote real polynomials.

**K-hop Locality.** In order to prove K-hop locality principle, we first make precise how the sparsity pattern of  $L^k$  reflects walks in  $G$ :

**Lemma 4 (Support of Powers and Walks).** *Let  $L$  be a block matrix indexed by  $V$  such that its off-diagonal block  $(v, u)$  is nonzero only when  $(v, u) \in E$ , and diagonal blocks  $(v, v)$  are arbitrary. Then for any  $k \geq 1$  and any pair  $(v, u) \in V \times V$ :  $(L^k)_{vu} \neq 0 \Rightarrow \exists$  a walk  $v = v_0 \sim v_1 \sim \dots \sim v_\ell = u$  in  $G$  of length  $\ell \leq k$ . In particular, if  $\text{dist}_G(v, u) > k$  (no walk of length  $\leq k$ ), then  $(L^k)_{vu} = 0$ .*

*Proof.* We proceed by induction on  $k$ .

*Base case  $k = 1$ .* By assumption on  $L$ , for  $v \neq u$  we have  $L_{vu} \neq 0$  only if  $(v, u) \in E$ , which is a walk of length 1. For  $v = u$  the block  $L_{vv}$  may be nonzero, corresponding to the trivial walk of length  $0 \leq 1$ . Hence the claim holds.

*Induction step.* Assume the statement holds for some  $k \geq 1$ . Consider  $L^{k+1} = L^k L$ . Its  $(v, u)$  block satisfies:  $(L^{k+1})_{vu} = \sum_{w \in V} (L^k)_{vw} L_{wu}$ . If  $(L^{k+1})_{vu} \neq 0$ , then there exists some  $w$  such that  $(L^k)_{vw} \neq 0$  and  $L_{wu} \neq 0$ . By the induction hypothesis,  $(L^k)_{vw} \neq 0$  implies the existence of a walk  $v = v_0 \sim v_1 \sim \dots \sim v_\ell = w$  of length  $\ell \leq k$ . The condition  $L_{wu} \neq 0$  means either  $w = u$  (diagonal block) or  $(w, u) \in E$  (off-diagonal edge block). In particular:

- If  $w = u$ , we obtain a walk from  $v$  to  $u$  of length  $\ell \leq k < k + 1$  by appending a trivial step at  $u$ .
- If  $(w, u) \in E$ , we can append this edge to the walk  $v \rightsquigarrow w$  and obtain a walk  $v = v_0 \sim \dots \sim v_\ell = w \sim u$  of length  $\ell + 1 \leq k + 1$ .

In both cases, there exists a walk from  $v$  to  $u$  of length at most  $k + 1$ . This proves the implication in the lemma for  $k + 1$ , closing the induction. For the final statement, if  $\text{dist}_G(v, u) > k$  then by definition there is no walk from  $v$  to  $u$  of length  $\leq k$ , so the implication above forces  $(L^k)_{vu} = 0$ .  $\square$

We can now prove the *K-hop locality of Polynomial Filters*.

*Proof of Theorem 1.* Recall that, as defined in Equation 1, we have:  $p(L) = \sum_{k=0}^K c_k L^k$ , and more specifically, for  $v, u \in V$  we have  $(p(L))_{vu} = \sum_{k=0}^K c_k (L^k)_{vu}$ . If  $\text{dist}_G(v, u) > K$ , then  $\text{dist}_G(v, u) > k$  for all  $0 \leq k \leq K$ . For  $k = 0$  we have  $L^0 = I$ , so  $(L^0)_{vu} = 0$  whenever  $v \neq u$ . For  $k \geq 1$ , Lemma 4 implies that  $(L^k)_{vu} = 0$  whenever  $\text{dist}_G(v, u) > k$ . Therefore, each term in the sum vanishes, and we obtain  $(p(L))_{vu} = 0$  whenever  $\text{dist}_G(v, u) > K$ , as claimed.  $\square$

**Commutation and Dirichlet Energy Monotonicity.** We now justify Theorem 2.

*Proof of Theorem 2.* Let  $L$  be symmetric PSD and let  $L = U\Lambda U^\top$  be its spectral decomposition, with  $\Lambda = \text{diag}(\lambda_1, \dots, \lambda_{nd})$  and  $U$  orthogonal. For any real polynomial  $r$  we have, by Lemma 3, we have  $r(L) = U r(\Lambda) U^\top$ , where  $r(\Lambda)$  is diagonal with entries  $r(\lambda_i)$ .

*Commutation and Polynomial Composition.* Let  $p, q$  be real polynomials. Then:

$$p(L)q(L) = (Up(\Lambda)U^\top)(Uq(\Lambda)U^\top) = U p(\Lambda) (U^\top U) q(\Lambda) U^\top = U p(\Lambda)q(\Lambda) U^\top \quad (33)$$

Since  $p(\Lambda)$  and  $q(\Lambda)$  are diagonal matrices, they commute and their product is diagonal with entries  $p(\lambda_i)q(\lambda_i)$ . In other words, we have:  $p(\Lambda)q(\Lambda) = q(\Lambda)p(\Lambda) = (pq)(\Lambda)$  and therefore,  $p(L)q(L) = U (pq)(\Lambda) U^\top = (pq)(L)$ . By symmetry of the argument,  $q(L)p(L) = (pq)(L)$  as well. This proves the commutation and composition identity.

*Dirichlet Energy under a Diffusion Multiplier.* Let  $x \in C^0(\mathcal{G}; \mathcal{F})$  and write  $x = U\hat{x}$ , so that  $\hat{x} = U^\top x$  are the sheaf Fourier coefficients. Using the spectral functional calculus, we have  $p(L)x = Up(\Lambda)U^\top x = Up(\Lambda)\hat{x}$ . The Dirichlet energy of  $p(L)x$  with respect to  $L$  is:

$$\langle p(L)x, L p(L)x \rangle = \langle Up(\Lambda)\hat{x}, U\Lambda p(\Lambda)\hat{x} \rangle = \hat{x}^\top p(\Lambda)^\top \Lambda p(\Lambda) \hat{x} \quad (34)$$

where we used orthogonality of  $U$  and symmetry of  $L$ . Since  $p(\Lambda)$  and  $\Lambda$  are diagonal and real,  $p(\Lambda)^\top = p(\Lambda)$  and these matrices all commute. Writing  $\mu_i := p(\lambda_i)$ , we obtain,  $p(\Lambda)\Lambda p(\Lambda) = \text{diag}(\lambda_1 \mu_1^2, \dots, \lambda_{nd} \mu_{nd}^2)$ . We therefore have then:

$$\langle p(L)x, Lp(L)x \rangle = \sum_{i=1}^{nd} \lambda_i \mu_i^2 \hat{x}_i^2 = \sum_{i=1}^{nd} \lambda_i p(\lambda_i)^2 \hat{x}_i^2 \quad (35)$$

By contrast, the original Dirichlet energy of  $x$  is, by [Theorem 4](#), defined as:  $\langle x, Lx \rangle = \sum_{i=1}^{nd} \lambda_i \hat{x}_i^2$ . Assume now that  $0 \leq p(\lambda) \leq 1$  on  $\sigma(L)$ . Then for every eigenvalue  $\lambda_i$  we have  $0 \leq p(\lambda_i) \leq 1$  and therefore  $0 \leq p(\lambda_i)^2 \leq 1$ . Since each term in the sums is nonnegative ( $\lambda_i \geq 0$  and  $\hat{x}_i^2 \geq 0$ ), we obtain  $\lambda_i p(\lambda_i)^2 \hat{x}_i^2 \leq \lambda_i \hat{x}_i^2$  for all  $i$ . Summing over  $i$  yields:

$$\langle p(L)x, Lp(L)x \rangle = \sum_{i=1}^{nd} \lambda_i p(\lambda_i)^2 \hat{x}_i^2 \leq \sum_{i=1}^{nd} \lambda_i \hat{x}_i^2 = \langle x, Lx \rangle \quad (36)$$

which is precisely (2). This shows that any spectral multiplier with  $0 \leq p(\lambda) \leq 1$  on the spectrum acts as a diffusion-like contraction of Dirichlet energy.  $\square$

Together, [Theorem 1](#) and [Theorem 2](#) formalise the two key structural properties of PolyNSD layers: *locality* (a single layer implements exactly  $K$ -hop mixing) and *stability* (diffusion-like multipliers cannot increase disagreement energy).

### A.6. Chebyshev Filters: Spectral Rescaling, Norm Control and Energy Monotonicity

In this subsection we make precise the claims stated in [section 3](#). In particular, we justify why the affine rescaling in [Equation 3](#) is a *structural* requirement for Chebyshev parameterisations, and prove that, once the spectrum of  $L$  is mapped to  $[-1, 1]$ , convex mixtures of first-kind Chebyshev polynomials define nonexpansive spectral multipliers  $p(\tilde{L})$  with non-increasing Dirichlet energy. This provides the technical backbone for the design choices in the Chebyshev-PolyNSD layer used in the main text.

**Spectral Rescaling to  $[-1, 1]$ .** The affine rescaling that occurs inside the *Polynomial Neural Sheaf Diffusion Layer*, as described in [Equation 3](#), is what makes the PolyNSD layer both *numerically stable* and *theoretically controlled*. In particular:

1. *Extremal Property and Uniform Bound.* First-kind Chebyshev polynomials satisfy  $T_k(\xi) = \cos(k \arccos \xi)$ ,  $|\xi| \leq 1$ , and hence:

$$|T_k(\xi)| \leq 1 \quad \text{for all } \xi \in [-1, 1], k \geq 0 \quad (37)$$

This extremal/minimax property *only* holds on  $[-1, 1]$ . For  $|\xi| > 1$ , Chebyshev polynomials grow exponentially:

$$T_k(\xi) = \cosh(k \operatorname{arcosh}|\xi|), \quad |\xi| > 1 \quad (38)$$

so  $|T_k(\xi)|$  behaves like  $c(\xi) \rho(\xi)^k$  with  $\rho(\xi) > 1$ . If we were to apply  $T_k(L)$  directly to a Laplacian whose eigenvalues satisfy  $\lambda_i > 1$ , high-degree terms would produce operator norms that grow exponentially in  $k$ . In other words, the very same sequence that is beautifully bounded on  $[-1, 1]$  is catastrophically unbounded as soon as eigenvalues leave that interval. By forcing the spectrum of the *rescaled* operator  $\tilde{L}$  to lie in  $[-1, 1]$ , we ensure that every eigenvalue  $\tilde{\lambda}_i$  sits exactly in the regime where Chebyshev polynomials are uniformly bounded by 1. This is what makes convex mixtures  $\sum_k \theta_k T_k(\tilde{L})$  nonexpansive in operator norm.

2. *Stability of the Recurrence.* The matrix recurrence:

$$T_0 = x, \quad T_1 = \tilde{L}x, \quad T_{k+1} = 2\tilde{L}T_k - T_{k-1} \quad (39)$$

is a direct lifting of the scalar recurrence  $T_{k+1}(\xi) = 2\xi T_k(\xi) - T_{k-1}(\xi)$ . When  $|\xi| \leq 1$ , this recurrence is numerically stable: rounding errors do not get amplified exponentially and  $T_k(\xi)$  remains  $\mathcal{O}(1)$  in  $k$ . If instead some eigenvalues  $\lambda_i$  satisfy  $|\lambda_i| > 1$ , the same recurrence *amplifies* errors and the computed  $T_k(\lambda_i)$  will quickly diverge in magnitude, even for moderate degrees  $K$ . Rescaling to  $[-1, 1]$  by design avoids this pathological regime and allows us to evaluate  $p(\tilde{L})$  reliably with  $K$  sparse matrix–vector multiplies.

3. *Transferring Scalar Approximation Bounds to Operators.* All classical Chebyshev approximation results, are stated for functions on  $[-1, 1]$ . What we want in PolyNSD is an *operator* approximation of a spectral multiplier  $f(L)$ , with  $\sigma(L) \subset [0, \lambda_{\max}]$ . The affine map  $\xi(\lambda) = \frac{2}{\lambda_{\max}}\lambda - 1$  identifies  $[0, \lambda_{\max}]$  with  $[-1, 1]$ . We approximate  $\tilde{f}(\xi) := f(\frac{\lambda_{\max}}{2}(\xi + 1))$  by a Chebyshev polynomial  $p^{(K)}(\xi)$  on  $[-1, 1]$ , and then lift the scalar bound  $\sup_{\xi \in [-1, 1]} |\tilde{f}(\xi) - p^{(K)}(\xi)|$  to an operator bound:  $\|f(L) - p^{(K)}(\tilde{L})\|_2 = \max_{\lambda_i \in \sigma(L)} |f(\lambda_i) - p^{(K)}(\xi(\lambda_i))|$ .

We now specialise the general energy argument of [Theorem 2](#) to the Chebyshev parametrisation used in PolyNSD. This is then easily provable to be the same also for different basis parameterisations. The key point is that convex mixtures of first-kind Chebyshev polynomials on  $[-1, 1]$  are uniformly bounded by 1, which immediately implies nonexpansiveness and non-increasing Dirichlet energy after spectral rescaling.

**Proposition 6 (Boundedness and Energy Monotonicity of Convex Chebyshev Mixtures).** *If  $\sigma(\tilde{L}) \subset [-1, 1]$  and  $\theta \in \Delta^K$ , then  $\|p_\theta(\tilde{L})\|_2 \leq 1$ , and for any symmetric PSD  $L$  with  $\tilde{L}$  as above and any  $x \in C^0(\mathcal{G}; \mathcal{F})$ , we have:  $\langle p_\theta(\tilde{L})x, L p_\theta(\tilde{L})x \rangle \leq \langle x, Lx \rangle$ .*

*Proof.* By the spectral theorem, there exists an orthogonal  $U$  and diagonal  $\tilde{\Lambda} = \text{diag}(\tilde{\lambda}_i)$  with  $\tilde{\lambda}_i \in [-1, 1]$  such that  $\tilde{L} = U\tilde{\Lambda}U^\top$ . By polynomial functional calculus,  $p_\theta(\tilde{L}) = U p_\theta(\tilde{\Lambda}) U^\top$  with  $p_\theta(\tilde{\Lambda}) = \text{diag}(p_\theta(\tilde{\lambda}_i))$ . Since  $|T_k(\xi)| \leq 1$  for all  $\xi \in [-1, 1]$  and  $\theta \in \Delta^K$ , for any  $\tilde{\lambda} \in [-1, 1]$  we have:

$$|p_\theta(\tilde{\lambda})| = \left| \sum_k \theta_k T_k(\tilde{\lambda}) \right| \leq \sum_k \theta_k |T_k(\tilde{\lambda})| \leq \sum_k \theta_k = 1 \quad (40)$$

Thus  $|p_\theta(\tilde{\lambda}_i)| \leq 1$  for all  $i$ , and the spectral norm of  $p_\theta(\tilde{L})$  is  $\|p_\theta(\tilde{L})\|_2 = \|p_\theta(\tilde{\Lambda})\|_2 = \max_i |p_\theta(\tilde{\lambda}_i)| \leq 1$  which proves (6). For the energy claim, write  $L = U\Lambda U^\top$  and  $x = U\hat{x}$  as in [Theorem 4](#). Since  $\tilde{L}$  is an affine function of  $L$ , the two are simultaneously diagonalisable by  $U$ , and by [Theorem 2](#) we obtain  $\langle p_\theta(\tilde{L})x, L p_\theta(\tilde{L})x \rangle = \sum_i \lambda_i p_\theta(\tilde{\lambda}_i)^2 \hat{x}_i^2$ . We have  $0 \leq p_\theta(\tilde{\lambda}_i)^2 \leq 1$  for all  $i$  by the previous bound, so each term satisfies  $\lambda_i p_\theta(\tilde{\lambda}_i)^2 \hat{x}_i^2 \leq \lambda_i \hat{x}_i^2$ . Since all quantities are nonnegative, summing over  $i$  yields, as claimed:

$$\langle p_\theta(\tilde{L})x, L p_\theta(\tilde{L})x \rangle \leq \sum_i \lambda_i \hat{x}_i^2 = \langle x, Lx \rangle \quad (41)$$

□

So, [Proposition 6](#) shows that, once the spectrum is rescaled to  $[-1, 1]$ , the Chebyshev-PolyNSD layer inherits a *hard*  $L^2$ -stability guarantee: the linear core has operator norm at most 1 and cannot increase the sheaf Dirichlet energy. This means that PolyNSD behaves as a spectral regulariser whose frequency response is learned within a nonexpansive envelope. It is worth noting that the proof strategy is not specific to Chebyshev polynomials: any orthogonal basis  $\{B_k\}$  that is uniformly bounded on  $[-1, 1]$ , combined with a convex parametrisation of the coefficients, admits an analogous argument. Chebyshev polynomials are simply the canonical instance that simultaneously provide (i) this stability, (ii) near-minimax approximation properties, and (iii) an efficient three-term recurrence.

## B. PolyNSD Layer

This section makes precise the layer-level construction sketched in [Figure 1](#), and provides detailed operator-theoretic and approximation-theoretic guarantees. We first introduce the Chebyshev-PolyNSD block, then describe the full architecture, discuss approximation of diffusion kernels, justify our choices for estimating the spectral scale, and finally analyse the high-pass skip and residual gating.

### B.1. Chebyshev-PolyNSD Layer

Let  $L$  be either the unnormalised sheaf Laplacian  $L_{\mathcal{F}}$  or its degree-normalised variant  $\Delta_{\mathcal{F}}$ , and let  $\lambda_{\max}$  be an upper bound on  $\sigma(L)$  (equal to 2 in the normalised case, set analytically or estimated by power iteration in the unnormalised case (see [subsection B.4](#))). We first rescale to  $[-1, 1]$  as in [Equation 3](#), i.e.,  $\tilde{L} = \frac{2}{\lambda_{\max}}L - I \sigma(\tilde{L}) \subset [-1, 1]$ . *Chebyshev Polynomials* of the first kind satisfy the following:

$$T_0(\xi) = 1, \quad T_1(\xi) = \xi, \quad T_{k+1}(\xi) = 2\xi T_k(\xi) - T_{k-1}(\xi) \quad (42)$$

which we lift to operators via the three-term recurrence:

$$T_0 = x, \quad T_1 = \tilde{L}x, \quad T_{k+1} = 2\tilde{L}T_k - T_{k-1}, \quad k \geq 1 \quad (43)$$

A degree- $K$  Chebyshev-PolyNSD filter with trainable logits  $\eta \in \mathbb{R}^{K+1}$  and  $\theta = \text{softmax}(\eta) \in \Delta^K$  is then:

$$p_\theta(\tilde{L})x = \sum_{k=0}^K \theta_k T_k \quad (44)$$

By construction  $|T_k(\xi)| \leq 1$  for all  $\xi \in [-1, 1]$  and  $\theta$  is a convex combination, so  $|p_\theta(\xi)| \leq 1$  on  $[-1, 1]$ . Therefore  $\|p_\theta(\tilde{L})\|_2 \leq 1$ , and by [Theorem 2](#) and [Theorem 6](#) Chebyshev-PolyNSD layers are linear *nonexpansive* maps that cannot increase the Dirichlet energy  $\langle x, Lx \rangle$ .

## B.2. Full Polynomial Neural Sheaf Diffusion Architecture

[Figure 1](#) provides a detailed view of the full PolyNSD architecture, from raw node features to task outputs. We summarise each step, but in subsequent subsections, you can find extensive details for each of them.

(1) *Feature Lifting to Stalks.* Given a graph  $G = (V, E)$  with raw node features  $x_v^{\text{raw}} \in \mathbb{R}^{F_{\text{in}}}$ , an input MLP  $\phi : \mathbb{R}^{F_{\text{in}}} \rightarrow \mathbb{R}^d$  produces stalk features  $x_v = \phi(x_v^{\text{raw}}) \in \mathbb{R}^d$ . Stacking across nodes yields a 0-cochain  $x \in C^0(\mathcal{G}; \mathcal{F}) \cong \mathbb{R}^{N \times C}$ , where  $C$  denotes the number of feature channels.

(2) *Sheaf Learner and Restriction Maps.* A sheaf learner  $\Psi$  takes as input local edge neighbourhoods (and optionally edge attributes) and outputs per-incidence restriction maps  $\mathcal{F}_{v \sqsubseteq e} : \mathbb{R}^d \rightarrow \mathbb{R}^d$ . We support three families: *diagonal maps*  $\mathcal{F}_{v \sqsubseteq e} = \text{diag}(t_{v \sqsubseteq e})$  with  $O(|E|d)$  parameters, *bundle/orthogonal maps*  $\mathcal{F}_{v \sqsubseteq e} \in O(d)$  acting as parallel transports, and *general linear maps*  $\mathcal{F}_{v \sqsubseteq e} \in \text{GL}(d)$  with maximal expressivity. Optional scalar edge weights  $w_e$  further modulate the assembled operator.

(3) *Laplacian Assembly and Spectral Scale.* From  $\{\mathcal{F}_{v \sqsubseteq e}\}$  we assemble the vertex sheaf Laplacian  $L_{\mathcal{F}} = \delta_{\mathcal{F}}^\top \delta_{\mathcal{F}}$  (and, optionally, its degree-normalised variant  $\Delta_{\mathcal{F}}$ ). For the normalised Laplacian we use the standard spectral bound  $\lambda_{\max} = 2$ , while for the unnormalised case we either use a Gershgorin-type analytic bound or a short power iteration, as detailed in [subsection B.4](#).

(4) *PolyNSD + High-pass Skip and Residual Gate.* Given  $L$  and  $\lambda_{\max}$ , we form  $\tilde{L}$  and evaluate a degree- $K$  Chebyshev-PolyNSD filter  $p_\theta(\tilde{L})$  via the recurrence [Equation 43](#). To compensate for the intrinsic low-pass bias of diffusion we add the high-pass skip  $h_{\text{hp}} = x - \lambda_{\max}^{-1} Lx$ , scaled by a learned scalar  $\alpha_{\text{hp}}$ , and define the pre-nonlinearity  $z = p_\theta(\tilde{L})x + \alpha_{\text{hp}} h_{\text{hp}}$ . A 1-Lipschitz nonlinearity  $\phi$  and a diagonal residual gate  $\varepsilon$  then produce the update  $x^+ = (I + \tanh \varepsilon)x - \phi(z)$ . Its spectral form and global Lipschitz bound are analysed in [subsection B.5](#).

(5) *Readout and depth.* A linear readout head maps the final stalk features to logits or regression targets. Multiple PolyNSD blocks can be stacked. In practice, we recompute restriction maps at each depth, but keep the within-block recurrence cheap by reusing the same sparse Laplacian and storing only two work buffers  $(T_{k-1}, T_k)$ , so the extra memory overhead is  $O(NdC)$  and independent of  $K$ .

## B.3. Chebyshev Approximation of Diffusion Kernels

This subsection formalises the intuition that Chebyshev-PolyNSD can approximate diffusion semigroups and other smooth spectral responses with exponentially small error in the polynomial degree  $K$ , provided the target response admits an analytic extension to a neighbourhood of the spectrum. Let  $f : [0, \lambda_{\max}] \rightarrow \mathbb{R}$  be a continuous spectral response and consider its affine rescaling to  $[-1, 1]$  via  $\xi(\lambda) = \frac{2}{\lambda_{\max}}\lambda - 1$ . We recall the standard notion of a Bernstein ellipse  $E_\rho$  with foci at  $\pm 1$  and parameter  $\rho > 1$ , and use it to quantify the analyticity region of  $f$  (see [Figure 4](#)). Our first step is to control the Chebyshev coefficients of a function that is analytic and bounded on a Bernstein ellipse.

**Lemma 5 (Chebyshev Coefficients under Bernstein Analyticity).** *Let  $\tilde{f} : [-1, 1] \rightarrow \mathbb{R}$  be continuous, and assume that  $\tilde{f}$  admits an analytic continuation to the interior of  $E_\rho$  and is bounded by  $M$  there, i.e.,  $|\tilde{f}(z)| \leq M$  for all  $z \in E_\rho$ . Let  $\tilde{f}(\xi) = \sum_{k=0}^{\infty} a_k T_k(\xi)$ ,  $\xi \in [-1, 1]$  be its (pointwise convergent) Chebyshev series expansion on  $[-1, 1]$ , where  $T_k$  are*

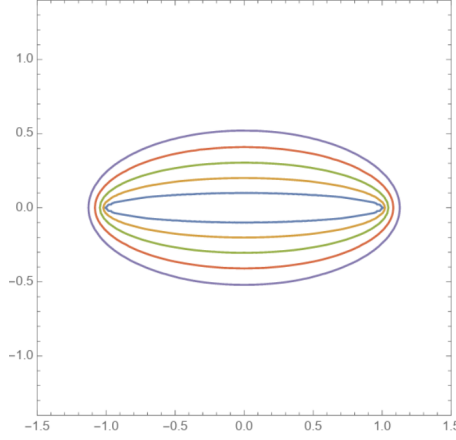


Figure 4. Bernstein ellipses  $E_\rho$  for increasing  $\rho$ . Each ellipse has foci at  $\pm 1$ . The rescaled response  $\tilde{f}$  on  $E_\rho$  implies an exponential-in- $K$  Chebyshev approximation rate with factor  $\rho^{-K}$ .

the Chebyshev polynomials of the first kind. Then, for all  $k \geq 1$ , we have:

$$|a_k| \leq \frac{2M}{\rho^k}. \quad (45)$$

*Proof.* We proceed in three steps: (i) relate  $\tilde{f}$  on  $[-1, 1]$  to a function on a circle in the complex plane, (ii) express the Chebyshev coefficients  $a_k$  as contour integrals, and (iii) bound those integrals by Cauchy's estimate.

*Step 1: Mapping the Circle to the Ellipse.* Recall that the Bernstein ellipse  $E_\rho$  is the image of the circle  $\{w \in \mathbb{C} : |w| = \rho\}$  under the Joukowski map:  $\Phi(w) := \frac{1}{2}\left(w + \frac{1}{w}\right)$ . More precisely, for  $w = \rho e^{i\theta}$  we have  $\Phi(w) \in E_\rho$ , and as  $\theta$  ranges over  $[0, 2\pi)$ ,  $\Phi(w)$  traces the ellipse  $E_\rho$  once. For  $|w| = 1$  the same map  $\Phi$  parametrises the interval  $[-1, 1]$  via  $\Phi(e^{i\theta}) = \cos \theta$ .

Define the function  $g$  on the annulus  $\{w \in \mathbb{C} : \rho^{-1} < |w| < \rho\}$  by  $g(w) := \tilde{f}(\Phi(w)) = \tilde{f}\left(\frac{1}{2}(w + w^{-1})\right)$ . By assumption,  $\tilde{f}$  is analytic on the interior of  $E_\rho$ , and the Joukowski map is analytic and maps  $\{w : |w| \leq \rho\}$  onto the closed ellipse and its interior. Hence  $g$  is analytic for  $|w| < \rho$  (away from  $w = 0$  the inverse map is well defined, and at  $w = 0$  analyticity follows by removable singularity, since  $\Phi$  is bounded near 0 and  $\tilde{f}$  is analytic in a neighbourhood of  $\Phi(0)$ ). On the circle  $|w| = \rho$  we have  $|\Phi(w)| \in E_\rho$  so  $|\tilde{f}(\Phi(w))| \leq M$ , thus:

$$|g(w)| \leq M \quad \text{for all } |w| = \rho \quad (46)$$

*Step 2: Chebyshev Expansion and Fourier Series of  $g$ .* On the unit circle  $|w| = 1$ , we can write  $w = e^{i\theta}$  and  $\Phi(w) = \cos \theta$ . The Chebyshev polynomials satisfy  $T_k(\cos \theta) = \cos(k\theta)$  for all  $k \geq 0$ , so the Chebyshev series expansion of  $\tilde{f}$  on  $[-1, 1]$  becomes a cosine series in the angular variable:

$$\tilde{f}(\cos \theta) = \sum_{k=0}^{\infty} a_k T_k(\cos \theta) = \sum_{k=0}^{\infty} a_k \cos(k\theta), \quad \theta \in \mathbb{R} \quad (47)$$

On the other hand, using  $w = e^{i\theta}$ , we have  $g(e^{i\theta}) = \tilde{f}(\Phi(e^{i\theta})) = \tilde{f}(\cos \theta)$ , so,  $g$  is restricted to the unit circle has the same real cosine expansion. We now express this cosine expansion in terms of the complex Fourier coefficients of  $g$ . Recall that  $\cos(k\theta) = \frac{1}{2}(e^{ik\theta} + e^{-ik\theta})$ , so Equation 47 becomes:

$$g(e^{i\theta}) = \tilde{f}(\cos \theta) = \sum_{k=0}^{\infty} a_k \cos(k\theta) = \frac{a_0}{2} + \sum_{k=1}^{\infty} \frac{a_k}{2} (e^{ik\theta} + e^{-ik\theta}) \quad (48)$$

Comparing with the standard Fourier series  $g(e^{i\theta}) = \sum_{m=-\infty}^{\infty} c_m e^{im\theta}$ , we identify:

$$c_0 = \frac{a_0}{2}, \quad c_k = \frac{a_k}{2}, \quad c_{-k} = \frac{a_k}{2} \quad \text{for } k \geq 1 \quad (49)$$

*Step 3: Cauchy Integral Formula and Coefficient Bounds.* By analyticity of  $g$  in  $|w| < \rho$ , each  $c_m$  can be written via Cauchy's integral formula on the circle  $|w| = \rho$ :  $c_m = \frac{1}{2\pi i} \int_{|w|=\rho} \frac{g(w)}{w^{m+1}} dw$ ,  $m \in \mathbb{Z}$ . Taking absolute values and using Equation 46 and  $|w| = \rho$ , we obtain:

$$|c_m| \leq \frac{1}{2\pi} \int_{|w|=\rho} \frac{|g(w)|}{|w|^{|m|+1}} |dw| \leq \frac{1}{2\pi} \int_{|w|=\rho} \frac{M}{\rho^{|m|+1}} |dw| = \frac{M}{2\pi\rho^{|m|+1}} \cdot 2\pi\rho = \frac{M}{\rho^{|m|}} \quad (50)$$

In particular, for  $k \geq 1$  we have  $|c_k| \leq \frac{M}{\rho^k}$  and  $|c_{-k}| \leq \frac{M}{\rho^k}$ . By Equation 49,  $a_k = 2c_k = 2c_{-k}$  for  $k \geq 1$ , we obtain exactly Equation 45 as:

$$|a_k| = 2|c_k| \leq \frac{2M}{\rho^k} \quad (51)$$

□

We now use this coefficient bound to control the truncation error of the Chebyshev series, and then lift this scalar bound to an operator bound for matrix-valued spectral filters.

**Theorem 7 (Exponential Chebyshev Convergence for Analytic Spectral Responses).** *Assume that the rescaled response  $\tilde{f}(\xi) := f\left(\frac{\lambda_{\max}}{2}(\xi + 1)\right)$  admits an analytic extension to the Bernstein ellipse  $E_\rho$  for some  $\rho > 1$ , and let  $M := \max_{z \in E_\rho} |\tilde{f}(z)|$ . Let  $p^{(K)}$  be the degree- $K$  Chebyshev truncation of  $\tilde{f}$  on  $[-1, 1]$ . Then:*

$$\sup_{\xi \in [-1, 1]} |\tilde{f}(\xi) - p^{(K)}(\xi)| \leq \frac{2M}{\rho^K(\rho - 1)} \quad (52)$$

Consequently, for any symmetric PSD  $L$  with spectrum  $\sigma(L) \subset [0, \lambda_{\max}]$  and  $\tilde{L}$  as in Equation 3:

$$\|f(L) - p^{(K)}(\tilde{L})\|_2 \leq \frac{2M}{\rho^K(\rho - 1)} \quad (53)$$

In particular, the heat kernel  $f(\lambda) = e^{-t\lambda}$  admits exponentially convergent Chebyshev approximations on  $[0, \lambda_{\max}]$  for any fixed  $t > 0$ .

*Proof.* We split the proof into two parts: first we bound the scalar approximation error of  $\tilde{f}$  by its degree- $K$  Chebyshev truncation on  $[-1, 1]$ , then we transfer the bound to the operator setting via the spectral decomposition of  $L$  and the affine rescaling  $\lambda \leftrightarrow \xi$ .

*Step 1: Scalar Chebyshev Truncation Error on  $[-1, 1]$ .* Let  $\tilde{f}(\xi) = \sum_{k=0}^{\infty} a_k T_k(\xi)$ ,  $\xi \in [-1, 1]$  be the Chebyshev series expansion of  $\tilde{f}$  on  $[-1, 1]$ , which converges uniformly on  $[-1, 1]$  under our analyticity assumption. Denote by  $p^{(K)}$  the degree- $K$  truncation  $p^{(K)}(\xi) := \sum_{k=0}^K a_k T_k(\xi)$ . The truncation error (the tail of the series) is then:

$$R_K(\xi) := \tilde{f}(\xi) - p^{(K)}(\xi) = \sum_{k=K+1}^{\infty} a_k T_k(\xi) \quad (54)$$

Using the uniform bound  $|T_k(\xi)| \leq 1$  for all  $\xi \in [-1, 1]$  and Equation 45, we obtain:

$$|R_K(\xi)| \leq \sum_{k=K+1}^{\infty} |a_k| |T_k(\xi)| \leq \sum_{k=K+1}^{\infty} |a_k| \leq \sum_{k=K+1}^{\infty} \frac{2M}{\rho^k} \quad \text{for all } \xi \in [-1, 1] \quad (55)$$

The remaining sum is geometric  $\sum_{k=K+1}^{\infty} \frac{1}{\rho^k} = \frac{\rho^{-(K+1)}}{1-\rho^{-1}} = \frac{\rho^{-K}}{\rho(1-\rho^{-1})} = \frac{\rho^{-K}}{\rho-1}$ . Plugging this into Equation 55 yields:

$$|R_K(\xi)| \leq 2M \cdot \frac{\rho^{-K}}{\rho-1} = \frac{2M}{\rho^K(\rho-1)} \quad \text{for all } \xi \in [-1, 1] \quad (56)$$

Taking the supremum over  $\xi \in [-1, 1]$  gives exactly Equation 52:

$$\sup_{\xi \in [-1, 1]} |\tilde{f}(\xi) - p^{(K)}(\xi)| = \sup_{\xi \in [-1, 1]} |R_K(\xi)| \leq \frac{2M}{\rho^K(\rho-1)} \quad (57)$$

*Step 2: Lifting the Scalar Bound to Operators.* Let  $L$  be a real symmetric PSD matrix with eigenvalues  $\lambda_1, \dots, \lambda_{nd}$  contained in  $[0, \lambda_{\max}]$ , and spectral decomposition  $L = U\Lambda U^\top$ ,  $\Lambda = \text{diag}(\lambda_1, \dots, \lambda_{nd})$  with  $U$  orthogonal. Define the affine rescaling as in Equation 3. By functional calculus, we have  $f(L) = Uf(\Lambda)U^\top$ ,  $p^{(K)}(\tilde{L}) = Up^{(K)}(\tilde{\Lambda})U^\top$  where  $f(\Lambda)$  is diagonal with entries  $f(\lambda_i)$ , and  $p^{(K)}(\tilde{\Lambda})$  is diagonal with entries  $p^{(K)}(\tilde{\lambda}_i) = p^{(K)}(\xi(\lambda_i))$ . Hence,  $f(L) - p^{(K)}(\tilde{L}) = U(f(\Lambda) - p^{(K)}(\tilde{\Lambda}))U^\top$ . The spectral (operator) norm is invariant under orthogonal conjugation, so:

$$\|f(L) - p^{(K)}(\tilde{L})\|_2 = \|f(\Lambda) - p^{(K)}(\tilde{\Lambda})\|_2 \quad (58)$$

The right-hand side is the operator norm of a diagonal matrix whose diagonal entries are  $d_i := f(\lambda_i) - p^{(K)}(\xi(\lambda_i))$ . The spectral norm of a diagonal matrix is just the maximum absolute value of its diagonal entries, thus:

$$\|f(\Lambda) - p^{(K)}(\tilde{\Lambda})\|_2 = \max_{1 \leq i \leq nd} |d_i| = \max_{\lambda_i \in \sigma(L)} |f(\lambda_i) - p^{(K)}(\xi(\lambda_i))| \quad (59)$$

By definition of  $\tilde{f}$ , we have  $\tilde{f}(\xi(\lambda)) = f\left(\frac{\lambda_{\max}}{2}(\xi(\lambda) + 1)\right) = f(\lambda)$ , so  $f(\lambda_i) = \tilde{f}(\xi(\lambda_i))$ . Therefore for each eigenvalue  $\lambda_i$  we can rewrite  $|f(\lambda_i) - p^{(K)}(\xi(\lambda_i))| = |\tilde{f}(\xi(\lambda_i)) - p^{(K)}(\xi(\lambda_i))|$ . Since  $\xi(\lambda_i) \in [-1, 1]$ , Equation 52 gives  $|\tilde{f}(\xi(\lambda_i)) - p^{(K)}(\xi(\lambda_i))| \leq \frac{2M}{\rho^K(\rho-1)}$ . Taking the maximum over all  $i$  and combining Equation 58–Equation 59 yields precisely Equation 53.

*Step 3: Application to Heat Kernels.* For the heat kernel  $f(\lambda) = e^{-t\lambda}$  with any fixed  $t > 0$ , the rescaled function:  $\tilde{f}(\xi) = f\left(\frac{\lambda_{\max}}{2}(\xi + 1)\right) = \exp\left(-t\frac{\lambda_{\max}}{2}(\xi + 1)\right)$  is an entire function of  $\xi \in \mathbb{C}$ , hence analytic on every Bernstein ellipse  $E_\rho$  and bounded by some finite  $M_\rho$ . Thus the assumptions of the theorem hold for all  $\rho > 1$ , and we conclude that the Chebyshev truncations  $p^{(K)}$  approximate  $f(L)$  with an error that decays exponentially in  $K$  as in Equation 53.  $\square$

**Theorem 7** formalises the intuition behind the Chebyshev-PolyNSD design: once the Laplacian spectrum is rescaled to  $[-1, 1]$ , the quality of the approximation  $p^{(K)}(\tilde{L}) \approx f(L)$  is controlled by *how far* the target response  $f$  extends analytically into the complex plane, as quantified by the largest Bernstein ellipse  $E_\rho$  on which  $\tilde{f}$  remains analytic and bounded. The larger this ellipse (i.e., the larger  $\rho$ ), the faster the error decreases geometrically in the degree  $K$  with factor  $\rho^{-K}$ . The theorem makes the *spectral sharpness* and *analyticity* trade-off explicit: sharper spectral filters require either a higher polynomial degree  $K$  or a relaxation of the desired uniform accuracy, whereas smoother filters (such as diffusions) can be captured extremely well with modest  $K$ .

In addition to that, the scalar bound in Equation 52 directly controls the operator approximation error in Equation 53 through the spectral calculus. Combined with the  $K$ -hop locality result for polynomial filters (see subsection A.5), this yields a clean picture: a single Chebyshev-PolyNSD layer with degree  $K$  implements a *strictly  $K$ -hop local* operator whose action approximates a global diffusion semigroup  $e^{-tL}$  (or, more generally, any analytic response  $f(L)$ ) up to an error decaying like  $\rho^{-K}$ . PolyNSD trades off the depth of the GNN with the polynomial degree  $K$ , while retaining both locality and a spectral approximation guarantee.

Finally, the argument is completely agnostic to the particular choice of  $f$ : any spectral response that is analytic on a Bernstein ellipse containing the rescaled spectrum can be uniformly approximated by Chebyshev polynomials with an explicit geometric rate. This covers not only diffusion semigroups but also families of low-pass, band-pass, and high-pass filters used in graph signal processing, provided they are regularised to admit an analytic extension on a sufficiently large  $E_\rho$ . So, **Theorem 7** gives us the approximation-theoretic backbone for Chebyshev-PolyNSD: it guarantees that PolyNSD layers can approximate a wide class of smooth spectral filters (in particular diffusion semigroups), with exponentially small error

in the polynomial degree, while retaining strict  $K$ -hop locality and the stability properties established in subsection A.6.

#### B.4. Estimating the Spectral Scale: Analytic Bound and Power Iteration

Chebyshev rescaling requires an upper spectral bound  $\lambda_{\max}$  for the chosen Laplacian  $L$ , so that the affine map in Equation 3, has spectrum in  $[-1, 1]$ . In PolyNSD we use two strategies to obtain such a bound: (i) *closed-form spectral enclosures* for normalised sheaf Laplacians and for unnormalised Laplacians via Gershgorin-type arguments, and (ii) a *short power iteration* to refine (or replace) the analytic bound on unnormalised operators. Both approaches are cheap for sparse sheaf Laplacians and provide the structural precondition needed by subsection B.3 and subsection A.6.

**Normalised Sheaf Laplacian.** For the degree-normalised sheaf Laplacian  $\Delta_{\mathcal{F}} = D^{-1/2}L_{\mathcal{F}}D^{-1/2}$ , the situation is directly analogous to the scalar graph case: all eigenvalues lie in  $[0, 2]$ .

**Proposition 8 (Spectral Enclosure for the Normalised Sheaf Laplacian).** *Let  $\Delta_{\mathcal{F}}$  be the degree-normalised (vertex) sheaf Laplacian on a finite sheaf  $\mathcal{F}$  over  $G = (V, E)$ . Then  $\Delta_{\mathcal{F}}$  is symmetric positive semidefinite and its spectrum satisfies  $\sigma(\Delta_{\mathcal{F}}) \subset [0, 2]$ .*

*Proof.* Symmetry and positive semidefiniteness follow from the usual sheaf Laplacian construction:  $L_{\mathcal{F}}$  is symmetric PSD as a discrete Hodge Laplacian and  $D^{-1/2}$  is symmetric and invertible, so  $\Delta_{\mathcal{F}} = D^{-1/2}L_{\mathcal{F}}D^{-1/2}$  is symmetric and PSD as well. For the upper bound, we use a Rayleigh quotient argument. For any nonzero  $x \in C^0(\mathcal{G}; \mathcal{F})$ , the Rayleigh quotient of  $\Delta_{\mathcal{F}}$  is:

$$R(x) := \frac{\langle x, \Delta_{\mathcal{F}}x \rangle}{\|x\|_2^2} = \frac{\langle D^{-1/2}x, L_{\mathcal{F}}D^{-1/2}x \rangle}{\|x\|_2^2} = \frac{\langle y, L_{\mathcal{F}}y \rangle}{\langle D^{1/2}y, D^{1/2}y \rangle} \quad (60)$$

where the last equality holds if we have  $y = D^{-1/2}x$ . The numerator has the usual sheaf Dirichlet form representation  $\langle y, L_{\mathcal{F}}y \rangle = \frac{1}{2} \sum_{(u,v) \in E} \|T_{vu}y_u - y_v\|_{\mathcal{F}_v}^2 \geq 0$ , while the denominator is a weighted norm  $\langle D^{1/2}y, D^{1/2}y \rangle = \sum_v \langle D_v y_v, y_v \rangle$ . The same computation as in the scalar normalised Laplacian case shows that  $0 \leq R(x) \leq 2, \forall x \neq 0$  because the local contributions at each edge are controlled by the incident degrees. Since the eigenvalues of a symmetric matrix are exactly the extremal values of its Rayleigh quotient, this implies  $\sigma(\Delta_{\mathcal{F}}) \subset [0, 2]$ .  $\square$

In practice, for normalised sheaf Laplacians we simply set  $\lambda_{\max} = 2$ , which guarantees  $\sigma(\tilde{L}) \subset [-1, 1]$  without any numerical estimation.

**Unnormalised Sheaf Laplacian: Analytic Bound via Gershgorin Discs.** When working with an unnormalised sheaf Laplacian  $L = L_{\mathcal{F}} = D - A$ , we can obtain a cheap but safe upper bound on the spectral radius by combining Gershgorin's theorem with the structural constraints on  $D$  and  $A$ .

**Proposition 9 (Gershgorin-Type Bound for Unnormalised Sheaf Laplacians).** *Let  $L_{\mathcal{F}} = D - A$  be an unnormalised sheaf Laplacian, with  $D = \text{blkdiag}(D_v) \succeq 0$  block-diagonal over vertices and  $A$  supported on off-diagonal edge blocks (so that the diagonal of  $A$  is zero). Assume that for each vertex  $v$  the diagonal block  $D_v$  dominates the outgoing sheaf couplings in the sense that:*

$$\sum_{u \neq v} \|A_{vu}\|_2 \leq \|D_v\|_2 \quad (61)$$

Then  $L_{\mathcal{F}}$  is symmetric PSD and its largest eigenvalue satisfies:

$$\lambda_{\max}(L_{\mathcal{F}}) \leq 2 \max_{v \in V} \|D_v\|_2 \quad (62)$$

In the scalar trivial-sheaf case ( $\dim \mathcal{F}_v = 1, D_v = \deg(v)$ ) this reduces to the familiar bound  $\lambda_{\max} \leq 2 \max_v \deg(v)$ .

*Proof.* Positive semidefiniteness follows from the usual sheaf Laplacian construction (as for  $L_{\mathcal{F}}$  above), so all eigenvalues are real and nonnegative. We now apply Gershgorin's disc theorem to the full matrix  $L_{\mathcal{F}}$ , viewed as an  $N \times N$  real symmetric matrix with  $N = \sum_v \dim \mathcal{F}_v$ . Let  $L_{ij}$  denote its scalar entries, and let  $\lambda$  be any eigenvalue. Gershgorin's theorem guarantees that there exists a row index  $i$  such that  $|L_{ii} - \lambda| \leq \sum_{j \neq i} |L_{ij}|$ . The row index  $i$  belongs to some vertex fibre  $\mathcal{F}_v$ , so the diagonal entry  $L_{ii}$  is one of the diagonal entries of the block  $D_v$ . Hence  $|L_{ii}| \leq \|D_v\|_2$ . On the other hand, the off-diagonal entries  $L_{ij}$  in that row come from the off-diagonal sheaf blocks  $\{-A_{vu}\}_{u \neq v}$ , so by the triangle inequality and the definition of the operator norm, we will have  $\sum_{j \neq i} |L_{ij}| \leq \sum_{u \neq v} \|A_{vu}\|_2 \leq \|D_v\|_2$  by the domination assumption Equation 61. Therefore, the corresponding Gershgorin disc for row  $i$  is contained in the real

interval:

$$[L_{ii} - R_i, L_{ii} + R_i] \subseteq [-\|D_v\|_2, 2\|D_v\|_2], \quad R_i := \sum_{j \neq i} |L_{ij}| \quad (63)$$

Since  $L_{\mathcal{F}}$  is symmetric, all its eigenvalues are real and must lie in the union of these intervals over all rows  $i$ , and hence over all vertices  $v$ . Intersecting with  $[0, \infty)$  (because  $L_{\mathcal{F}}$  is PSD), we obtain  $0 \leq \lambda \leq 2 \max_{v \in V} \|D_v\|_2$  for every eigenvalue  $\lambda$  of  $L_{\mathcal{F}}$ , which proves the claim. In the scalar case,  $D_v = \deg(v)$  and the off-diagonal entries in row  $v$  are  $-1$  along each incident edge, so  $R_i = \deg(v)$  and the usual scalar Gershgorin discs  $[0, 2 \deg(v)]$  are recovered.  $\square$

In PolyNSD, the Gershgorin-type bound of [Theorem 9](#) provides a very fast, purely local estimate of  $\lambda_{\max}$  that is guaranteed to be safe for Chebyshev rescaling, even though it can be somewhat conservative.

**Unnormalised Sheaf Laplacian: Power Iteration.** To obtain a tighter estimate of the largest eigenvalue of  $L_{\mathcal{F}}$ , we can refine (or replace) the analytic bound via a short power iteration. For a symmetric matrix  $L$  with eigenvalues  $\lambda_1 \geq \lambda_2 \geq \dots \geq 0$ , the classical power method repeatedly applies  $L$  and normalises:  $x^{(t+1)} \leftarrow \frac{Lx^{(t)}}{\|Lx^{(t)}\|_2}$ ,  $\|x^{(0)}\|_2 = 1$ , and uses the Rayleigh quotient  $\widehat{\lambda}^{(t)} := \frac{\langle x^{(t)}, Lx^{(t)} \rangle}{\|x^{(t)}\|_2^2} = \langle x^{(t)}, Lx^{(t)} \rangle$  as an approximation to  $\lambda_1$ . The next proposition states a standard error bound.

**Proposition 10 (Power-Iteration Error).** *Let  $L = U\Lambda U^T$  be real symmetric with eigenvalues  $\lambda_1 > \lambda_2 \geq \dots \geq \lambda_n \geq 0$  and orthonormal eigenvectors  $\{u_i\}_{i=1}^n$ . Let  $x^{(0)} = \sum_{i=1}^n \alpha_i u_i$  with  $\alpha_1 \neq 0$  and define  $x^{(t)}$  and  $\widehat{\lambda}^{(t)}$  as above. Set  $r := \lambda_2/\lambda_1 \in (0, 1)$ . Then for every  $t \geq 0$ :*

$$0 \leq \lambda_1 - \widehat{\lambda}^{(t)} \leq (\lambda_1 - \lambda_2) r^{2t} \frac{\|x^{(0)} - \langle x^{(0)}, u_1 \rangle u_1\|_2^2}{\langle x^{(0)}, u_1 \rangle^2} \quad (64)$$

*In particular, the Rayleigh quotient converges to  $\lambda_1$  at a geometric rate  $r^{2t}$  as  $t$  increases.*

*Proof.* We make the dependence on the spectral decomposition explicit. Since  $L = U\Lambda U^T$  and the eigenvectors form an orthonormal basis, we can write:  $x^{(0)} = \sum_{i=1}^n \alpha_i u_i$ ,  $\alpha_i = \langle x^{(0)}, u_i \rangle$ . After  $t$  steps of the (unnormalised) power method, we have  $L^t x^{(0)} = \sum_{i=1}^n \alpha_i \lambda_i^t u_i$ . Normalising, then yields:

$$x^{(t)} = \frac{L^t x^{(0)}}{\|L^t x^{(0)}\|_2} = \frac{\sum_{i=1}^n \alpha_i \lambda_i^t u_i}{\left(\sum_{i=1}^n \alpha_i^2 \lambda_i^{2t}\right)^{1/2}} \quad (65)$$

so the coordinates of  $x^{(t)}$  in the eigenbasis are:  $\beta_i^{(t)} := \langle x^{(t)}, u_i \rangle = \frac{\alpha_i \lambda_i^t}{\left(\sum_{j=1}^n \alpha_j^2 \lambda_j^{2t}\right)^{1/2}}$ . The Rayleigh quotient at step  $t$

can then be expressed as:

$$\widehat{\lambda}^{(t)} = \langle x^{(t)}, Lx^{(t)} \rangle = \sum_{i=1}^n \lambda_i (\beta_i^{(t)})^2 = \frac{\sum_{i=1}^n \alpha_i^2 \lambda_i^{2t+1}}{\sum_{i=1}^n \alpha_i^2 \lambda_i^{2t}} \quad (66)$$

*Nonnegativity of the Error.* We first show that  $\widehat{\lambda}^{(t)} \leq \lambda_1$ . Since  $\lambda_1 \geq \lambda_i$  for all  $i$ , we have  $\lambda_1 \sum_{i=1}^n \alpha_i^2 \lambda_i^{2t} \geq \sum_{i=1}^n \alpha_i^2 \lambda_i^{2t+1}$  and hence:

$$\lambda_1 - \widehat{\lambda}^{(t)} = \frac{\lambda_1 \sum_i \alpha_i^2 \lambda_i^{2t} - \sum_i \alpha_i^2 \lambda_i^{2t+1}}{\sum_i \alpha_i^2 \lambda_i^{2t}} \geq 0 \quad (67)$$

Thus  $0 \leq \widehat{\lambda}^{(t)} \leq \lambda_1$  for all  $t$ .

*Closed-Form Expression for the Error.* We can rewrite the numerator more transparently by factoring  $\lambda_1$ :

$$\lambda_1 \sum_i \alpha_i^2 \lambda_i^{2t} - \sum_i \alpha_i^2 \lambda_i^{2t+1} = \sum_{i=1}^n \alpha_i^2 (\lambda_1 - \lambda_i) \lambda_i^{2t} \quad (68)$$

The  $i = 1$  term vanishes because  $\lambda_1 - \lambda_1 = 0$ , so:  $\lambda_1 - \widehat{\lambda}^{(t)} = \frac{\sum_{i=2}^n \alpha_i^2 (\lambda_1 - \lambda_i) \lambda_i^{2t}}{\sum_{i=1}^n \alpha_i^2 \lambda_i^{2t}}$ .

*Upper Bound via the Spectral Gap.* For  $i \geq 2$  we have  $\lambda_i \leq \lambda_2$  and  $\lambda_1 - \lambda_i \leq \lambda_1 - \lambda_2$ . Therefore:

$$\sum_{i=2}^n \alpha_i^2 (\lambda_1 - \lambda_i) \lambda_i^{2t} \leq (\lambda_1 - \lambda_2) \sum_{i=2}^n \alpha_i^2 \lambda_i^{2t} \leq (\lambda_1 - \lambda_2) \lambda_2^{2t} \sum_{i=2}^n \alpha_i^2 \quad (69)$$

On the other hand, the denominator is bounded from below by the  $i = 1$  term  $\sum_{i=1}^n \alpha_i^2 \lambda_i^{2t} \geq \alpha_1^2 \lambda_1^{2t}$ . Combining these two inequalities yields:

$$\lambda_1 - \widehat{\lambda}^{(t)} \leq (\lambda_1 - \lambda_2) \frac{\lambda_2^{2t} \sum_{i=2}^n \alpha_i^2}{\alpha_1^2 \lambda_1^{2t}} = (\lambda_1 - \lambda_2) \left( \frac{\lambda_2}{\lambda_1} \right)^{2t} \frac{\sum_{i=2}^n \alpha_i^2}{\alpha_1^2} \quad (70)$$

Recalling that  $r = \lambda_2/\lambda_1 \in (0, 1)$ , we identify:

$$\sum_{i=2}^n \alpha_i^2 = \|x^{(0)} - \alpha_1 u_1\|_2^2 = \|x^{(0)} - \langle x^{(0)}, u_1 \rangle u_1\|_2^2, \quad \alpha_1 = \langle x^{(0)}, u_1 \rangle \quad (71)$$

so that we have the following equation that we can substitute in the previous inequality:

$$\frac{\sum_{i=2}^n \alpha_i^2}{\alpha_1^2} = \frac{\|x^{(0)} - \langle x^{(0)}, u_1 \rangle u_1\|_2^2}{\langle x^{(0)}, u_1 \rangle^2}, \quad (72)$$

$$\lambda_1 - \widehat{\lambda}^{(t)} \leq (\lambda_1 - \lambda_2) r^{2t} \frac{\|x^{(0)} - \langle x^{(0)}, u_1 \rangle u_1\|_2^2}{\langle x^{(0)}, u_1 \rangle^2} \quad (73)$$

Since  $0 < r < 1$ , the prefactor  $r^{2t}$  ensures geometric convergence of  $\widehat{\lambda}^{(t)}$  to  $\lambda_1$ .  $\square$

In PolyNSD we typically combine these ingredients as follows. For normalised sheaf Laplacians we fix  $\lambda_{\max} = 2$  by [Theorem 8](#). For unnormalised sheaf Laplacians we initialise  $\lambda_{\max}$  using the Gershgorin-type analytic bound of [Theorem 9](#), which requires only local degree information, and (optionally) refine it with 5–10 steps of power iteration as in [Theorem 10](#). This yields a spectrally safe rescaling  $\widetilde{L}$  for the Chebyshev-PolyNSD layer, while keeping the overhead negligible compared to the overall training cost.

### B.5. High-pass Skip and Residual Gating

We conclude the analysis of PolyNSD by formalising the spectral effect and stability properties of the *high-pass correction* and *gated residual* used in the main text, and by explaining why they are structurally useful in the design of our PolyNSD layers. A single PolyNSD layer applies, before the pointwise nonlinearity  $\phi$ , the linear transformation:

$$h_{\text{hp}} := x - \frac{1}{\lambda_{\max}} Lx \quad (74)$$

$$z := p(\widetilde{L})x + \alpha_{\text{hp}} h_{\text{hp}} \quad (75)$$

$$x^+ := (I + \tanh \varepsilon)x - \phi(z) \quad (76)$$

where  $\widetilde{L}$  is defined as [Equation 3](#) and it is the spectrally rescaled Laplacian,  $p$  is a polynomial filter (typically a convex Chebyshev mixture as in [subsection A.6](#)),  $\alpha_{\text{hp}} \in \mathbb{R}$  is a learnable scalar,  $\varepsilon$  is a learnable diagonal parameter (so  $I + \tanh \varepsilon$  is a diagonal residual gate), and  $\phi$  is a component-wise nonlinearity with Lipschitz constant  $\text{Lip}(\phi) \leq 1$ . The term  $p(\widetilde{L})x$  plays the role of a learned, spectrally controlled diffusion-like filter, whose response is bounded and well approximated as in [subsection B.3](#). The additional term  $h_{\text{hp}} = x - \frac{1}{\lambda_{\max}} Lx$  is a simple linear spectral correction: it is affine in  $L$ , cheap to compute, and has a closed-form frequency response that can be combined with  $p$  to compensate for excessive low-pass bias. The residual gate  $(I + \tanh \varepsilon)$  then allows us to tune the deviation from the identity map while keeping a global Lipschitz control.

**Proposition 11 (Spectral Shape and Global Lipschitz Bound).** *Let  $L = U\Lambda U^\top$  be symmetric positive semidefinite, with eigenvalues  $\{\lambda_i\}_{i=1}^{nd}$  and orthonormal eigenvectors  $\{u_i\}$ , and let  $\widetilde{L} = \frac{2}{\lambda_{\max}} L - I$  with  $\sigma(L) \subset [0, \lambda_{\max}]$ . Let  $p$  be any real polynomial such that  $\|p(\widetilde{L})\|_2 \leq 1$ . Then:*

1. In the eigenbasis of  $L$ , the linear operator  $x \mapsto p(\tilde{L})x + \alpha_{\text{hp}}h_{\text{hp}}$  has per-eigenvalue multiplier:

$$m(\lambda) = p\left(\frac{2\lambda}{\lambda_{\max}} - 1\right) + \alpha_{\text{hp}}\left(1 - \frac{\lambda}{\lambda_{\max}}\right), \quad \lambda \in \sigma(L) \quad (77)$$

In particular, if  $\alpha_{\text{hp}} > 0$  and  $p(\xi) \geq 0$  for all  $\xi \in [-1, 1]$ , then  $m(\lambda) > 0$  for all  $\lambda \in [0, \lambda_{\max})$ , so no non-harmonic mode ( $\lambda > 0$  with  $\lambda < \lambda_{\max}$ ) can be annihilated.

2. The full mapping  $T : x \mapsto x^+$  satisfies the global Lipschitz bound:

$$\|T(x) - T(y)\|_2 \leq \left[ (1 + \|\tanh \varepsilon\|_\infty) + \text{Lip}(\phi) (1 + 2|\alpha_{\text{hp}}|) \right] \|x - y\|_2, \quad (78)$$

i.e.  $T$  is Lipschitz with constant at most:  $L_T \leq (1 + \|\tanh \varepsilon\|_\infty) + \text{Lip}(\phi) (1 + 2|\alpha_{\text{hp}}|)$ .

*Proof.* We treat the two claims separately.

(1) *Spectral Multiplier of the High-pass Skip.*

Since  $\tilde{L}$  is an affine function of  $L$ , we have  $L\tilde{L} = \tilde{L}L$  and the two operators are simultaneously diagonalisable by the same orthogonal basis  $U$ . Writing  $L = U\Lambda U^\top$ ,  $\Lambda = \text{diag}(\lambda_1, \dots, \lambda_{nd})$ , we obtain:

$$\tilde{L} = \frac{2}{\lambda_{\max}}U\Lambda U^\top - I = U\left(\frac{2}{\lambda_{\max}}\Lambda - I\right)U^\top = U\tilde{\Lambda}U^\top \quad (79)$$

with  $\tilde{\Lambda} = \text{diag}(\tilde{\lambda}_i)$  and  $\tilde{\lambda}_i = \frac{2}{\lambda_{\max}}\lambda_i - 1 \in [-1, 1]$  for all  $i$ , by  $\sigma(L) \subset [0, \lambda_{\max}]$ . Let  $x \in C^0(\mathcal{G}; \mathcal{F})$  and write  $x = U\hat{x}$  with  $\hat{x} = (\hat{x}_i)_i$ . By polynomial functional calculus, we have:  $p(\tilde{L})x = U p(\tilde{\Lambda})\hat{x} = U(\text{diag}(p(\tilde{\lambda}_i))\hat{x})$  so the  $i$ -th Fourier coefficient of  $p(\tilde{L})x$  is:  $p(\tilde{\lambda}_i)\hat{x}_i = p\left(\frac{2\lambda_i}{\lambda_{\max}} - 1\right)\hat{x}_i$ . Similarly, for the high-pass term we have:

$$h_{\text{hp}} = \left(I - \frac{1}{\lambda_{\max}}L\right)x = U\left(I - \frac{1}{\lambda_{\max}}\Lambda\right)\hat{x} \quad (80)$$

so its  $i$ -th Fourier coefficient is then  $\left(1 - \frac{\lambda_i}{\lambda_{\max}}\right)\hat{x}_i$ . Putting these together, the pre-nonlinearity linear combination  $x \mapsto p(\tilde{L})x + \alpha_{\text{hp}}h_{\text{hp}}$  acts diagonally in the eigenbasis as:

$$\hat{x}_i \mapsto \left[ p\left(\frac{2\lambda_i}{\lambda_{\max}} - 1\right) + \alpha_{\text{hp}}\left(1 - \frac{\lambda_i}{\lambda_{\max}}\right) \right] \hat{x}_i \quad (81)$$

which is exactly the multiplier  $m(\lambda_i)$  in Equation 77. For the positivity statement, assume  $\alpha_{\text{hp}} > 0$  and  $p(\xi) \geq 0$  on  $[-1, 1]$ . For any eigenvalue  $\lambda \in [0, \lambda_{\max})$  we have  $1 - \lambda/\lambda_{\max} > 0$ , hence,  $\alpha_{\text{hp}}\left(1 - \frac{\lambda}{\lambda_{\max}}\right) > 0$  and the additional term  $p\left(\frac{2\lambda}{\lambda_{\max}} - 1\right) \geq 0$  by hypothesis. Therefore  $m(\lambda) > 0$  for all  $\lambda \in [0, \lambda_{\max})$ , so no non-harmonic eigenmode can be annihilated. The only potential zero of  $m$  on the spectrum can appear at  $\lambda = \lambda_{\max}$ , e.g. if  $p(1) = 0$  and  $\alpha_{\text{hp}} = 0$ .

(2) *Global Lipschitz Bound for the Full Update.*

Let  $x, y$  be two arbitrary inputs and set:  $\Delta x := x - y$ ,  $\Delta z := z(x) - z(y)$ . Then,  $T(x) - T(y) = (I + \tanh \varepsilon)\Delta x - (\phi(z(x)) - \phi(z(y)))$  So by the triangle inequality, we have:

$$\|T(x) - T(y)\|_2 \leq \|(I + \tanh \varepsilon)\Delta x\|_2 + \|\phi(z(x)) - \phi(z(y))\|_2 \quad (82)$$

We first bound the residual gate term. Since  $I + \tanh \varepsilon$  is diagonal, its spectral norm equals the maximum absolute value of its diagonal entries:

$$\|I + \tanh \varepsilon\|_2 = \max_j |1 + \tanh \varepsilon_j| \leq 1 + \max_j |\tanh \varepsilon_j| = 1 + \|\tanh \varepsilon\|_\infty \quad (83)$$

Hence,

$$\|(I + \tanh \varepsilon)\Delta x\|_2 \leq (1 + \|\tanh \varepsilon\|_\infty) \|\Delta x\|_2 \quad (84)$$

Next we control the nonlinear term. By Lipschitzness of  $\phi$  with constant  $\text{Lip}(\phi)$ , we have:

$$\|\phi(z(x)) - \phi(z(y))\|_2 \leq \text{Lip}(\phi) \|\Delta z\|_2 \quad (85)$$

The increment  $\Delta z$  can then be written as  $\Delta z = p(\tilde{L})\Delta x + \alpha_{\text{hp}}\left(I - \frac{1}{\lambda_{\text{max}}}\right)\Delta x$ , so by the triangle inequality and submultiplicativity of the operator norm:

$$\|\Delta z\|_2 \leq \|p(\tilde{L})\|_2 \|\Delta x\|_2 + |\alpha_{\text{hp}}| \left\| I - \frac{1}{\lambda_{\text{max}}} L \right\|_2 \|\Delta x\|_2 \quad (86)$$

By hypothesis  $\|p(\tilde{L})\|_2 \leq 1$ . Moreover, since  $L$  is symmetric PSD with eigenvalues  $\lambda_i \in [0, \lambda_{\text{max}}]$ , the eigenvalues of  $I - \frac{1}{\lambda_{\text{max}}}L$  are  $\mu_i = 1 - \lambda_i/\lambda_{\text{max}} \in [0, 1]$ , so in fact  $\left\| I - \frac{1}{\lambda_{\text{max}}}L \right\|_2 \leq 1$ . Using instead the looser bound  $\left\| I - \frac{1}{\lambda_{\text{max}}}L \right\|_2 \leq 2$  (which remains valid even if  $\lambda_{\text{max}}$  is only an upper bound on the spectrum), we obtain from Equation 86:

$$\|\Delta z\|_2 \leq (1 + 2|\alpha_{\text{hp}}|) \|\Delta x\|_2 \quad (87)$$

Combining Equation 85 and Equation 87 yields:

$$\|\phi(z(x)) - \phi(z(y))\|_2 \leq \text{Lip}(\phi) (1 + 2|\alpha_{\text{hp}}|) \|\Delta x\|_2 \quad (88)$$

Substituting together with Equation 84 into Equation 82, we obtain then:

$$\|T(x) - T(y)\|_2 \leq \left[ (1 + \|\tanh \varepsilon\|_\infty) + \text{Lip}(\phi) (1 + 2|\alpha_{\text{hp}}|) \right] \|\Delta x\|_2 \quad (89)$$

which is exactly the claimed Lipschitz bound: Equation 78.  $\square$

**High-pass Skip and Residual Gating.** Equation 77 shows that the frequency response  $m(\lambda)$  of the linear core is a *sum of two simple terms*: a learned polynomial  $p\left(\frac{2\lambda}{\lambda_{\text{max}}} - 1\right)$  and a linear profile  $\alpha_{\text{hp}}(1 - \lambda/\lambda_{\text{max}})$ . If  $p$  is chosen to approximate a diffusion semigroup  $e^{-t\lambda}$  (or any analytic low-pass filter as in subsection B.3), then  $p$  is typically strongly decreasing in  $\lambda$ , i.e.  $p(0) \approx 1$  and  $p(\lambda_{\text{max}}) \approx 0$ . In isolation, this tends to *aggressively suppress* high-frequency modes, and repeated application of such a filter can readily lead to oversmoothing. The correction  $\lambda \mapsto \alpha_{\text{hp}}\left(1 - \frac{\lambda}{\lambda_{\text{max}}}\right)$  is a simple knob that deforms this pure diffusion profile. For instance, indeed:

- If  $\alpha_{\text{hp}} < 0$  with small magnitude, then  $m(\lambda) = p(\cdot) + \alpha_{\text{hp}}(1 - \lambda/\lambda_{\text{max}})$  *subtracts more* from low frequencies (where  $1 - \lambda/\lambda_{\text{max}} \approx 1$ ) than from high ones (where  $1 - \lambda/\lambda_{\text{max}} \approx 0$ ), relatively flattening the low-pass behaviour and partially reweighting intermediate and high modes.
- Conversely, if  $\alpha_{\text{hp}} > 0$ , the same term can be used to ensure  $m(\lambda)$  remains strictly positive on  $[0, \lambda_{\text{max}}]$  when  $p \geq 0$ , as captured in item (1) of Theorem 11, so that no non-harmonic mode is accidentally annihilated by the learned polynomial.

In both cases, the effect is controlled by a *single scalar* and a linear function of the spectrum, making the impact on  $m(\lambda)$  easy to analyse and to regularise. Second, the Lipschitz estimate in Equation 78 quantifies the stability cost of inserting both the high-pass correction and the gated residual. The term  $1 + \|\tanh \varepsilon\|_\infty$  bounds how far the residual branch deviates from the identity: when  $\varepsilon$  is small, we have  $\tanh \varepsilon \approx 0$  and the residual behaves nearly isometrically. The contribution  $\text{Lip}(\phi) (1 + 2|\alpha_{\text{hp}}|)$  comes from the composition of a 1-Lipschitz nonlinearity with the pre-activation linear map  $z(x)$ : here 1 corresponds to the nonexpansive polynomial  $p(\tilde{L})$  (by design of the Chebyshev-PolyNSD core), while  $2|\alpha_{\text{hp}}|$  bounds the additional amplification introduced by the high-pass term  $I - \frac{1}{\lambda_{\text{max}}}L$ . This makes transparent the trade-off: larger  $|\alpha_{\text{hp}}|$  allows more aggressive reshaping of the spectrum but increases the worst-case Lipschitz constant linearly and explicitly, which can be controlled during optimisation (e.g. via weight regularisation or explicit constraints on  $\alpha_{\text{hp}}$  and  $\varepsilon$ ). Together with the approximation results of subsection B.3 and the nonexpansive properties of Chebyshev mixtures in subsection A.6, Theorem 11 therefore explains why PolyNSD augments its diffusion-like polynomial core with exactly (i) a linear spectral correction of the form  $I - \frac{1}{\lambda_{\text{max}}}L$  and (ii) a diagonal residual gate: they provide a low-complexity, analytically tractable

way to combat oversmoothing and to preserve informative high-frequency content, while keeping the overall layer within a globally controlled Lipschitz envelope.

### B.6. PolyNSD vs Neural Sheaf Diffusion: Operator Class

In this subsection we make precise the claim that Chebyshev-PolyNSD with degree  $K=1$  recovers the same diffusion operator class as Neural Sheaf Diffusion (NSD) (Bodnar et al., 2022), while for  $K>1$  it strictly generalises it to higher-order polynomials in the sheaf Laplacian. In order to do that, we focus on the *diffusion core*, i.e. the linear operator that acts on sheaf 0-cochains between pointwise nonlinearities and feature-mixing MLPs.

**Canonical NSD Diffusion Core.** In Neural Sheaf Diffusion, once a sheaf Laplacian  $L$  has been assembled from learned restriction maps, the diffusion step acting on a 0-cochain  $x \in C^0(\mathcal{G}; \mathcal{F})$  can be written abstractly as:

$$x^+ = Ax - BLx, \quad (90)$$

where  $A$  and  $B$  are feature-wise scaling operators, encoding the step size and residual weighting. For the purposes of spectral analysis, the key point is that, for fixed  $L$ , NSD’s diffusion core always lies in the two-dimensional linear span  $\{I, L\}$ : it is a first-order polynomial  $aI + bL$ , with  $a, b$  determined by the learnable scalings in Equation 90 (possibly different per feature channel). We now show that Chebyshev-PolyNSD with  $K=1$  recovers exactly this operator class, and that allowing  $K>1$  extends it to higher-order polynomials in  $L$  with explicit  $K$ -hop locality.

#### B.6.1. CHEBYSHEV POLYNSD WITH $K=1$ RECOVERS NSD

Let’s start from the layer update used in PolyNSD (Equation 5, where  $p_\theta(\tilde{L})$  is a degree- $K$  polynomial in  $\tilde{L}$  (e.g. a convex Chebyshev mixture),  $\alpha_{\text{hp}} \in \mathbb{R}$  is a scalar high-pass weight,  $\varepsilon$  is a diagonal residual gate, and  $\phi$  is a 1-Lipschitz nonlinearity. For the operator-class comparison we temporarily set  $\phi$  to the identity and focus on the linear map  $x \mapsto x^+$ .

**Degree-1 Chebyshev Parameterisation.** For  $K=1$ , the Chebyshev recurrence yields:

$$T_0(\tilde{L}) = I, \quad T_1(\tilde{L}) = \tilde{L} = \frac{2}{\lambda_{\max}}L - I \quad (91)$$

Let  $\theta = (\theta_0, \theta_1) \in \Delta^1$  be the (convex) coefficients of the Chebyshev mixture, e.g.  $\theta = \text{softmax}(\eta)$  for some logits  $\eta \in \mathbb{R}^2$ . The degree-1 filter is then  $p_\theta(\tilde{L}) = \theta_0 T_0(\tilde{L}) + \theta_1 T_1(\tilde{L}) = \theta_0 I + \theta_1 \left( \frac{2}{\lambda_{\max}}L - I \right)$ . Acting on an input  $x$ , this gives  $x_{\text{cheb}} := p_\theta(\tilde{L})x = (\theta_0 - \theta_1)x + \theta_1 \frac{2}{\lambda_{\max}}Lx$ . The high-pass correction is  $h_{\text{hp}} = x - \frac{1}{\lambda_{\max}}Lx$  and the pre-nonlinearity activation becomes:

$$z = x_{\text{cheb}} + \alpha_{\text{hp}} h_{\text{hp}} = (\theta_0 - \theta_1 + \alpha_{\text{hp}})x + \left( \theta_1 \frac{2}{\lambda_{\max}} - \alpha_{\text{hp}} \frac{1}{\lambda_{\max}} \right) Lx \quad (92)$$

Finally, setting  $\phi$  to the identity<sup>1</sup>, we obtain:

$$x^+ = (I + \tanh \varepsilon)x - z \quad (93)$$

**Proposition 12 (Chebyshev-PolyNSD with  $K=1$  Induces a First-Order Polynomial in  $L$ ).** Under the setup above with  $K=1$  and  $\phi = \text{id}$ , the PolyNSD update in Equation 93 can be written as:

$$x^+ = ax + bLx \quad (94)$$

where the coefficients  $a, b$  (per feature channel) are given by:

$$a = (1 + \tanh \varepsilon) - (\theta_0 - \theta_1 + \alpha_{\text{hp}}), \quad b = -\left( \theta_1 \frac{2}{\lambda_{\max}} - \alpha_{\text{hp}} \frac{1}{\lambda_{\max}} \right) \quad (95)$$

In particular, for any fixed  $L$  and  $\lambda_{\max}$ , the degree-1 Chebyshev-PolyNSD core spans the same operator class  $\{aI + bL\}$  as NSD’s diffusion core in Equation 90.

<sup>1</sup>In practice  $\phi$  is a 1-Lipschitz nonlinearity; here we isolate the linear diffusion core. The nonlinearity can be placed before or after this core in both NSD and PolyNSD, and does not change the operator class of the linear part.

*Proof.* Substituting the expression for  $z$  in Equation 92 into Equation 93 yields:

$$x^+ = (I + \tanh \varepsilon)x - \left[ (\theta_0 - \theta_1 + \alpha_{\text{hp}})x + \left( \theta_1 \frac{2}{\lambda_{\text{max}}} - \alpha_{\text{hp}} \frac{1}{\lambda_{\text{max}}} \right) Lx \right] \quad (96)$$

$$= \left[ (1 + \tanh \varepsilon) - (\theta_0 - \theta_1 + \alpha_{\text{hp}}) \right] x - \left[ \theta_1 \frac{2}{\lambda_{\text{max}}} - \alpha_{\text{hp}} \frac{1}{\lambda_{\text{max}}} \right] Lx \quad (97)$$

Defining  $a, b$  as in Equation 95 gives the claimed form in Equation 94. Since  $a, b \in \mathbb{R}$  (or feature-wise scalars when  $\varepsilon$  is diagonal), this coincides with the NSD form Equation 90, i.e. a first-order polynomial  $aI + bL$ .  $\square$

**Finding PolyNSD Parameters from NSD Diffusion Step.** Given a target NSD diffusion step:  $x_{\text{NSD}}^+ = Ax - BLx$ , we can always find PolyNSD parameters  $(\theta_0, \theta_1, \alpha_{\text{hp}}, \varepsilon)$  realising the same operator, up to per-channel scaling, provided  $\lambda_{\text{max}} > 0$ . For example, in the degree-normalised setting where  $\lambda_{\text{max}} = 2$  and we ignore the high-pass term ( $\alpha_{\text{hp}} = 0$ ), choosing  $\theta_1 = \frac{B}{2}, \theta_0 = 1 - \theta_1$  gives  $b = -B$  in Equation 95, and then we can enforce  $a = A$  by tuning  $\varepsilon$ , i.e. setting the residual gate so that  $1 + \tanh \varepsilon = A + (\theta_0 - \theta_1)$ . Thus, after fixing  $\lambda_{\text{max}}$ , the map from PolyNSD parameters to the pair  $(a, b)$  is surjective onto the NSD operator class  $\{aI + bL\}$ .

### B.6.2. STRICT GENERALISATION FOR $K > 1$

We now show that allowing higher polynomial degrees  $K > 1$  extends the diffusion operator class from  $\{aI + bL\}$  to all polynomials in  $L$  of degree at most  $K$ . Under mild spectral assumptions on  $L$ , this generalises NSD strictly, meaning that there exist PolyNSD operators that cannot be represented by any single NSD diffusion step.

**PolyNSD Operator Class for General  $K$ .** For a degree- $K$  Chebyshev-PolyNSD core, the filter  $p_\theta$  can be written as  $p_\theta(\tilde{L}) = \sum_{k=0}^K \theta_k T_k(\tilde{L}), \theta \in \Delta^K$ . Each  $T_k(\tilde{L})$  is itself a degree- $k$  polynomial in  $L$  (since  $\tilde{L}$  is affine in  $L$ ), so  $p_\theta(\tilde{L})$  is a polynomial in  $L$  of degree at most  $K$ . The same calculation as in the  $K=1$  case shows that the full linear core:  $x \mapsto (I + \tanh \varepsilon)x - (p_\theta(\tilde{L})x + \alpha_{\text{hp}} h_{\text{hp}})$  remains a polynomial in  $L$  of degree at most  $K$ .

**Proposition 13 (PolyNSD Core as a Polynomial in  $L$ ).** *For fixed  $L$  and  $\lambda_{\text{max}} > 0$ , any Chebyshev-PolyNSD diffusion core with degree  $K$  (and  $\phi = \text{id}$ ) can be written as  $x^+ = q(L)x$ , where  $q$  is a polynomial in one variable of degree at most  $K$ , whose coefficients depend linearly on  $\theta, \alpha_{\text{hp}}$  and  $I + \tanh \varepsilon$ . In particular, taking  $K=1$  recovers the class  $\{aI + bL\}$  of NSD, while  $K > 1$  yields higher-order polynomials.*

*Proof.* By definition,  $T_k(\tilde{L})$  is a degree- $k$  polynomial in  $\tilde{L}$ . Since  $\tilde{L}$  is an affine function of  $L$ , each  $T_k(\tilde{L})$  is a degree- $k$  polynomial in  $L$ . Therefore,  $p_\theta(\tilde{L}) = \sum_{k=0}^K \theta_k T_k(\tilde{L})$  is a polynomial in  $L$  of degree at most  $K$ . The high-pass term  $h_{\text{hp}} = x - \lambda_{\text{max}}^{-1} Lx$  is a first-order polynomial in  $L$ , and the residual term  $(I + \tanh \varepsilon)x$  is a degree-0 polynomial (the identity scaled). Subtracting a linear combination of these three contributions preserves polynomial structure and does not increase the degree. Hence the overall linear map  $x \mapsto x^+$  is of the form  $x^+ = q(L)x$  with  $\deg q \leq K$ .  $\square$

**Strictness Under Mild Spectral Assumptions.** To argue that PolyNSD with  $K > 1$  is not merely a reparameterisation of NSD, we show that, under mild conditions on the spectrum of  $L$ , there exist polynomials  $q$  of degree at least 2 that cannot be represented as  $aI + bL$ .

**Proposition 14 (Strict Generalisation for  $K > 1$ ).** *Assume  $L$  has at least three distinct eigenvalues  $\lambda_{i_1}, \lambda_{i_2}, \lambda_{i_3} \in \sigma(L)$ . Let  $q$  be a real polynomial of degree  $d \geq 2$ , and consider the operator  $q(L)$ . Then, there is no pair  $a, b \in \mathbb{R}$  such that  $q(L) = aI + bL$ , unless  $q$  coincides with an affine polynomial on the set  $\{\lambda_{i_1}, \lambda_{i_2}, \lambda_{i_3}\}$ . In particular, for generic choices of  $\theta$  that induce a polynomial of degree at least 2, the resulting PolyNSD operator cannot be realised by any NSD core of the form Equation 90.*

*Proof.* Write the spectral decomposition  $L = U\Lambda U^\top$  with  $\Lambda = \text{diag}(\lambda_1, \dots, \lambda_{nd})$ . Then,  $q(L) = Uq(\Lambda)U^\top, aI + bL = U(aI + b\Lambda)U^\top$ . If  $q(L) = aI + bL$ , then conjugating by  $U^\top$  gives  $q(\Lambda) = aI + b\Lambda$ , i.e.,  $q(\lambda_i) = a + b\lambda_i$ , for all  $i$ . In particular, for the three distinct eigenvalues  $\lambda_{i_1}, \lambda_{i_2}, \lambda_{i_3}$ , we must have  $q(\lambda_{i_j}) = a + b\lambda_{i_j}, j = 1, 2, 3$ . But an affine function  $\lambda \mapsto a + b\lambda$  is determined uniquely by its values on any two distinct points. If a degree- $d$  polynomial  $q$  with  $d \geq 2$  coincides with an affine function on three distinct points, then its second finite difference on these points must vanish, forcing the quadratic and higher-order terms of  $q$  to cancel there. For a generic choice of  $q$  and eigenvalues, this does not occur. Concretely, if we choose coefficients so that the highest-degree coefficient is nonzero and the polynomial is not exactly affine on the three eigenvalues, then no such  $a, b$  can exist. This shows that, whenever  $q$  is genuinely of

degree at least 2 on three distinct eigenvalues, the operator  $q(L)$  cannot be compressed into the NSD form  $aI + bL$ .  $\square$

Thus, as soon as  $L$  exhibits a reasonably rich spectrum (three or more distinct eigenvalues) and the learned Chebyshev coefficients  $\theta \in \Delta^K$  activate higher-order terms ( $\deg q \geq 2$ ), PolyNSD realises operators outside the NSD class.

**Depth vs Polynomial Degree and Computational Cost.** Let’s now also compare PolyNSD and NSD from a *depth* and *complexity* perspective. For fixed  $L$  and linear activations, stacking  $T$  NSD diffusion cores of the form  $a_t I + b_t L$  yields  $x^{(T)} = \left( \prod_{t=1}^T (a_t I + b_t L) \right) x^{(0)}$ , which is a polynomial in  $L$  of degree at most  $T$ . Conversely, any polynomial in  $L$  with real roots can be factorised (over  $\mathbb{C}$ ) as a product of linear factors, which can in principle be mapped to NSD-style layers. In practice, however, this requires  $T$  layers, each with its own sheaf prediction and Laplacian assembly. By contrast, a single degree- $K$  PolyNSD layer computes  $p_\theta(\tilde{L})x$  via a three-term recurrence using  $K$  sparse matrix–vector products with  $\tilde{L}$ , reusing the same sheaf Laplacian within the block. The resulting complexity is  $\mathcal{O}(K \text{nnz}(L) C)$ , for feature dimension  $C$ , which matches the asymptotic cost of stacking  $K$  NSD layers with *fixed* sheaf structure, *but avoids repeated edge-wise sheaf prediction and Laplacian construction*. Combined with the approximation guarantees in [subsection B.3](#) and the stability results in [subsection A.6](#) and [subsection B.5](#), this shows that PolyNSD provides a spectrally controlled, computationally efficient generalisation of NSD: degree  $K=1$  recovers NSD’s diffusion core, while  $K>1$  trades depth for polynomial degree, enlarging the operator class from first-order to higher-order polynomials in the sheaf Laplacian with explicit  $K$ -hop locality.

## C. Extensive and Additional Experiments

This appendix collects the full experimental details for the results reported in [section 4](#). We first describe the datasets used in our evaluation, then provide a consolidated view of model variants, hyperparameters, ablations, interpretability diagnostics, and training protocols for PolyNSD and all baselines. We also provide extended quantitative results that complement the main trends reported in [section 4](#).

### C.1. Hyper-Parameters

This section collects the full hyper-parameter search space used in the experiments in [section 4](#). The final reported test-set accuracy for each run is chosen from the checkpoint that achieved the highest validation accuracy. All experiments were run on a single *NVIDIA A100-SXM4-80GB* GPU. For what concerns *real datasets*, [Table 5](#) lists the hyperparameters and their searchable values/ranges used in the experiments, reflecting the same choices of ([Bodnar et al., 2022](#)). For *synthetic datasets*, we evaluate three families of settings mirroring the experiments in ([Caralt et al., 2024](#)): *Heterophily*, *Feature Noise*, and *Amount of Data*, each instantiated in two columns (DIFF on the right and RISNN on the left), which differ only in feature dimensionality and a few graph knobs. [Table 6](#) summarises the common training setup and [Table 7](#) the panel-specific grids.

### C.2. Datasets

**Real-World Node-Classification Benchmarks.** For real-world experiments we use the standard node-classification benchmarks commonly adopted in the sheaf-learning and heterophily literature: TEXAS, WISCONSIN, FILM, SQUIRREL, CHAMELEON, CORNELL, CITESEER, PUBMED, and CORA. Below we briefly recall their construction.

*WebKB (Cornell, Texas, Wisconsin).* Nodes correspond to webpages from the computer science departments of the respective universities, and edges are hyperlinks between pages. Node features are bag-of-words representations of page content. The node labels distinguish different page types (e.g., student, project, course, staff, faculty).

- *WikipediaNetwork (Chameleon, Squirrel).* Nodes are Wikipedia pages and edges denote hyperlinks, while the node features are derived from page content, and labels denote page categories/roles.
- *Film.* In the FILM graph, nodes correspond to actors and edges connect actors co-occurring on the same Wikipedia page or film. Node features are keyword-based descriptors, while the task is multi-class node classification.
- *Citation graphs (Cora, Citeseer, PubMed).* Nodes represent scientific articles, edges encode citation relations. Node features are bag-of-words or standard pre-computed attributes, and the task is to classify each article into a subject category.

[Table 4](#) reports the basic statistics used throughout our experiments: homophily level  $h$  (fraction of edges whose endpoints

Table 4. Real-World dataset statistics.

Dataset	Homophily $h$	#Nodes	#Edges	#Classes
Texas	0.11	183	295	5
Wisconsin	0.21	251	466	5
Film	0.22	7,600	26,752	5
Squirrel	0.22	5,201	198,493	5
Chameleon	0.23	2,277	31,421	5
Cornell	0.30	183	280	5
Citeseer	0.74	3,327	4,676	7
Pubmed	0.80	18,717	44,327	3
Cora	0.81	2,708	5,278	6

Table 5. Hyper-parameter search space.

Hyper-parameter	Searchable values / notes
Hidden channels	{8, 16, 32} (WebKB) and {8, 16, 32, 64} (others)
Stalk width $d$	{1, 2, ..., 5}
Layers	{1, 2, ..., 8}
Poly degree $K$	{2, 3, 4, 5, 8, 12, 16} (for PolySD / Chebyshev)
Learning rate	0.02 (WebKB) and 0.01 (others)
Activations	ELU
Weight decay (model)	Log-uniform (exponent range e.g. [-4.5, 11.0])
Sheaf decay	Log-uniform (exponent range e.g. [-4.5, 11.0])
Input dropout	categorical {0.0, 0.1, ..., 0.9}
Layer dropout	Uniform [0.0, 0.9]
Patience (epochs)	100 (Wiki) and 200 (others)
Max training epochs	1000 (Wiki) and 500 (others)
Optimiser	Adam ( $\beta_1 = 0.9$ , $\beta_2 = 0.999$ )
Misc model flags	left/right weights, normalised, use_act, edge_weights, etc.

share the same label), number of nodes, number of edges, and number of classes. These match the statistics and fixed-split protocol used in the sheaf literature: for each dataset we adopt the per-class 48%/32%/20% train/validation/test protocol and average results over the same 10 fixed splits as in prior work.

### C.2.1. SYNTHETIC BENCHMARKS

For the controlled stress tests, we adopt the synthetic benchmark of (Caralt et al., 2024), which explicitly decouples (i) feature complexity, (ii) graph connectivity, and (iii) label structure. Each graph instance is specified by:  $N$  (number of nodes),  $K$  (even base degree of a regular ring lattice before rewiring),  $n_c$  (number of balanced classes),  $het \in [0, 1]$  (heterophily coefficient controlling inter-/intra-class edges) and  $\sigma \geq 0$  (feature noise level). We briefly recall the feature and graph generation steps below.

*Feature Generation: non-linear Class Manifolds with Shared Mean.* We construct class-specific, non-linearly separable features while enforcing a common mean across classes. This makes naive averaging ineffective while preserving class structure under non-trivial aggregation. Let  $n_{\text{data}}$  be the feature dimension,  $n_h$  an auxiliary latent dimension, and  $n_c$  the number of classes. The process is detailed as follows:

1. Draw class prototypes  $v_k \sim \mathcal{U}([0, 1]^{n_{\text{data}}})$  for  $k = 1, \dots, n_c$ .
2. Define a fixed non-linear map  $f : \mathbb{R}^{n_h} \rightarrow \mathbb{R}^{n_{\text{data}}}$  as the sine-cosine embedding of the  $(n_h - 1)$ -sphere. We sample angles  $\theta_0, \dots, \theta_{n_h-3} \sim \mathcal{U}([0, \pi])$  and  $\theta_{n_h-2} \sim \mathcal{U}([0, 2\pi])$ , construct  $s \in \mathbb{S}^{n_h-1}$  via standard hyperspherical coordinates, and set  $z = f(\theta)$  after truncating/tiling to length  $n_{\text{data}}$ .
3. For a node of class  $k$ , we sample  $\theta$  as above and set the raw feature  $x_{\text{raw}} = v_k \odot f(\theta)$ , where  $\odot$  denotes element-wise multiplication, yielding an ellipsoidal shell per class.
4. We centre features to enforce a shared expected value across classes  $\mu = \frac{1}{N} \sum_{i=1}^N x_{\text{raw},i}$ ,  $\tilde{x}_i = x_{\text{raw},i} - \mu$ .
5. Finally, we add i.i.d. Gaussian noise  $\epsilon_i \sim \mathcal{N}(0, \sigma^2 I)$  and optionally rescale  $x_i = \tilde{x}_i + \epsilon_i$ .

*Graph Generation: Ring-rewire with Class-aware Mixing.* Connectivity is generated independently of features and controlled by the heterophily index  $het$ . The graph generation process consists in:

1. Assign classes almost uniformly so that  $|C_k| \approx N/n_c$ .
2. Build a regular ring lattice of degree  $K$ , being  $E = \{(i, j) : 0 < \min(|i-j|, N-|i-j|) \leq K/2\}$ .
3. Define the class-transition matrix  $R^c = (1 - het) I_{n_c} + \frac{het}{n_c - 1} (\mathbf{1}\mathbf{1}^\top - I_{n_c})$  so that  $\Pr(\text{same class}) = 1 - het$  and each different class has probability  $het/(n_c - 1)$ .
4. For each node  $i$  and each of its  $K/2$  ‘‘rightmost’’ edges, rewire with probability  $p$ , we sample a target class  $c' \sim \text{Categorical}((R^c)_{c_i, \cdot})$ , where  $c_i$  is the class of node  $i$  and choose  $j$  uniformly among nodes in class  $c'$  that are not  $i$  and not already adjacent to  $i$ , and replace the endpoint with  $j$ . We then de-duplicate multi-edges and remove self-loops. The average degree remains  $K$ , while the expected fraction of inter-class edges equals  $het$ .

We consider two synthetic regimes (RISNN and DIFF) that differ only in feature dimensionality and a few graph knobs, following (Caralt et al., 2024).

Table 6. Synthetic experiments common training hyper-parameters.

Hyper-parameter	Value / note
Models	DiagSheafChebyshev, BundleSheafChebyshev, GeneralSheafChebyshev
Optimiser	Adam (learning rate 0.01)
Weight decay	$5 \times 10^{-4}$
Sheaf decay	$5 \times 10^{-4}$
Max epochs / Patience	1500 / 200
Seed	43
Device	single NVIDIA A100-SXM4-80GB
Dataset flag	dataset = synthetic_exp, ellipsoids = false, edge_noise = 0.0

Table 7. Synthetic experiments panel-specific grids.

Family (Fig)	Column	#Classes	#Feats	#Nodes	Degree	Feat noise	Heterophily ( <i>het</i> )
Heterophily	Diff	{2, 3, 4, 5}	4	{400, 600, 800, 1000}	4	0.0	{0.0, 0.25, 0.50, 0.75, 1.0}
Heterophily	RiSNN	{2, 3, 4, 5}	15	{400, 600, 800, 1000}	4	0.0	{0.0, 0.25, 0.50, 0.75, 1.0}
Feature Noise	Diff	2	3	400	2	{0.0, 0.2, 0.4, 0.6, 0.8, 1.0}	1.0
Feature Noise	RiSNN	2	15	500	5	{0.0, 0.05, 0.1, 0.15, 0.2, 0.25, 0.30}	1.0
Amount of Data	Diff	3	3	{100, 500, 1000}	{2, 6, 10}	0.0	0.9
Amount of Data	RiSNN	3	15	{100, 500, 1000}	{2, 6, 10}	0.0	0.9

### C.3. Stalk Dimension vs. Accuracy

In this subsection here we detail the results obtained in Table 4 about the stalk dimensionality impact on the accuracy. This experiment aims to isolate the effect of stalk dimension on real-world performance. As previously seen, the stalk dimension  $d$  controls the size of the local sheaf fibres and therefore the dimensionality of the features transported along edges. In prior sheaf models, relatively large stalks, with  $d \approx 4$ , were often used by default and occasionally increased further in search of improved expressivity. To quantify how much PolyNSD depends on stalk size, we sweep  $d \in \{2, 3, 4, 5\}$  on a representative subset of datasets spanning different homophily regimes: CORA, PUBMED (homophilous citation graphs) and TEXAS, FILM (strongly heterophilous graphs). For each dataset, we run all three PolyNSD variants (Diagonal, Bundle, and General transports). Within each dataset-variant pair, we fix all architectural hyperparameters to the default PolyNSD configuration (depth  $L = 2$ , hidden width 32, Chebyshev parameterisation, same regularisation and optimiser settings) and vary only the stalk dimension  $d$ , training on the standard 10 fixed splits. We then report mean±std test accuracy across the 10 runs.

**Findings: PolyNSD maintains SOTA results across depth.** The results we get are summarised in Figure 5 and show that on PUBMED and FILM, accuracies are essentially flat within error bars as  $d$  varies, indicating that increasing stalk dimension beyond  $d = 2$  brings no systematic benefit. On CORA and TEXAS we observe mild, non-monotonic trends: performance can slightly increase when moving from  $d = 2$  to  $d = 3$ , but often degrades again for  $d \geq 4$ . The strongest configurations on all four datasets typically occur at *small stalk dimensions* ( $d \in \{2, 3\}$ ). Larger stalks do not lead to clear improvements and can even hurt performance through over-parameterisation and increased optimisation difficulty. This contrasts with earlier sheaf architecture settings, where  $d = 4$  emerged as a de facto default and larger stalks were sometimes required to approach state-of-the-art performance. This is because polynomial diffusion on the sheaf Laplacian compensates for the reduced stalk dimensionality, where expressive spectral filters and explicit parallel transport allows us to achieve near state-of-the-art accuracy with compact stalks, motivating the choice of low  $d$  in the main experiments.

### C.4. Depth Robustness and Oversmoothing

In this subsection, we will better investigate how PolyNSD behaves as depth increases, compared to classical GNNs and other sheaf models. We consider four representative datasets: CORA, CITESEER (homophilous citation graphs), and CORNELL, CHAMELEON (heterophilous benchmarks). For each model we sweep the number of layers  $L \in \{2, 4, 8, 16, 32\}$ , keeping all other hyperparameters fixed. For each model-depth pair, we report test accuracy mean±std over the 10 fixed splits, and we additionally highlight, for each model, the depth at which its best test accuracy is achieved. The complete results are given in Table 8. This makes explicit the qualitative patterns summarised in the main text: GCN and Geom-GCN deteriorate

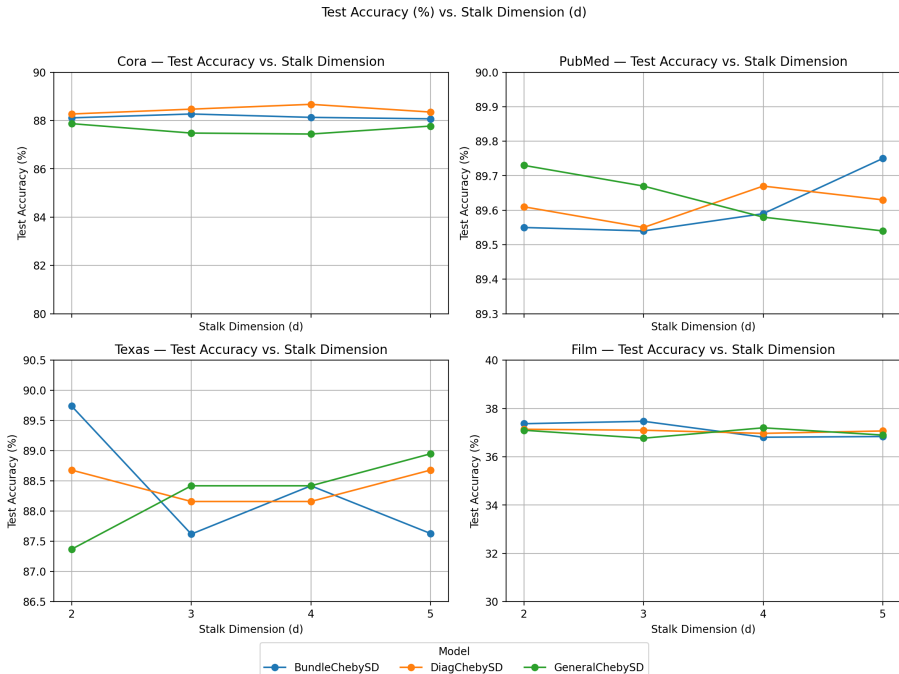


Figure 5. Test accuracy vs. stalk dimension  $d \in \{2, 3, 4, 5\}$ . We sweep  $d$  on four real-world datasets over the three versions, keeping fixed the other hyperparameters.

quickly with depth (often approaching random performance on heterophilous graphs), GAT runs into numerical instability at high depth, GCNII and SAN/ANSD provide strong deep baselines, and PolyNSD variants remain competitive and stable up to  $L = 32$  layers, especially on the heterophilous benchmarks.

**Dirichlet-energy Diagnostics on Heterophily.** To complement the depth sweep in Table 8, we add a *representation-level* diagnostic that probes how the intermediate signals evolve as depth increases on heterophilous graphs. In particular, we focus on the two canonical heterophily benchmarks CHAMELEON and SQUIRREL and track the (normalized) Dirichlet energy of intermediate representations produced by NSD and PolyNSD. Accuracy as a function of depth (as in Table 8) reveals whether a method degrades as layers increase, but it does not reveal *why* a degradation might occur. In deep message passing, poor depth scaling can arise either from oversmoothing (collapse to an overly low-frequency subspace, which is reconducible to have Dirichlet Energy = 0) or from the opposite failure mode, a.k.a. *Energy Amplification*, where intermediate representations become increasingly “rough” with respect to the learned propagation operator, yielding unstable depth-wise dynamics. The goal here is to quantify whether a model exhibits *controlled propagation* as depth increases, i.e., whether the representation variation induced by the learned transport remains bounded and predictable.

**Measuring channel-averaged Normalised Dirichlet-Energy** Let  $x_\ell \in \mathbb{R}^{(Nd) \times C}$  be the intermediate sheaf representation after the  $\ell$ -th propagation (diffusion/filter) step, and let  $L$  denote the sparse Laplacian-like operator applied at the probed point in the layer. We compute the channel-averaged normalised Dirichlet energy as  $E_{\text{norm}}(x_\ell) = \frac{\langle x_\ell, Lx_\ell \rangle}{\langle x_\ell, x_\ell \rangle}$ , and report the depth-wise trajectory  $\{E_{\text{norm}}(x_\ell)\}_{\ell=1}^L$ . Here, larger values indicate higher variation with respect to the learned transport, while smaller values indicate increased alignment with the low-energy modes of  $L$ . We train NSD and PolyNSD with identical routines and log  $E_{\text{norm}}(x_\ell)$  at the best validation checkpoint. We repeat over a controlled grid of settings: seeds  $\in \{0, 1, 2\}$ , stalk dimensions  $d \in \{2, 3, 4\}$ , and depths  $L \in \{2, 3, 4\}$ , for each transport class (Diagonal, Bundle, General). For each (dataset, transport class, method) group we aggregate all runs (total  $n = 27$ ) and plot mean $\pm$ std per layer.

**Findings: PolyNSD Controls Propagation Energy.** Across both heterophilous datasets and all transport classes, we observe a consistent qualitative separation in which *NSD shows high and increasing energy with depth*, while *PolyNSD produces substantially lower energy and more stable trajectories*. More specifically, we have that NSD trajectories typically

Table 8. Depth ablation study: studying oversmoothing presence. We report accuracy  $\pm$  stdev for real-world datasets used to study the oversmoothing effect. The “best” result corresponds to the number of layers with the highest accuracy. “OOM” denotes out-of-memory and “INS” numerical instability. The top three models for each dataset and layer are coloured by **First**, **Second** and **Third**, respectively.

Layers	2	4	8	16	32	Best
Cora ( $h=0.81$ )						
DiagChebySD	<b>88.67<math>\pm</math>1.29</b>	<b>88.23<math>\pm</math>1.36</b>	<b>88.11<math>\pm</math>1.08</b>	<b>87.73<math>\pm</math>1.64</b>	87.22 $\pm$ 1.64	2
BundleChebySD	<b>87.95<math>\pm</math>1.31</b>	87.75 $\pm$ 1.49	<b>87.87<math>\pm</math>1.90</b>	<b>88.01<math>\pm</math>1.46</b>	87.36 $\pm$ 1.49	16
GeneralChebySD	87.44 $\pm$ 1.09	<b>87.77<math>\pm</math>1.24</b>	87.48 $\pm$ 1.25	86.92 $\pm$ 1.18	86.90 $\pm$ 1.48	4
SAN	86.90 $\pm$ 1.31	86.84 $\pm$ 0.97	86.68 $\pm$ 1.13	86.54 $\pm$ 0.89	86.62 $\pm$ 1.39	2
ANSD	86.98 $\pm$ 1.07	87.08 $\pm$ 1.26	86.80 $\pm$ 1.15	86.84 $\pm$ 1.24	<b>86.56<math>\pm</math>0.75</b>	4
GGCN	87.00 $\pm$ 1.15	87.48 $\pm$ 1.32	87.63 $\pm$ 1.33	<b>87.51<math>\pm</math>1.19</b>	<b>87.95<math>\pm</math>1.05</b>	32
GPRGNN	<b>87.93<math>\pm</math>1.11</b>	<b>87.95<math>\pm</math>1.18</b>	<b>87.87<math>\pm</math>1.41</b>	87.26 $\pm$ 1.51	87.18 $\pm$ 1.29	4
H2GCN	87.87 $\pm$ 1.20	86.10 $\pm$ 1.51	86.18 $\pm$ 2.10	OOM	OOM	2
GCNII	85.35 $\pm$ 1.56	85.35 $\pm$ 1.48	86.38 $\pm$ 0.98	87.12 $\pm$ 1.11	<b>87.95<math>\pm</math>1.23</b>	64
PairNorm	85.79 $\pm$ 1.01	85.07 $\pm$ 0.91	84.65 $\pm$ 1.09	82.21 $\pm$ 2.84	60.32 $\pm$ 8.28	2
Geom-GCN	85.35 $\pm$ 1.57	21.01 $\pm$ 2.61	13.98 $\pm$ 1.48	13.98 $\pm$ 1.48	13.98 $\pm$ 1.48	2
GCN	86.98 $\pm$ 1.27	83.24 $\pm$ 1.56	31.03 $\pm$ 3.08	31.05 $\pm$ 2.36	30.76 $\pm$ 3.43	2
GAT	87.30 $\pm$ 1.10	86.50 $\pm$ 1.20	84.97 $\pm$ 1.24	INS	INS	2
Citeseer ( $h=0.74$ )						
DiagChebySD	<b>77.19<math>\pm</math>1.25</b>	<b>77.12<math>\pm</math>1.61</b>	76.54 $\pm$ 1.93	76.71 $\pm$ 2.50	76.34 $\pm$ 1.24	2
BundleChebySD	76.98 $\pm$ 1.76	<b>77.57<math>\pm</math>1.55</b>	<b>76.97<math>\pm</math>1.90</b>	<b>76.87<math>\pm</math>1.51</b>	<b>77.26<math>\pm</math>1.99</b>	4
GeneralChebySD	<b>77.82<math>\pm</math>1.68</b>	76.75 $\pm$ 1.59	76.62 $\pm$ 1.04	75.87 $\pm$ 1.69	75.11 $\pm$ 1.86	2
SAN	76.27 $\pm$ 1.76	76.30 $\pm$ 1.80	76.62 $\pm$ 1.70	76.18 $\pm$ 1.47	76.07 $\pm$ 2.18	8
ANSD	76.99 $\pm$ 1.74	76.86 $\pm$ 1.71	76.61 $\pm$ 1.51	76.69 $\pm$ 1.56	76.22 $\pm$ 1.47	2
GGCN	76.83 $\pm$ 1.82	76.77 $\pm$ 1.48	<b>76.91<math>\pm</math>1.56</b>	<b>76.88<math>\pm</math>1.56</b>	<b>76.97<math>\pm</math>1.52</b>	10
GPRGNN	77.13 $\pm$ 1.67	<b>77.05<math>\pm</math>1.43</b>	<b>77.09<math>\pm</math>1.62</b>	76.00 $\pm$ 1.64	74.97 $\pm$ 1.47	2
H2GCN	76.90 $\pm$ 1.80	76.09 $\pm$ 1.54	74.10 $\pm$ 1.83	OOM	OOM	1
GCNII	75.42 $\pm$ 1.78	75.29 $\pm$ 1.90	76.00 $\pm$ 1.66	<b>76.96<math>\pm</math>1.38</b>	<b>77.33<math>\pm</math>1.48</b>	32
PairNorm	73.59 $\pm$ 1.47	72.62 $\pm$ 1.97	72.32 $\pm$ 1.58	59.71 $\pm$ 15.97	27.21 $\pm$ 10.95	2
Geom-GCN	<b>78.02<math>\pm</math>1.15</b>	23.01 $\pm$ 1.95	7.23 $\pm$ 0.87	7.23 $\pm$ 0.87	7.23 $\pm$ 0.87	2
GCN	76.50 $\pm$ 1.36	64.33 $\pm$ 8.27	24.18 $\pm$ 1.71	23.07 $\pm$ 2.95	25.3 $\pm$ 1.77	2
GAT	76.55 $\pm$ 1.23	75.33 $\pm$ 1.39	66.57 $\pm$ 5.08	INS	INS	2
Cornell ( $h=0.3$ )						
DiagChebySD	<b>85.40<math>\pm</math>5.16</b>	<b>85.13<math>\pm</math>5.57</b>	<b>85.68<math>\pm</math>7.36</b>	84.05 $\pm$ 8.41	81.62 $\pm$ 6.92	8
BundleChebySD	<b>85.40<math>\pm</math>7.95</b>	<b>84.86<math>\pm</math>5.82</b>	84.59 $\pm$ 7.05	<b>85.13<math>\pm</math>8.31</b>	<b>84.59<math>\pm</math>7.93</b>	2
GeneralChebySD	<b>85.13<math>\pm</math>6.19</b>	<b>84.86<math>\pm</math>6.42</b>	84.32 $\pm$ 6.49	81.62 $\pm$ 7.53	81.35 $\pm$ 6.22	2
SAN	82.70 $\pm$ 6.64	84.59 $\pm$ 4.69	<b>85.68<math>\pm</math>4.53</b>	<b>84.32<math>\pm</math>6.82</b>	<b>83.51<math>\pm</math>7.20</b>	8
ANSD	84.86 $\pm$ 6.07	84.32 $\pm$ 5.10	84.86 $\pm$ 5.95	<b>84.59<math>\pm</math>6.51</b>	83.24 $\pm$ 3.97	8
GGCN	83.78 $\pm$ 6.73	83.78 $\pm$ 6.16	<b>84.86<math>\pm</math>5.69</b>	83.78 $\pm$ 6.73	<b>83.78<math>\pm</math>6.51</b>	6
GPRGNN	76.76 $\pm$ 8.22	77.57 $\pm$ 7.46	80.27 $\pm$ 8.11	78.38 $\pm$ 6.04	74.59 $\pm$ 7.66	8
H2GCN	81.89 $\pm$ 5.98	82.70 $\pm$ 6.27	80.27 $\pm$ 6.63	OOM	OOM	1
GCNII	67.57 $\pm$ 11.34	64.59 $\pm$ 9.63	73.24 $\pm$ 5.91	77.84 $\pm$ 3.97	75.41 $\pm$ 5.47	16
PairNorm	50.27 $\pm$ 7.17	53.51 $\pm$ 8.00	58.38 $\pm$ 5.01	58.38 $\pm$ 3.01	58.92 $\pm$ 3.15	32
Geom-GCN	60.54 $\pm$ 3.67	23.78 $\pm$ 11.64	12.97 $\pm$ 2.91	12.97 $\pm$ 2.91	12.97 $\pm$ 2.91	2
GCN	60.54 $\pm$ 5.30	59.19 $\pm$ 3.30	58.92 $\pm$ 3.15	58.92 $\pm$ 3.15	58.92 $\pm$ 3.15	2
GAT	61.89 $\pm$ 5.05	58.38 $\pm$ 4.05	58.38 $\pm$ 3.86	INS	INS	2
Chameleon ( $h=0.23$ )						
DiagChebySD	<b>69.50<math>\pm</math>1.81</b>	<b>70.39<math>\pm</math>1.66</b>	<b>70.04<math>\pm</math>2.87</b>	<b>68.99<math>\pm</math>4.13</b>	66.78 $\pm$ 3.99	4
BundleChebySD	<b>67.13<math>\pm</math>1.63</b>	<b>67.13<math>\pm</math>3.59</b>	66.03 $\pm$ 1.70	66.51 $\pm$ 2.11	66.47 $\pm$ 2.79	2
GeneralChebySD	63.29 $\pm$ 2.47	65.22 $\pm$ 1.72	58.55 $\pm$ 3.43	61.80 $\pm$ 4.64	65.17 $\pm$ 5.19	4
SAN	65.88 $\pm$ 2.10	65.99 $\pm$ 1.28	<b>68.16<math>\pm</math>2.18</b>	<b>68.62<math>\pm</math>2.81</b>	<b>67.61<math>\pm</math>2.80</b>	16
ANSD	65.35 $\pm$ 1.26	<b>67.11<math>\pm</math>1.88</b>	66.69 $\pm$ 2.30	67.39 $\pm$ 1.84	<b>66.91<math>\pm</math>1.61</b>	16
GGCN	<b>70.77<math>\pm</math>1.42</b>	69.58 $\pm$ 2.68	<b>70.33<math>\pm</math>1.70</b>	<b>70.44<math>\pm</math>1.82</b>	<b>70.29<math>\pm</math>1.62</b>	5
GPRGNN	46.58 $\pm$ 1.77	45.72 $\pm$ 3.45	41.16 $\pm$ 5.79	39.58 $\pm$ 7.85	35.42 $\pm$ 8.52	2
H2GCN	59.06 $\pm$ 1.85	60.11 $\pm$ 2.15	OOM	OOM	OOM	4
GCNII	61.07 $\pm$ 4.10	63.86 $\pm$ 3.04	62.89 $\pm$ 1.18	60.20 $\pm$ 2.10	56.97 $\pm$ 1.81	4
PairNorm	62.74 $\pm$ 2.82	59.01 $\pm$ 2.80	54.12 $\pm$ 2.24	46.38 $\pm$ 2.23	46.78 $\pm$ 2.26	2
Geom-GCN	60.00 $\pm$ 2.81	19.17 $\pm$ 1.66	19.58 $\pm$ 1.73	19.58 $\pm$ 1.73	19.58 $\pm$ 1.73	2
GCN	64.82 $\pm$ 2.24	53.11 $\pm$ 4.44	35.15 $\pm$ 3.14	35.39 $\pm$ 3.23	35.20 $\pm$ 3.25	2
GAT	60.26 $\pm$ 2.50	48.71 $\pm$ 2.96	35.09 $\pm$ 3.55	INS	INS	2

grow monotonically with  $\ell$ , indicating that intermediate signals become progressively more varying with respect to the learned transport operator. This is consistent with an *energy amplification* regime, where deeper propagation accumulates higher-frequency components in the representation space. On the other hand, PolyNSD yields markedly smaller  $E_{\text{norm}}$  values and a smoother depth-wise evolution, suggesting that the polynomial parameterisation learns a propagation rule with *better-conditioned* spectral behaviour. This result, in relation to depth robustness, provides an explanatory lens: compared to NSD, PolyNSD induces *tighter control* over the variation of intermediate representations with depth, preventing the progressive energy growth observed in NSD.

### C.5. Oversquashing Diagnostics via Long-Range Influence Decay

The depth robustness study in subsection C.4 probes how performance changes as we increase the number of propagation steps. However, poor long-range performance can also arise from a distinct failure mode: *oversquashing*, where information (and gradients) from distant nodes is compressed through repeated local aggregation and graph bottlenecks, making far-away evidence effectively unusable. Since PolyNSD introduces an explicit *spectral* (polynomial) component that can realise multi-hop mixing within a shallow stack, it is natural to ask whether it improves long-range *influence* compared to classical (layer-by-layer) neural sheaf diffusion (NSD). We therefore complement the depth/energy diagnostics with a gradient-based *influence decay* probe.

More formally, let  $x \in \mathbb{R}^{N \times F}$  be the input node features and let  $s_v(x)$  denote a scalar score for a target node  $v$  (in practice, we use the logit or log-probability of the ground-truth class at  $v$ ). For a source node  $u$ , we quantify how much  $u$  can affect the prediction at  $v$  by the gradient magnitude:  $G(u \rightarrow v) = \left\| \frac{\partial s_v}{\partial x_u} \right\|_2$ . We then aggregate gradients by hop distance. Let  $\text{dist}(u, v)$  be the shortest-path distance on the input graph. For each hop  $d \in \{0, \dots, D\}$  we define the distance-binned influence as:

$$I(d) = \mathbb{E}_{v \in \mathcal{T}} \left[ \frac{1}{|\{u : \text{dist}(u, v) = d\}|} \sum_{u: \text{dist}(u, v) = d} \left\| \frac{\partial s_v}{\partial x_u} \right\|_2 \right] \quad (98)$$

where  $\mathcal{T}$  is a set of sampled target nodes (e.g., from the evaluation split). Finally, we plot a normalised curve to focus on the *rate of decay*  $\tilde{I}(d) = \frac{I(d)}{I(0)}$ . A steep collapse of  $\tilde{I}(d)$  with  $d$  indicates that distant nodes have vanishing influence on

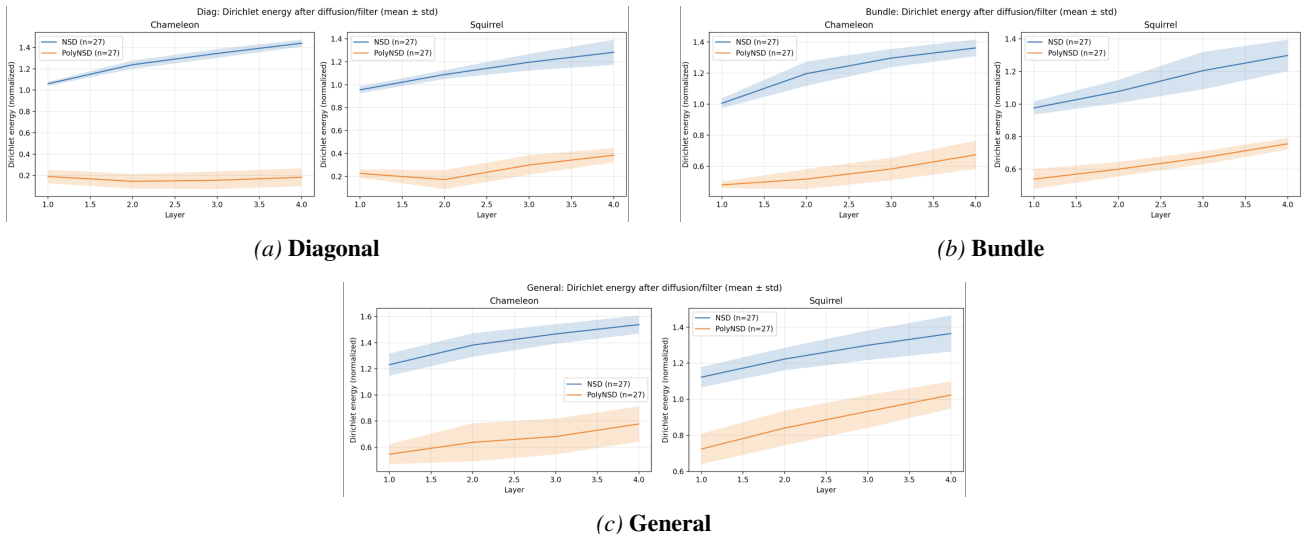


Figure 6. *Dirichlet-energy diagnostics on heterophily.* Normalized Dirichlet energy trajectories on CHAMELEON and SQUIRREL for NSD vs. PolyNSD across transport classes.

predictions (a hallmark of oversquashing), whereas a slower decay indicates improved long-range sensitivity.

**Experimental protocol.** We evaluate this diagnostic on three standard benchmarks with different structural regimes: the heterophilous SQUIRREL and CHAMELEON, and the homophilous PUBMED. For each dataset, we compare all three transport classes (Diagonal, Bundle, General) and both diffusion families (NSD vs. PolyNSD), yielding six curves per dataset. To compare “many local steps” against “few spectral steps”, we follow a matched-reach heuristic: NSD is run with a deeper stack ( $L_{NSD} = 6$ ), whereas PolyNSD uses fewer layers ( $L_{Poly} = 2$ ) but a higher polynomial degree ( $K = 10$ ), providing explicit multi-hop mixing per layer. For each trained model, we sample a set  $\mathcal{T}$  of target nodes from the evaluation split, compute  $\nabla_x s_v$  via backpropagation, and aggregate  $\|\partial s_v / \partial x_u\|_2$  into hop-distance bins up to a fixed maximum distance  $D$  (here  $D = 10$ ), where hop distances are computed via BFS on the undirected version of the input graph. We report  $\tilde{I}(d)$  on a log-scale for readability and clamp extremely small values only for plotting stability.

**Findings: PolyNSD Mitigates Long-Range Influence Collapse.** Figure 7 shows a consistent qualitative separation across all three datasets and all transport classes. In particular, we have that:

- *NSD exhibits rapid long-range influence decay.* For Diagonal and Bundle transports,  $\tilde{I}(d)$  drops sharply as  $d$  increases and approaches numerical underflow at larger distances (often by  $d \approx 8-10$ ), indicating that far nodes have essentially no effect on predictions, being consistent with an oversquashing regime.
- *PolyNSD preserves substantially higher long-range influence.* Across SQUIRREL, CHAMELEON, and PUBMED, PolyNSD variants maintain larger  $\tilde{I}(d)$  at intermediate-to-large hop distances, often separated from NSD by multiple orders of magnitude at  $d = 10$ . This results, therefore into an improved gradient flow and greater sensitivity to distant nodes. The slower decay of  $\tilde{I}(d)$  empirically supports this hypothesis: PolyNSD sustains usable long-range influence where NSD collapses.
- *Richer transports benefit most from the spectral component.* While all PolyNSD variants improve long-range influence relative to their NSD counterparts, the effect is typically strongest for *Bundle-Poly* and *General-Poly*, suggesting that combining expressive transports with polynomial spectral filtering yields the most robust long-range dependency handling.

As shown in Figure 7, for strictly local diffusion updates, an NSD model of depth  $L$  can only depend on nodes within  $L$  propagation steps. As a result,  $\tilde{I}(d)$  may exhibit a drop to (near-)zero for  $d > L$  that reflects a finite receptive-field limit. In our setup, GENERAL-NSD experiences a sharp cutoff around  $d \approx 6$  (i.e., negligible gradient sensitivity beyond its depth-limited neighbourhood). The same depth-limited cliff is less pronounced for DIAGONAL-NSD and BUNDLE-NSD,

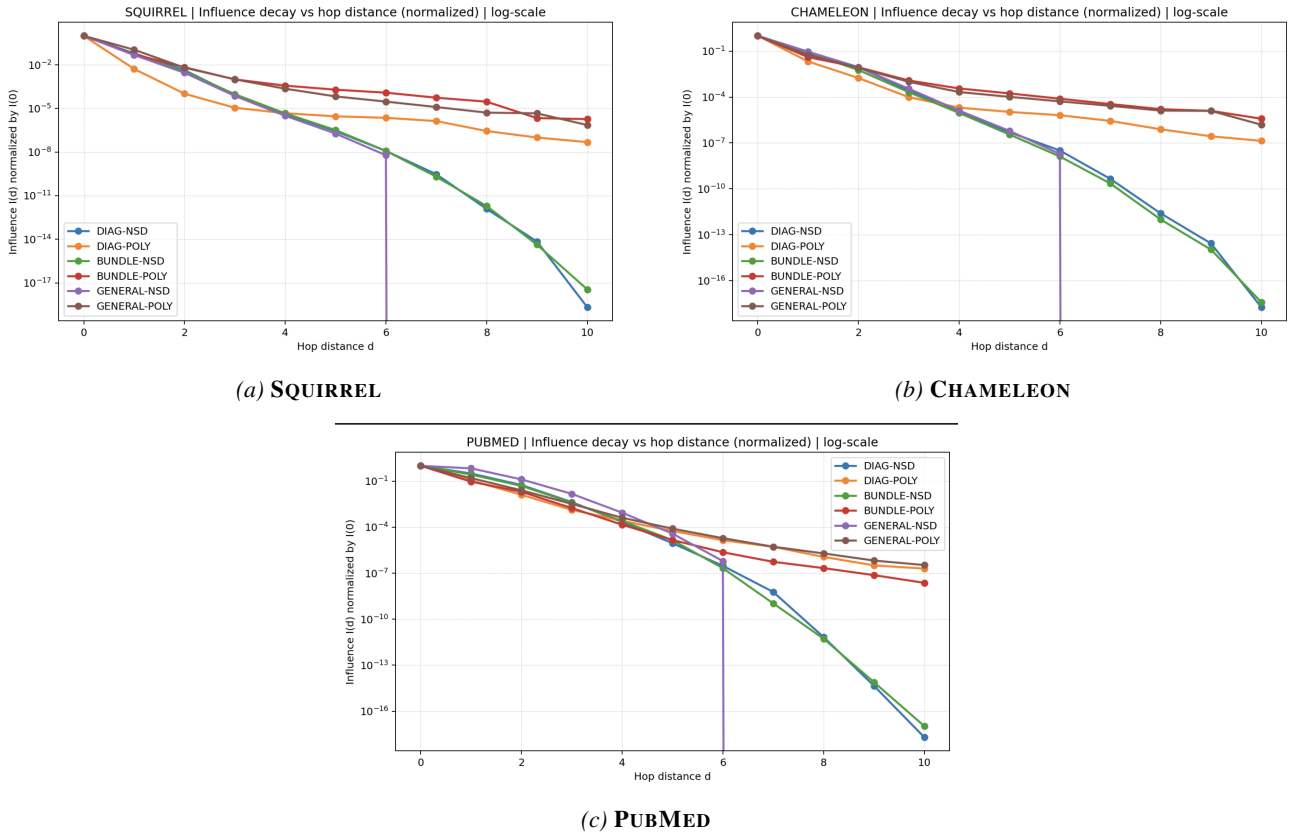


Figure 7. Oversquashing diagnostics via influence decay. Normalised influence  $\tilde{I}(d) = I(d)/I(0)$  (log-scale) as a function of hop distance  $d$  for NSD vs. PolyNSD across the three transport classes (Diagonal, Bundle, General).

meaning that these implementations have a *larger effective propagation radius per nominal layer*, so that non-trivial gradients can persist beyond  $d = L_{\text{NSD}}$  despite matching the same nominal depth parameter. In contrast, GENERAL-PolyNSD continues to display non-trivial influence beyond  $d = 6$  due to its explicit degree- $K$  polynomial filtering, which enables multi-hop mixing within a shallow stack.

### C.6. Chebyshev Order $K$ weep

This section investigates how the polynomial order  $K$  of PolyNSD affects performance and how this interacts with the choice of spectral scaling  $\lambda_{\text{max}}$ . The goal is to understand when higher-order filters are beneficial and to what extent they strictly improve over the  $K=1$  (NSD-equivalent) case. For these ablations we use a controlled configuration shared across all datasets: stalk dimension  $d = 4$ , number of diffusion layers  $L = 2$ , hidden channels 16, and within each dataset and PolyNSD variant, we sweep the polynomial order  $K \in \{1, 2, 4, 8, 12, 16\}$  and the spectral scaling strategy: *analytic* vs *iterative* estimate of  $\lambda_{\text{max}}$ , as described in section 3. We report mean $\pm$ std test accuracy over the 10 splits.

**Homophily and Heterophily Order  $K$ 's Impact.** The results in Figure 8 shows test accuracy as a function of  $K$  for the nine real-world benchmarks, with one panel per dataset. Each panel overlays the six configurations obtained by crossing the three transport classes with the two choices of  $\lambda_{\text{max}}$  estimation. Across datasets : (i) On homophilous graphs such as CORA, CITESEER and PUBMED, moderate orders ( $K \approx 4-8$ ) are often optimal. Increasing  $K$  beyond this range yields diminishing returns. (ii) On heterophilous graphs such as SQUIRREL and CHAMELEON, the optimum shifts towards larger values ( $K \in \{8, 16\}$ ), consistent with the need for longer-range, multi-frequency propagation to stabilise learning under label inconsistency. (iii) For all three transport classes and across all datasets, the best configuration always satisfies  $K > 1$ , meaning that higher-order polynomial filters strictly improve over the NSD-like  $K = 1$  baseline at fixed depth and width.

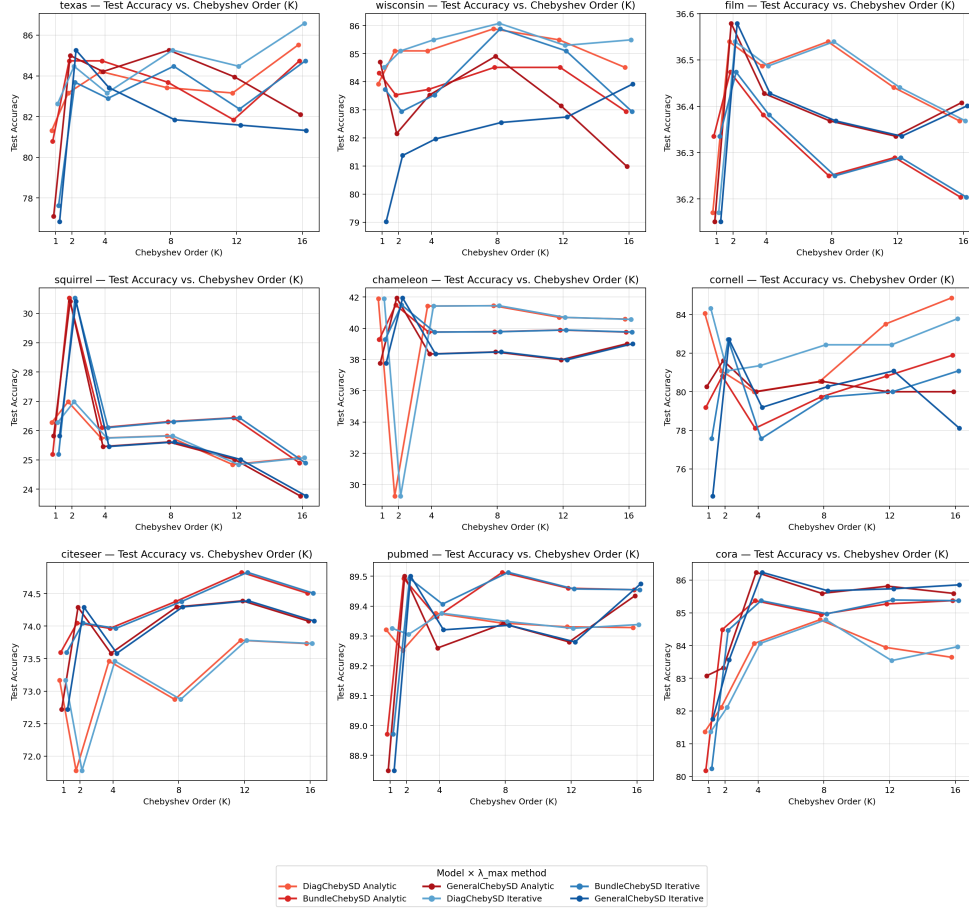


Figure 8. Chebyshev order  $K$  sweep. Test accuracy vs.  $K$  for the nine real-world benchmarks. Each panel corresponds to one dataset and overlays the six configurations given by the three PolyNSD variants crossed with analytic vs. iterative estimates of  $\lambda_{\max}$ . Error bars denote mean $\pm$ std over the 10 fixed splits.

Table 9. PolyNSD (Chebyshev)  $K$ -sweep. The three PolySD variants are held fixed with  $Layers=2$ ,  $StalkDim=4$  and  $Hidden=16$ , and columns sweep  $K \in \{2, 4, 8, 16\}$  are reported, with the associated number of parameters. Top-1 per dataset and model (per-row) are coloured as **First**.

$K$	2	4	6	8	16	Best
<b>PubMed</b> ( $h=0.80$ , $\#N = 18,707$ , $\#E = 44,327$ , $\#C = 3$ )						
<b>DiagChebySD</b>	87.37 $\pm$ 0.45	87.95 $\pm$ 0.60	88.01 $\pm$ 0.39	<b>88.18<math>\pm</math>0.40</b>	87.65 $\pm$ 0.42	8
<i>#params</i>	48,659	48,661	48,663	48,665	48,673	48,665
<b>BundleChebySD</b>	87.86 $\pm$ 0.47	<b>87.91<math>\pm</math>0.32</b>	87.52 $\pm$ 0.45	87.63 $\pm$ 0.37	87.51 $\pm$ 0.74	4
<i>#params</i>	49,619	49,621	49,623	49,625	49,633	49,621
<b>GeneralChebySD</b>	87.74 $\pm$ 0.49	87.80 $\pm$ 0.25	87.62 $\pm$ 0.43	<b>87.87<math>\pm</math>0.49</b>	87.82 $\pm$ 0.49	8
<i>#params</i>	52,499	52,501	52,503	52,505	52,513	52,505
<b>Chameleon</b> ( $h=0.23$ , $\#N = 2,277$ , $\#E = 31,421$ , $\#C = 5$ )						
<b>DiagChebySD</b>	36.27 $\pm$ 2.48	61.21 $\pm$ 10.09	59.36 $\pm$ 10.55	68.55 $\pm$ 2.32	<b>70.57<math>\pm</math>1.32</b>	16
<i>#params</i>	194,821	194,823	194,825	194,827	194,835	194,835
<b>BundleChebySD</b>	59.85 $\pm$ 7.93	61.97 $\pm$ 7.18	66.18 $\pm$ 2.34	<b>66.64<math>\pm</math>2.35</b>	66.58 $\pm$ 9.92	8
<i>#params</i>	195,781	195,783	195,785	195,787	195,795	195,787
<b>GeneralChebySD</b>	62.39 $\pm$ 3.16	66.05 $\pm$ 1.65	65.94 $\pm$ 1.64	62.08 $\pm$ 3.27	<b>67.39<math>\pm</math>2.50</b>	16
<i>#params</i>	198,661	198,663	198,665	198,667	198,675	198,675
<b>Squirrel</b> ( $h=0.22$ , $\#N = 5,201$ , $\#E = 198,493$ , $\#C = 5$ )						
<b>DiagChebySD</b>	35.34 $\pm$ 2.76	46.65 $\pm$ 1.76	43.92 $\pm$ 2.83	47.18 $\pm$ 1.18	<b>47.72<math>\pm</math>1.20</b>	16
<i>#params</i>	174,661	174,663	174,665	174,667	174,675	174,675
<b>BundleChebySD</b>	44.12 $\pm$ 1.65	43.58 $\pm$ 2.26	41.69 $\pm$ 5.56	41.29 $\pm$ 2.55	<b>44.48<math>\pm</math>3.22</b>	16
<i>#params</i>	176,901	174,983	176,903	176,905	176,913	176,913
<b>GeneralChebySD</b>	41.66 $\pm$ 1.42	40.27 $\pm$ 2.69	<b>42.02<math>\pm</math>2.50</b>	40.70 $\pm$ 2.01	41.82 $\pm$ 3.24	6
<i>#params</i>	179,781	179,783	179,785	179,787	179,795	179,785

**Numeric Results: Degree  $K > 1$  is always beneficial.** To provide a more compact view of the effect of  $K$  in the context of the accuracy–efficiency trade-offs, Table 9 reports PolyNSD performance on three datasets with distinct homophily levels: PUBMED (high homophily), CHAMELEON, and SQUIRREL (heterophilous). We fix the depth and width and sweep  $K \in \{2, 4, 6, 8, 16\}$ , reporting for each entry both the test accuracy and the corresponding parameter count. On all three datasets, the best configuration occurs at  $K > 1$ , and increasing  $K$  allows PolyNSD to emulate a wide range of effective propagation depths without changing the number of layers. Here, higher-order sheaf polynomials are shown to strictly enlarge the class of linear operators that can be realised at fixed depth.

### C.7. PolyNSD vs NSD: Detailed Accuracy–Efficiency Analysis

This subsection quantifies how much accuracy can be retained or gained when replacing NSD layers with PolyNSD layers at comparable or reduced parameter counts. We focus on three large benchmarks that cover both homophilous and heterophilous regimes: PUBMED (high homophily), CHAMELEON and SQUIRREL (low homophily). For each dataset and for each transport class, we consider two complementary sweeps: (i) *Depth sweep (NSD)*, where hidden width and stalk dimension are fixed, while the number of NSD layers  $L$  is varied, and (ii) *Width sweep (NSD)*, where depth and stalk dimension are fixed, while the hidden width (number of channels) is varied. For each configuration we record the test accuracy (mean±std over the 10 fixed splits) and the total number of trainable parameters. This allows us to draw iso-accuracy and iso-parameter comparisons between PolyNSD and NSD.

Table 10. PolySD vs NSD: layers sweep. “OOM” stands for out of memory, whilst “N/A” means that the parameter count is not available. We report the best results, for each dataset, for the three PolySD variant, with the associated parameter count. The last column contains the summary of improvements of the PolySD model variant, showing the PolySD **Improvement** or **Deterioration** w.r.t. the NSD Best setting. Top-1 per dataset and model (per-row) are coloured as **First**.

Layers	2	4	8	16	32	Best	PolySD Improvement
<i>PubMed</i> ( $h=0.80$ , $\#N = 18,707$ , $\#E = 44,327$ , $\#C = 3$ )							
DiagChebySD: 88.18±0.40 (K=8), #params=48,665							
BundleChebySD: 87.91±0.32 (K=4), #params=49,621							
GeneralChebySD: 87.87±0.49 (K=8), #params=52,505							
Diag-NSD	87.82±0.55	<b>87.92±0.51</b>	87.92±0.52	65.92±20.39	39.49±1.60	4	<b>+0.26%</b>
#params	48,655	50,507	54,211	61,619	76,435	50,507	-3.65% (-1,842)
Bundle-NSD	87.70±0.56	87.85±0.42	<b>87.94±0.36</b>	87.63±0.47	37.03±4.72	8	<b>-0.03%</b>
#params	49,615	52,427	58,051	69,299	91,795	58,051	-14.52% (-8,430)
General-NSD	87.48±0.64	87.62±0.36	<b>87.72±0.68</b>	39.94±1.03	39.33±2.25	8	<b>+0.15%</b>
#params	52,495	58,187	69,571	92,339	137,875	69,571	-24.53% (-17,066)
<i>Chameleon</i> ( $h=0.23$ , $\#N = 2,277$ , $\#E = 31,421$ , $\#C = 5$ )							
DiagChebySD: 70.57±1.32 (K=16), #params=194,835							
BundleChebySD: 66.64±2.35 (K=8), #params=195,787							
GeneralChebySD: 67.39±2.50 (K=16), #params=198,675							
Diag-NSD	<b>64.43±2.06</b>	61.27±5.14	57.34±6.10	22.92±1.42	22.89±2.59	2	<b>+6.15%</b>
#params	194,817	196,669	200,373	207,781	222,597	194,817	+0.009% (+18)
Bundle-NSD	47.10±10.14	<b>54.08±6.30</b>	50.57±3.53	24.91±2.87	23.05±2.46	4	<b>+12.56%</b>
#params	195,777	198,589	204,213	215,461	237,957	198,589	-1.41% (-2,802)
General-NSD	<b>59.60±4.53</b>	58.18±3.56	26.05±3.41	23.79±3.41	20.07±3.74	2	<b>+7.79%</b>
#params	198,657	204,349	215,733	238,501	284,037	198,657	+0% (+0)
<i>Squirrel</i> ( $h=0.22$ , $\#N = 5,201$ , $\#E = 198,493$ , $\#C = 5$ )							
DiagChebySD: 47.72±1.20 (K=16), #params=174,675							
BundleChebySD: 44.48±3.22 (K=16), #params=176,913							
GeneralChebySD: 42.02±2.50 (K=6), #params=179,785							
Diag-NSD	41.98±1.17	<b>42.60±1.83</b>	42.05±1.54	20.80±1.33	OOM	4	<b>+5.12%</b>
#params	175,937	177,789	181,493	188,901	N/A	177,789	-1.75% (-3,114)
Bundle-NSD	<b>42.46±1.45</b>	42.30±1.83	37.99±2.61	22.86±3.03	OOM	2	<b>+2.02%</b>
#params	176,897	179,709	185,333	196,581	N/A	176,897	+0.009% (+16)
General-NSD	39.11±1.96	<b>39.96±1.76</b>	33.69±1.32	OOM	OOM	4	<b>+2.06%</b>
#params	179,777	185,469	196,853	N/A	N/A	185,469	-3.06% (-5,684)

#### C.7.1. POLYNSD VS NSD: DEPTH SWEEP

In the first comparison we fixed PolyNSD depth to  $L = 2$  and vary its polynomial order  $K$ , while sweeping NSD depth  $L \in \{2, 4, 8, 16, 32\}$  at fixed hidden width 16 and stalk dimension 4. Once chosen the best setting from Table 9, we compare it against the NSD depth sweep. Table 10 summarises the results by reporting, for each dataset and transport class: (i) the best NSD configuration over the depth sweep, (ii) the best PolyNSD configuration over the  $K$  sweep at depth  $L = 2$  and

(iii) the accuracy difference and parameter ratio between PolyNSD and the best NSD configuration.

**Findings: PolyNSD improves performances w.r.t. NSD and it does this with fewer layers.** On PUBMED (homophilic setting), PolyNSD matches or slightly improves over the best NSD configuration with comparable or smaller parameter counts. On CHAMELEON and SQUIRREL (heterophilic settings), PolyNSD yields substantial gains (up to +6%– + 13% accuracy) over NSD at similar or smaller parameter budgets, particularly in the diagonal and bundle variants, highlighting the advantage of higher-order spectral control in heterophilous regimes. An important comment to make is that, if we were to compare PolyNSD and NSD with the same power, we would need to look at the very first column of the layers table. From this, we can notice further improvements: with the same computational power, PolyNSD is extremely stronger than NSD, reaching peaks of +20% in accuracy in heterophilic settings.

### C.7.2. POLYNSD VS NSD: WIDTH SWEEP

We now consider the complementary scenario w.r.t. the previous experiment: we fix NSD depth to  $L = 2$  and sweep the hidden width  $\text{Hidden} \in \{16, 32, 64, 128, 256\}$ , keeping stalk dimension 4 constant. Table 11 reports the corresponding test accuracies and parameter counts, together with the relative improvement of PolyNSD is the best NSD configuration across the width sweep.

**Findings: PolyNSD improves performances w.r.t. NSD and it does this with fewer hidden channels.** On PUBMED and CHAMELEON, PolyNSD matches or exceeds the best NSD performance while using fewer parameters dramatically (often only 1%–20% of the parameters of the widest NSD models). Increasing NSD width beyond a certain point yields only marginal gains at a substantial parameter cost. On SQUIRREL, NSD can sometimes surpass PolyNSD by combining wide layers with large depth, resulting in models with between  $10^6$  and  $10^7$  parameters. However, at equal or smaller parameter budgets, PolyNSD consistently attains higher accuracy, indicating a more favourable accuracy–efficiency frontier.

Table 11. PolySD vs NSD: hidden-channels sweep. “OOM” stands for out of memory, whilst “N/A” means that the parameter count is not available. We also report the best results, for each dataset, for the three PolySD variant, with the associated parameter count. The last column contains the summary of improvements of the PolySD model variant, showing the PolyNSD Improvement or Deterioration w.r.t. the NSD Best setting. Top-1 per dataset and model (per-row) are coloured as First.

Hidden Channels	16	32	64	128	256	Best	PolySD Improvement
<i>PubMed</i> ( $h=0.80$ , $\#N = 18,707$ , $\#E = 44,327$ , $\#C = 3$ )							
<b>DiagChebySD</b> : $88.18 \pm 0.40$ (K=8), $\#params=48,665$							
<b>BundleChebySD</b> : $87.91 \pm 0.32$ (K=4), $\#params=49,621$							
<b>GeneralChebySD</b> : $87.87 \pm 0.49$ (K=8), $\#params=52,505$							
Diag-NSD	$87.82 \pm 0.55$	$87.86 \pm 0.44$	$88.02 \pm 0.53$	<b><math>88.05 \pm 0.46</math></b>	$88.03 \pm 0.50$	128	<b>+0.13%</b>
<i>#params</i>	48,655	111,071	277,375	775,871	2,436,415	775,871	-93.73% (-727,206)
Bundle-NSD	$87.70 \pm 0.56$	$87.83 \pm 0.51$	$87.84 \pm 0.38$	$87.87 \pm 0.56$	<b><math>87.92 \pm 0.44</math></b>	256	<b>-0.01</b>
<i>#params</i>	49,615	112,991	281,215	783,551	2,451,775	2,451,775	-97.98% (-2,402,154)
General-NSD	$87.48 \pm 0.64$	$87.69 \pm 0.53$	$87.71 \pm 0.66$	$87.64 \pm 0.55$	<b><math>87.91 \pm 0.37</math></b>	256	<b>-0.04%</b>
<i>#params</i>	52,495	118,751	292,735	806,591	2,497,855	2,497,855	-97.90% (-2,445,350)
<i>Chameleon</i> ( $h=0.23$ , $\#N = 2,277$ , $\#E = 31,421$ , $\#C = 5$ )							
<b>DiagChebySD</b> : $70.57 \pm 1.32$ (K=16), $\#params=194,835$							
<b>BundleChebySD</b> : $66.64 \pm 2.35$ (K=8), $\#params=195,787$							
<b>GeneralChebySD</b> : $67.39 \pm 2.50$ (K=16), $\#params=198,675$							
Diag-NSD	$64.43 \pm 2.06$	$65.33 \pm 1.78$	<b><math>65.66 \pm 1.61</math></b>	$65.42 \pm 1.09$	$64.78 \pm 1.99$	64	<b>+4.91%</b>
<i>#params</i>	194,817	403,393	862,017	1,945,153	4,774,977	862,017	-77.40% (-667,182)
Bundle-NSD	$46.75 \pm 10.70$	$61.91 \pm 8.76$	$61.53 \pm 7.50$	<b><math>63.68 \pm 1.60</math></b>	$62.10 \pm 2.11$	128	<b>+2.96%</b>
<i>#params</i>	195,777	405,313	865,857	1,952,833	4,790,337	1,952,833	-89.97% (-1,757,046)
General-NSD	$61.12 \pm 2.27$	$64.28 \pm 1.58$	$64.74 \pm 1.46$	<b><math>65.04 \pm 2.13</math></b>	$63.92 \pm 1.75$	128	<b>+2.35%</b>
<i>#params</i>	198,657	411,073	877,377	1,975,873	4,836,417	1,975,873	-89.94% (-1,777,198)
<i>Squirrel</i> ( $h=0.22$ , $\#N = 5,201$ , $\#E = 198,493$ , $\#C = 5$ )							
<b>DiagChebySD</b> : $47.72 \pm 1.20$ (K=16), $\#params=174,675$							
<b>BundleChebySD</b> : $44.48 \pm 3.22$ (K=16), $\#params=176,913$							
<b>GeneralChebySD</b> : $42.02 \pm 2.50$ (K=6), $\#params=179,785$							
Diag-NSD	$41.98 \pm 1.17$	$49.21 \pm 1.87$	$49.35 \pm 1.53$	<b><math>49.59 \pm 1.10</math></b>	$49.51 \pm 1.89$	128	<b>-1.87%</b>
<i>#params</i>	175,937	365,633	786,497	1,794,113	4,472,897	1,794,113	-90.26% (-1,619,438)
Bundle-NSD	$42.46 \pm 1.45$	$47.48 \pm 3.47$	<b><math>49.81 \pm 1.47</math></b>	$48.87 \pm 2.70$	OOM	64	<b>-5.33%</b>
<i>#params</i>	176,897	367,553	790,337	1,801,793	N/A	790,337	-77.62% (-613,424)
General-NSD	$39.11 \pm 1.96$	$39.22 \pm 1.97$	<b><math>42.58 \pm 3.66</math></b>	OOM	OOM	64	<b>-0.56%</b>
<i>#params</i>	179,777	373,313	801,857	N/A	N/A	801,857	-77.58% (-622,072)

### C.8. Spectral-Response Diagnostics Across Homophilic and Heterophilic Regimes

In this appendix subsection, we make some *model diagnostic* and we try to ask to the question *what kind of frequency response* the learned PolyNSD filters implement, and how this behaviour changes across transport classes, network depth  $L$ , stalk dimension  $d$ , and graph regimes (homophilic vs. heterophilic). PolyNSD replaces an affine-in-spectrum diffusion core with a learnable degree- $K$  polynomial in the (sheaf) Laplacian. Raw accuracy tables we have alone do not reveal *how* the model uses its additional spectral expressivity, so the goal here is therefore to provide evidence that PolyNSD learns *non-trivial, dataset-dependent spectral shaping*, and to characterise systematic differences between homophilic and heterophilic datasets.

More formally, for a (sheaf) Laplacian eigenpair  $Lu = \lambda u$ , we saw that a polynomial filter  $p(L)$  acts diagonally in the eigenbasis:  $p(L)u = p(\lambda)u$ . In our implementation, the polynomial is evaluated on the rescaled eigenvalue  $\xi(\lambda) = 2\lambda/\lambda_{\max} - 1 \in [-1, 1]$ . We have also seen that our discrete PolyNSD layers include a high-pass reinjection term controlled by  $\alpha_{\text{hp}}$ , which, under a one-step linearisation, contributes an approximately linear correction proportional to  $(1 - \lambda/\lambda_{\max})$ . For interpretability, we therefore visualise three curves:

$$p(\xi(\lambda)) \quad (\text{polynomial component}), \quad (99)$$

$$\alpha_{\text{hp}} \left(1 - \frac{\lambda}{\lambda_{\max}}\right) \quad (\text{HP correction, approximate}), \quad (100)$$

$$m(\lambda) := p(\xi(\lambda)) + \alpha_{\text{hp}} \left(1 - \frac{\lambda}{\lambda_{\max}}\right) \quad (\text{combined response, approximate}). \quad (101)$$

**Experimental Protocol and Statistics.** We train PolyNSD and then plot the learned spectral response at the best validation checkpoint. We do this for four datasets: two heterophilic (CHAMELEON and SQUIRREL) and two homophilic (CITeseer and PUBMED). We run these experiments across multiple seeds and hyperparameters settings. To make the grid comparable at scale, we compute from the combined response  $m(\lambda)$  some statistics:  $G_{\text{low}}$ , being the mean of  $m(\lambda)$  over the lowest 20% of the spectrum (“low frequencies”).  $G_{\text{high}}$ , being the mean of  $m(\lambda)$  over the highest 20% of the spectrum (“high frequencies”), and finally  $\Delta G = G_{\text{high}} - G_{\text{low}}$ , being a separation measure between high and low spectral regions. We also report `Non-monotone`, being the number of sign changes in  $\frac{d}{d\lambda}m(\lambda)$ , a simple indicator of non-monotonic / band-pass-like behaviour. We report the diagnostic statistics in Table 2, aggregated per dataset over the entire grid. In Figure 9, we show representative learned responses from our grid of 4 datasets.

**Findings: Heterophilic vs. Homophilic Spectral Patterns.** Across the full grid (all models,  $L$ ,  $d$ , and seeds), we observe systematic differences between heterophilic and homophilic datasets. More in particular:

(1) *Homophilic datasets exhibit Stronger Low–High Spectral Separation in the learned response.* Using  $\Delta G$  as a robust separation proxy, homophilic graphs show substantially larger separation. Indeed, in average, we have that *Heterophilic* dataset spectral separation is  $\Delta G = 0.45 \pm 0.14$ , while *Homophilic* one is:  $\Delta G = 1.05 \pm 0.34$ . The reason for that is that the learned filter in homophilic regimes tends to implement a more pronounced “contrast” between different parts of the spectrum. In heterophilic regimes, the separation is milder, consistent with the need to balance information at multiple neighbourhood radii rather than primarily emphasising a single spectral extreme.

(2) *Low-frequency Gain differs sharply between Regimes.* A striking pattern is that  $G_{\text{low}}$  is *never* positive on PUBMED/CITeseer in our grid, while it is frequently positive on heterophilic graphs (the fraction of runs with  $G_{\text{low}} > 0$  is indeed 38.8% (heterophilic) vs. 0.0% (homophilic)). This suggests that heterophilic datasets more often induce filters that *retain or amplify* a portion of low-frequency content, whereas homophilic datasets consistently learn a response that suppresses the lowest end of the spectrum and relies more heavily on the interaction between the polynomial component and the HP reinjection.

(3) *High-pass Reinjection is markedly Stronger on Homophilic datasets.* The learned  $\alpha_{\text{hp}}$  is consistently more negative (larger magnitude) on PUBMED and CITeseer than on CHAMELEON and SQUIRREL. Quantitatively, we have: *Heterophilic* being  $\alpha_{\text{hp}} = -0.25 \pm 0.08$  and *Homophilic* equal to  $\alpha_{\text{hp}} = -0.98 \pm 0.44$ . This indicates that, in homophilic settings, the model uses more the HP skip to counteract oversmoothing and/or to preserve discriminative components that would otherwise be washed out by repeated diffusion.

(4) *Heterophilic Graphs show more Consistently non-Monotone (Band-pass-like) responses.* The learned curves are frequently non-monotone. The heterophilic runs show near-maximal non-monotonicity (`nonmonotone`: 2.00 (heterophilic))

Table 12. Network depth  $L$  effect on the learned spectral diagnostics. We report mean $\pm$ std across all models, stalk dimensions  $d \in \{2, 3, 4\}$  and seeds (3) for heterophilic (CHAMELEON, SQUIRREL) vs. homophilic (CITSEER, PUBMED) datasets.

$L$	$\alpha_{\text{hp}}$		$\Delta G$		# sign-changes	
	Hetero	Homo	Hetero	Homo	Hetero	Homo
2	-0.29 $\pm$ 0.09	-1.48 $\pm$ 0.17	0.50 $\pm$ 0.15	1.41 $\pm$ 0.30	2.00 $\pm$ 0.00	1.49 $\pm$ 0.57
3	-0.26 $\pm$ 0.09	-0.95 $\pm$ 0.32	0.46 $\pm$ 0.15	0.96 $\pm$ 0.31	2.00 $\pm$ 0.00	1.74 $\pm$ 0.51
4	-0.22 $\pm$ 0.09	-0.59 $\pm$ 0.34	0.36 $\pm$ 0.10	0.77 $\pm$ 0.28	2.00 $\pm$ 0.00	1.67 $\pm$ 0.62

Table 13. Stalk dimension  $d$  effect on the learned spectral diagnostics. We report mean $\pm$ std across all models, depths  $d \in \{2, 3, 4\}$  and seeds (3).

$d$	$\alpha_{\text{hp}}$		$\Delta G$		# sign-changes	
	Hetero	Homo	Hetero	Homo	Hetero	Homo
2	-0.30 $\pm$ 0.10	-1.03 $\pm$ 0.49	0.49 $\pm$ 0.15	1.06 $\pm$ 0.33	2.00 $\pm$ 0.00	1.76 $\pm$ 0.44
3	-0.27 $\pm$ 0.09	-0.96 $\pm$ 0.38	0.50 $\pm$ 0.16	1.04 $\pm$ 0.35	2.00 $\pm$ 0.00	1.57 $\pm$ 0.63
4	-0.20 $\pm$ 0.07	-1.03 $\pm$ 0.46	0.33 $\pm$ 0.09	1.05 $\pm$ 0.37	2.00 $\pm$ 0.00	1.56 $\pm$ 0.65

vs. 1.69 (homophilic) on average). Qualitatively, many heterophilic curves resemble mild band-pass shapes, aligning with the common observation that *heterophily benefits from more selective, higher-order spectral control* rather than repeated smoothing.

**Spectral response evolving with depth  $L$ : earned responses are less extreme as layers are stacked.** In Table 12, we aggregate the diagnostics per regime as a function of  $L$  (averaging across transport classes,  $d \in \{2, 3, 4\}$  and seeds). Here, increasing  $L$ : (i) makes  $\alpha_{\text{hp}}$  *less negative* (smaller magnitude) in both regimes, and (ii) reduces the low–high separation  $\Delta G$ , especially on homophilic datasets. This indicates that depth partly substitutes for explicit HP reinjection and strong spectral separation: as more PolyNSD layers are stacked, the learned response becomes less “extreme” at the ends of the spectrum, while heterophilic runs remain non-monotone for all  $L$ .

**Spectral response evolving with stalk dimension  $d$ : reduction of magnitude and separation.** In Table 13, we aggregate the diagnostics as a function of  $d$  (averaging across transport classes, depths  $L \in \{2, 3, 4\}$  and seeds). On homophilic datasets, the diagnostic statistics are comparatively *stable* across  $d$ , while for heterophilic datasets, instead, increasing  $d$  tends to reduce both the magnitude of  $\alpha_{\text{hp}}$  and the separation  $\Delta G$ . This result suggests a flatter (i.e., less contrastive) response when using wider stalks, indicating that, in heterophilic regimes, increasing fiber dimension can act as an additional degree of freedom that partially compensates for the strong spectral separation, whereas in homophilic regimes, the HP correction remains a dominant and robust mechanism irrespective of  $d$ .

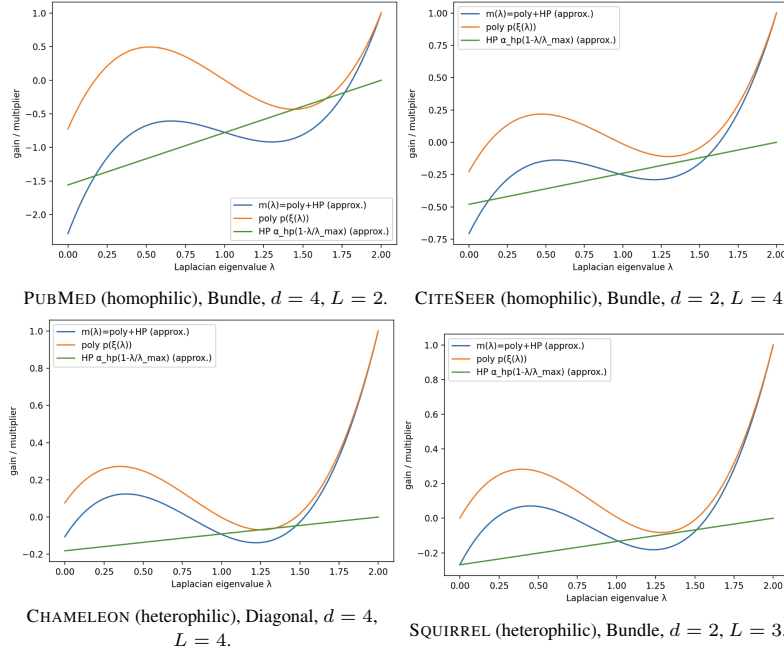
### C.9. Continuous-Time PolyNSD via Neural Sheaf ODEs

To confirm the model-agnostic claim, we extend the PolyNSD from discrete-time layers to *continuous-time* formulation in which sheaf diffusion is parameterised as a neural ordinary differential equation (ODE), following the Neural Sheaf Diffusion (NSD) model of (Bodnar et al., 2022). At the level of node features  $X(t) \in \mathbb{R}^{nd \times f}$ , NSD defines a time-evolving sheaf  $(G, \mathcal{F}(t))$  and a diffusion-type ODE of the form:  $\dot{X}(t) = -\sigma(\Delta_{\mathcal{F}(t)}(I_n \otimes W_1)X(t)W_2)$ , where  $\Delta_{\mathcal{F}(t)}$  is the (normalised) sheaf Laplacian at time  $t$ ,  $W_1, W_2$  are trainable weight matrices, and  $\sigma$  is a (typically 1-Lipschitz) nonlinearity. The restriction/transport maps and, hence,  $\Delta_{\mathcal{F}(t)}$  are obtained from the current features via a learnable parametrisation  $(G, \mathcal{F}(t)) = g(G, X(t); \theta)$ , so that both the geometry and the diffusion field evolve over time.

**From Discrete PolyNSD to PolyNSD ODEs.** Discrete PolyNSD layers replace the one-step NSD diffusion core  $aI + bL$  by a degree- $K$  spectral polynomial  $q_\theta(L)$  in a (normalised or unnormalised) sheaf Laplacian  $L$ , evaluated via a three-term recurrence on a spectrally rescaled operator  $L_e$ , and augmented with residual and high-pass terms (Section 3). In the continuous-time setting, we use the same sheaf prediction mechanism and polynomial filter to define the *infinitesimal* vector field of a neural sheaf ODE:

$$\dot{X}(t) = f_\theta(G, \mathcal{F}(t), X(t)) := -\sigma(q_\theta(\Delta_{\mathcal{F}(t)})(I_n \otimes W_1)X(t)W_2), \quad (102)$$

Figure 9. Spectral-response plots. Representative spectral response got for the 4 datasets, including the combined response  $m(\lambda)$ , the polynomial component and the HP correction term.



where  $q_\theta$  is a degree- $K$  polynomial in one variable (e.g. a convex combination of Chebyshev polynomials evaluated at  $L_e$ ). For fixed sheaf structure, linear activations and time-independent  $q_\theta$ , the ODE  $\dot{X}(t) = -q_\theta(\Delta_{\mathcal{F}}) X(t)$  has the closed-form solution  $X(T) = \exp(-T q_\theta(\Delta_{\mathcal{F}})) X(0)$ , so that each eigenmode with Laplacian eigenvalue  $\lambda$  is multiplied at time  $T$  by  $\exp(-T q_\theta(\lambda))$ . In this sense, continuous-time PolyNSD realises a *continuous-depth* sheaf diffusion whose spectral response is given by an exponential of a learnable polynomial in the sheaf spectrum, generalising the NSD case where  $q_\theta(\lambda)$  is effectively affine in  $\lambda$ .

**Continuous ODE Solvers.** In practice, we work with the same three transport classes as in the discrete setting, yielding the continuous families *Cont DiagChebySD*, *Cont BundleChebySD* and *Cont GeneralChebySD*. At each solver step, we: (i) use the current features  $X(t)$  to predict edge-wise restriction maps via a parametric function  $\Phi_\theta$ , yielding a sheaf  $(G, \mathcal{F}(t))$  and its Laplacian  $\Delta_{\mathcal{F}(t)}$ , (ii) construct the spectrally rescaled Laplacian  $L_e(t)$  and evaluate the polynomial  $q_\theta(L_e(t))$  via a stable three-term recurrence (with  $K$  sparse matrix–vector products), (iii) apply the diffusion field  $f_\theta$  in (102) and advance the state with a fixed-step ODE solver (integrating over a time horizon  $t \in [0, T]$  using a simple explicit method like the forward Euler or low-order Runge–Kutta).

**Depth, Spectral Control, and the Impact of PolyNSD in Continuous Time.** From a modelling perspective, the triple  $(K, T, N_{\text{steps}})$  jointly controls the effective depth and spectral behaviour of the continuous-time dynamics. The polynomial degree  $K$  determines the class of spectral generators  $q_\theta(\lambda)$  that can be realised: for  $K = 1$  we recover NSD-type generators  $a + b\lambda$ , whereas  $K > 1$  allows higher-order shaping of the sheaf spectrum. The integration horizon  $T$  scales the exponential factor  $\exp(-T q_\theta(\lambda))$ , thus modulating how quickly different frequencies are damped or preserved, and the numerical step size  $\Delta t$  trades off solver stability and approximation accuracy.

**Findings: PolyNSD continuous-time implementation reaches s.o.t.a. results.** Table 3 shows that introducing polynomial spectral control in the *continuous-time* setting is consistently beneficial, especially in heterophilic regimes, with the three proposed continuous PolyNSD variants (*Cont DiagChebySD*, *Cont BundleChebySD*, *Cont GeneralChebySD*) achieving *top-three* performance on most benchmarks. Compared to continuous NSD baselines, the improvements can be substantial in the most heterogeneous cases and this supports the interpretation that higher-order spectral generators  $q_\theta(\lambda)$  are particularly effective when the task requires mixing information across multiple neighbourhood radii rather than primarily smoothing. As for the discrete-time case, no single transport class dominates uniformly across all datasets, making the *diagonal* variant the preferred one once again, thanks to the important implicit savings it brings. This suggests that polynomial spectral

Table 14. Polynomial bases recurrences evaluated on the rescaled Laplacian  $\tilde{\mathbf{L}}$ .

Basis	Initialisation	Three-term recurrence ( $k \geq 1$ )
Chebyshev Type I $T_k$	$T_0(\tilde{\mathbf{L}})x = x, \quad T_1(\tilde{\mathbf{L}})x = \tilde{\mathbf{L}}x$	$T_{k+1}(\tilde{\mathbf{L}})x = 2\tilde{\mathbf{L}}T_k(\tilde{\mathbf{L}})x - T_{k-1}(\tilde{\mathbf{L}})x$
Chebyshev Type II $U_k$	$U_0(\tilde{\mathbf{L}})x = x, \quad U_1(\tilde{\mathbf{L}})x = 2\tilde{\mathbf{L}}x$	$U_{k+1}(\tilde{\mathbf{L}})x = 2\tilde{\mathbf{L}}U_k(\tilde{\mathbf{L}})x - U_{k-1}(\tilde{\mathbf{L}})x$
Chebyshev Type III $V_k$	$V_0(\tilde{\mathbf{L}})x = x, \quad V_1(\tilde{\mathbf{L}})x = (2\tilde{\mathbf{L}} - \mathbf{I})x$	$V_{k+1}(\tilde{\mathbf{L}})x = 2\tilde{\mathbf{L}}V_k(\tilde{\mathbf{L}})x - V_{k-1}(\tilde{\mathbf{L}})x$
Chebyshev Type IV $W_k$	$W_0(\tilde{\mathbf{L}})x = x, \quad W_1(\tilde{\mathbf{L}})x = (2\tilde{\mathbf{L}} + \mathbf{I})x$	$W_{k+1}(\tilde{\mathbf{L}})x = 2\tilde{\mathbf{L}}W_k(\tilde{\mathbf{L}})x - W_{k-1}(\tilde{\mathbf{L}})x$
Legendre $P_k$	$P_0(\tilde{\mathbf{L}})x = x, \quad P_1(\tilde{\mathbf{L}})x = \tilde{\mathbf{L}}x$	$P_{k+1}(\tilde{\mathbf{L}})x = \frac{2k+1}{k+1}\tilde{\mathbf{L}}P_k(\tilde{\mathbf{L}})x - \frac{k}{k+1}P_{k-1}(\tilde{\mathbf{L}})x$
Gegenbauer $C_k^{(\lambda)}$ ( $\lambda > 0$ )	$C_0^{(\lambda)}(\tilde{\mathbf{L}})x = x, \quad C_1^{(\lambda)}(\tilde{\mathbf{L}})x = 2\lambda\tilde{\mathbf{L}}x$	$C_{k+1}^{(\lambda)}(\tilde{\mathbf{L}})x = \frac{2(k+\lambda)}{k+1}\tilde{\mathbf{L}}C_k^{(\lambda)}(\tilde{\mathbf{L}})x - \frac{k+2\lambda-1}{k+1}C_{k-1}^{(\lambda)}(\tilde{\mathbf{L}})x$
Jacobi $P_k^{(\alpha,\beta)}$ ( $\alpha, \beta > -1$ )	$P_0^{(\alpha,\beta)}(\tilde{\mathbf{L}})x = x, \quad P_1^{(\alpha,\beta)}(\tilde{\mathbf{L}})x = c_1\tilde{\mathbf{L}}x + c_0x$	$P_{k+1}^{(\alpha,\beta)}(\tilde{\mathbf{L}})x = A_k\tilde{\mathbf{L}}P_k^{(\alpha,\beta)}(\tilde{\mathbf{L}})x + B_kP_k^{(\alpha,\beta)}(\tilde{\mathbf{L}})x - C_kP_{k-1}^{(\alpha,\beta)}(\tilde{\mathbf{L}})x, \quad \text{with:}$
		$A_k = \frac{2(k+1)(k+\alpha+\beta+1)}{(2k+\alpha+\beta+1)(2k+\alpha+\beta+2)}$
		$B_k = \frac{\beta^2 - \alpha^2}{(2k+\alpha+\beta)(2k+\alpha+\beta+2)}$
		$C_k = \frac{2(k+\alpha)(k+\beta)}{(2k+\alpha+\beta)(2k+\alpha+\beta+1)}$

control is complementary to the choice of transport class: the polynomial improves the *spectral expressivity* of the dynamics, while the transport class controls the *geometry* of information propagation.

### C.10. Alternative Orthogonal Polynomial Bases Used in PolyNSD

Our Polynomial Neural Sheaf Diffusion (PolyNSD) layers apply a spectral filter to a (sheaf) Laplacian  $\mathbf{L}$  via an orthogonal polynomial basis on the rescaled operator  $\tilde{\mathbf{L}}$ . Given a feature vector  $x \in \mathbb{R}^{N^d}$  (stacking fibers) and a family of orthogonal polynomials  $\{\Phi_k\}_{k \geq 0}$  on  $[-1, 1]$ , we define then the filter:  $p(\tilde{\mathbf{L}})x = \sum_{k=0}^K \alpha_k \Phi_k(\tilde{\mathbf{L}})x$ ,  $\alpha_k = \text{softmax}(\theta)_k$ , where  $\theta \in \mathbb{R}^{K+1}$  are learnable logits and  $\alpha_k$  form a convex mixture of the basis responses. All bases are implemented via stable three-term recurrences directly on vectors  $v \mapsto \Phi_k(\tilde{\mathbf{L}})v$ . We therefore experiment over multiple solutions in here, as listed in Table 14.

**Findings: Alternative orthogonal bases yield consistent performance, with Chebyshev as a strong default.** Table 15 show that PolyNSD is *robust* to the specific choice of orthogonal polynomial basis: across transport classes (Diagonal / Bundle / General) and datasets spanning the homophily–heterophily spectrum, most bases attain performances that are close to the Chebyshev Type I default, confirming that the main gains come from *higher-order spectral control* rather than from a single privileged basis. These results confirm that PolyNSD is *basis-agnostic* and the key ingredient is the ability to learn a bounded degree- $K$  spectral multiplier on the rescaled sheaf Laplacian via stable recurrences. Chebyshev Type I offers the most consistent default, but alternative orthogonal bases provide a viable design space for tailoring approximation properties without changing the PolyNSD layer structure.

Table 15. Extended PolyNSD discrete node classification benchmark results. We report the accuracy  $\pm$  stdev on node classification datasets, ordered by increasing homophily. Our techniques are denoted in **bold**. The first section includes Sheaf Neural Networks models, while the second includes other GNN models. The top three models for each dataset are coloured by **First**, **Second** and **Third**, respectively.

	Texas	Wisconsin	Film	Squirrel	Chameleon	Cornell	Citeseer	Pubmed	Cora
<i>Homophily level</i>	<b>0.11</b>	<b>0.21</b>	<b>0.22</b>	<b>0.22</b>	<b>0.23</b>	<b>0.30</b>	<b>0.74</b>	<b>0.80</b>	<b>0.81</b>
#Nodes	183	251	7,600	5,201	2,277	183	3,327	18,717	2,708
#Edges	295	466	26,752	198,493	31,421	280	4,676	44,327	5,278
#Classes	5	5	5	5	5	5	7	3	6
<b>DiagChebyT1SD</b>	88.68 $\pm$ 3.12	87.84 $\pm$ 4.45	37.14 $\pm$ 1.26	<b>56.61<math>\pm</math>2.06</b>	70.41 $\pm$ 2.47	<b>86.49<math>\pm</math>5.54</b>	<b>77.74<math>\pm</math>1.26</b>	89.67 $\pm$ 0.34	<b>88.67<math>\pm</math>1.29</b>
<b>BundleChebyT1SD</b>	<b>89.74<math>\pm</math>5.32</b>	87.65 $\pm$ 3.29	37.47 $\pm$ 0.86	54.33 $\pm$ 2.67	69.29 $\pm$ 1.88	85.40 $\pm$ 7.94	77.57 $\pm$ 1.55	<b>89.75<math>\pm</math>0.34</b>	88.12 $\pm$ 1.35
<b>GeneralChebyT1SD</b>	88.94 $\pm$ 4.53	88.23 $\pm$ 4.56	37.20 $\pm$ 0.77	53.88 $\pm$ 1.65	67.34 $\pm$ 2.45	<b>86.49<math>\pm</math>5.80</b>	77.10 $\pm$ 1.30	89.73 $\pm$ 0.41	88.47 $\pm$ 1.19
<b>DiagChebyT2SD</b>	88.68 $\pm$ 5.27	88.23 $\pm$ 3.40	36.98 $\pm$ 0.71	51.20 $\pm$ 3.16	71.01 $\pm$ 2.57	85.95 $\pm$ 5.38	77.42 $\pm$ 1.80	89.60 $\pm$ 0.44	88.49 $\pm$ 1.34
<b>BundleChebyT2SD</b>	88.42 $\pm$ 6.25	88.23 $\pm$ 3.28	37.14 $\pm$ 1.17	52.30 $\pm$ 2.01	67.67 $\pm$ 1.80	86.22 $\pm$ 7.69	77.56 $\pm$ 1.66	89.57 $\pm$ 0.54	88.17 $\pm$ 1.20
<b>GeneralChebyT2SD</b>	88.42 $\pm$ 4.74	87.84 $\pm$ 3.90	37.00 $\pm$ 1.03	51.34 $\pm$ 1.35	67.00 $\pm$ 2.38	85.68 $\pm$ 4.53	77.21 $\pm$ 1.58	89.62 $\pm$ 0.28	88.03 $\pm$ 1.11
<b>DiagChebyT3SD</b>	88.68 $\pm$ 7.07	87.45 $\pm$ 4.74	36.99 $\pm$ 1.13	53.28 $\pm$ 1.71	70.09 $\pm$ 2.75	85.40 $\pm$ 5.16	77.43 $\pm$ 1.54	89.67 $\pm$ 0.37	88.37 $\pm$ 1.40
<b>BundleChebyT3SD</b>	88.95 $\pm$ 4.37	88.43 $\pm$ 4.51	37.31 $\pm$ 0.93	55.48 $\pm$ 2.84	67.70 $\pm$ 1.21	85.95 $\pm$ 6.71	77.31 $\pm$ 1.23	89.62 $\pm$ 0.34	88.05 $\pm$ 1.49
<b>GeneralChebyT3SD</b>	89.21 $\pm$ 5.05	88.23 $\pm$ 3.16	37.00 $\pm$ 1.06	<b>55.79<math>\pm</math>2.52</b>	66.49 $\pm$ 1.94	84.59 $\pm$ 5.80	77.03 $\pm$ 1.33	89.51 $\pm$ 0.32	87.99 $\pm$ 1.56
<b>DiagChebyT4SD</b>	<b>90.00<math>\pm</math>4.68</b>	88.04 $\pm$ 2.70	37.31 $\pm$ 0.98	54.27 $\pm$ 1.99	<b>71.45<math>\pm</math>2.03</b>	85.68 $\pm$ 5.54	77.50 $\pm$ 1.54	89.64 $\pm$ 0.34	<b>88.79<math>\pm</math>1.13</b>
<b>BundleChebyT4SD</b>	89.21 $\pm$ 4.15	88.43 $\pm$ 2.97	37.05 $\pm$ 1.12	53.23 $\pm$ 1.52	67.34 $\pm$ 1.49	85.40 $\pm$ 6.42	77.09 $\pm$ 1.76	89.62 $\pm$ 0.35	87.99 $\pm$ 1.21
<b>GeneralChebyT4SD</b>	88.16 $\pm$ 5.30	88.04 $\pm$ 4.92	37.31 $\pm$ 0.98	53.60 $\pm$ 2.92	69.62 $\pm$ 1.85	84.86 $\pm$ 6.86	76.58 $\pm$ 1.72	89.63 $\pm$ 0.29	87.54 $\pm$ 1.84
<b>DiagChebyInterpSD</b>	<b>89.74<math>\pm</math>4.05</b>	87.45 $\pm$ 3.74	36.89 $\pm$ 0.70	54.45 $\pm$ 3.47	68.46 $\pm$ 3.11	85.67 $\pm$ 5.54	<b>77.60<math>\pm</math>1.75</b>	89.70 $\pm$ 0.32	88.63 $\pm$ 1.09
<b>BundleChebyInterpSD</b>	88.95 $\pm$ 4.04	88.04 $\pm$ 3.56	36.92 $\pm$ 0.72	55.02 $\pm$ 2.32	70.02 $\pm$ 2.11	86.21 $\pm$ 7.09	77.34 $\pm$ 1.72	89.66 $\pm$ 0.41	88.33 $\pm$ 1.34
<b>GeneralChebyInterpSD</b>	88.43 $\pm$ 3.76	87.84 $\pm$ 4.45	37.23 $\pm$ 0.59	52.75 $\pm$ 6.60	67.37 $\pm$ 2.65	85.95 $\pm$ 6.14	77.03 $\pm$ 2.21	89.72 $\pm$ 0.26	88.11 $\pm$ 1.23
<b>DiagLegendreSD</b>	89.47 $\pm$ 4.99	88.43 $\pm$ 4.15	37.20 $\pm$ 0.55	51.88 $\pm$ 2.61	70.35 $\pm$ 2.30	85.40 $\pm$ 6.86	77.53 $\pm$ 1.57	89.70 $\pm$ 0.48	<b>88.65<math>\pm</math>1.17</b>
<b>BundleLegendreSD</b>	88.95 $\pm$ 4.04	<b>89.41<math>\pm</math>4.04</b>	37.29 $\pm$ 0.84	51.65 $\pm$ 1.83	<b>71.18<math>\pm</math>1.46</b>	84.86 $\pm$ 4.22	77.49 $\pm$ 1.46	89.61 $\pm$ 0.32	88.27 $\pm$ 1.38
<b>GeneralLegendreSD</b>	89.21 $\pm$ 5.05	88.63 $\pm$ 2.88	37.34 $\pm$ 1.13	51.97 $\pm$ 1.98	68.95 $\pm$ 2.37	85.40 $\pm$ 6.96	76.85 $\pm$ 1.69	87.72 $\pm$ 0.32	87.89 $\pm$ 1.12
<b>DiagGagenbauerSD</b>	89.21 $\pm$ 4.77	87.65 $\pm$ 3.72	37.06 $\pm$ 1.16	52.97 $\pm$ 4.69	70.39 $\pm$ 4.31	85.68 $\pm$ 5.54	77.23 $\pm$ 1.83	89.61 $\pm$ 0.32	88.63 $\pm$ 1.81
<b>BundleGagenbauerSD</b>	88.95 $\pm$ 5.10	87.65 $\pm$ 3.93	36.99 $\pm$ 1.12	49.81 $\pm$ 1.35	69.87 $\pm$ 2.02	<b>86.76<math>\pm</math>4.90</b>	77.43 $\pm$ 1.54	89.61 $\pm$ 0.44	88.33 $\pm$ 1.44
<b>GeneralGagenbauerSD</b>	88.68 $\pm$ 3.73	88.04 $\pm$ 3.22	37.20 $\pm$ 0.80	49.47 $\pm$ 1.47	66.25 $\pm$ 2.29	85.13 $\pm$ 6.54	77.18 $\pm$ 1.72	89.67 $\pm$ 0.35	87.85 $\pm$ 0.99
<b>DiagJacobiSD</b>	88.68 $\pm$ 6.23	88.63 $\pm$ 3.59	37.03 $\pm$ 0.72	52.30 $\pm$ 0.93	66.14 $\pm$ 1.50	86.22 $\pm$ 5.05	77.35 $\pm$ 1.43	89.09 $\pm$ 0.89	88.53 $\pm$ 1.02
<b>BundleJacobiSD</b>	88.95 $\pm$ 4.96	88.82 $\pm$ 3.83	37.18 $\pm$ 0.97	55.76 $\pm$ 2.02	68.22 $\pm$ 1.42	85.68 $\pm$ 5.68	76.97 $\pm$ 1.74	89.72 $\pm$ 0.48	88.13 $\pm$ 1.19
<b>GeneralJacobiSD</b>	88.68 $\pm$ 5.14	88.82 $\pm$ 4.89	37.03 $\pm$ 0.95	52.30 $\pm$ 1.30	66.62 $\pm$ 1.07	85.68 $\pm$ 3.83	76.80 $\pm$ 1.68	89.53 $\pm$ 0.46	87.66 $\pm$ 1.26
<b>PolySpectralGNN</b>	64.59 $\pm$ 6.40	58.62 $\pm$ 6.04	25.50 $\pm$ 0.85	51.72 $\pm$ 1.76	62.65 $\pm$ 3.03	54.59 $\pm$ 6.26	60.44 $\pm$ 0.89	78.7 $\pm$ 0.56	76.2 $\pm$ 0.67
RiSNN - NoT	87.89 $\pm$ 4.28	88.04 $\pm$ 2.39	N/A	51.24 $\pm$ 1.71	66.58 $\pm$ 1.81	82.97 $\pm$ 6.17	75.07 $\pm$ 1.56	87.91 $\pm$ 0.55	85.86 $\pm$ 1.31
RiSNN	86.84 $\pm$ 3.72	87.84 $\pm$ 2.60	N/A	53.30 $\pm$ 3.30	65.15 $\pm$ 2.40	85.95 $\pm$ 6.14	76.23 $\pm$ 1.81	88.00 $\pm$ 0.42	85.27 $\pm$ 1.11
JdSNN - NoW	87.30 $\pm$ 4.53	88.43 $\pm$ 2.83	N/A	51.28 $\pm$ 1.80	66.45 $\pm$ 3.46	84.59 $\pm$ 6.95	75.93 $\pm$ 1.41	88.09 $\pm$ 0.49	84.39 $\pm$ 1.47
JdSNN	87.37 $\pm$ 5.10	<b>89.22<math>\pm</math>3.42</b>	N/A	49.89 $\pm$ 1.71	66.40 $\pm$ 2.33	85.41 $\pm$ 4.55	73.27 $\pm$ 1.86	88.19 $\pm$ 0.55	85.43 $\pm$ 1.73
Conn - NSD	86.16 $\pm$ 2.24	88.73 $\pm$ 4.47	<b>37.91<math>\pm</math>1.28</b>	45.19 $\pm$ 1.57	65.21 $\pm$ 2.04	85.95 $\pm$ 7.72	75.61 $\pm$ 1.93	89.28 $\pm$ 0.38	83.74 $\pm$ 2.19
SAN	84.05 $\pm$ 5.33	86.47 $\pm$ 3.87	37.09 $\pm$ 1.18	50.96 $\pm$ 1.40	67.46 $\pm$ 1.90	84.32 $\pm$ 5.64	72.57 $\pm$ 1.50	87.12 $\pm$ 0.30	85.90 $\pm$ 1.85
ANSD	85.68 $\pm$ 4.69	87.45 $\pm$ 3.19	37.66 $\pm$ 1.40	54.39 $\pm$ 1.76	68.38 $\pm$ 2.14	84.59 $\pm$ 5.93	76.81 $\pm$ 1.82	89.21 $\pm$ 0.37	87.20 $\pm$ 1.03
Diag - NSD	85.67 $\pm$ 6.95	88.63 $\pm$ 2.75	37.79 $\pm$ 1.01	54.78 $\pm$ 1.81	68.68 $\pm$ 1.73	86.49 $\pm$ 7.35	77.14 $\pm$ 1.85	89.42 $\pm$ 0.43	87.14 $\pm$ 1.06
O(d) - NSD	85.95 $\pm$ 5.51	<b>89.41<math>\pm</math>4.74</b>	<b>37.81<math>\pm</math>1.15</b>	<b>56.34<math>\pm</math>1.32</b>	68.04 $\pm$ 1.58	84.86 $\pm$ 4.71	76.70 $\pm$ 1.57	89.49 $\pm$ 0.40	86.90 $\pm$ 1.13
Gen - NSD	82.97 $\pm$ 5.13	89.21 $\pm$ 3.84	<b>37.80<math>\pm</math>1.22</b>	53.17 $\pm$ 1.31	67.93 $\pm$ 1.58	85.68 $\pm$ 6.51	76.32 $\pm$ 1.65	89.33 $\pm$ 0.35	87.30 $\pm$ 1.15
GGCN	84.86 $\pm$ 4.55	86.86 $\pm$ 3.29	37.54 $\pm$ 1.56	55.17 $\pm$ 1.58	<b>71.14<math>\pm</math>1.84</b>	85.68 $\pm$ 6.63	77.14 $\pm$ 1.45	89.15 $\pm$ 0.37	87.95 $\pm$ 1.05
H2GCN	84.86 $\pm$ 7.23	87.65 $\pm$ 4.98	35.70 $\pm$ 1.00	36.48 $\pm$ 1.86	60.11 $\pm$ 2.15	82.70 $\pm$ 5.28	77.11 $\pm$ 1.57	89.49 $\pm$ 0.38	87.87 $\pm$ 1.20
GPRGNN	78.38 $\pm$ 4.36	82.94 $\pm$ 4.21	34.63 $\pm$ 1.22	31.61 $\pm$ 1.24	46.58 $\pm$ 1.71	80.27 $\pm$ 8.11	77.13 $\pm$ 1.67	87.54 $\pm$ 0.38	87.95 $\pm$ 1.18
FAGCN	82.43 $\pm$ 6.89	82.94 $\pm$ 7.95	34.87 $\pm$ 1.25	42.59 $\pm$ 0.79	55.22 $\pm$ 3.19	79.19 $\pm$ 9.79	N/A	N/A	N/A
MixHop	77.84 $\pm$ 7.73	75.88 $\pm$ 4.90	32.22 $\pm$ 2.34	48.30 $\pm$ 1.48	60.50 $\pm$ 2.53	73.51 $\pm$ 6.34	76.26 $\pm$ 1.33	85.31 $\pm$ 0.61	87.61 $\pm$ 0.85
GCNII	77.57 $\pm$ 3.83	80.39 $\pm$ 3.40	37.44 $\pm$ 1.30	38.47 $\pm$ 1.58	63.86 $\pm$ 3.04	77.86 $\pm$ 3.79	77.33 $\pm$ 1.48	<b>90.15<math>\pm</math>0.43</b>	88.37 $\pm$ 1.25
Geom - GCN	66.76 $\pm$ 2.72	64.51 $\pm$ 3.66	31.59 $\pm$ 1.15	38.15 $\pm$ 0.92	60.00 $\pm$ 2.81	60.54 $\pm$ 3.67	<b>78.02<math>\pm</math>1.15</b>	<b>89.95<math>\pm</math>0.47</b>	85.35 $\pm$ 1.57
PairNorm	60.27 $\pm$ 4.34	48.43 $\pm$ 6.14	27.40 $\pm$ 1.24	50.44 $\pm$ 2.04	62.74 $\pm$ 2.82	58.92 $\pm$ 3.15	73.59 $\pm$ 1.47	87.53 $\pm$ 0.44	85.79 $\pm$ 1.01
GraphSAGE	82.43 $\pm$ 6.14	81.18 $\pm$ 5.56	34.23 $\pm$ 0.99	41.61 $\pm$ 0.74	58.73 $\pm$ 1.68	75.95 $\pm$ 5.01	76.04 $\pm$ 1.30	88.45 $\pm$ 0.50	86.90 $\pm$ 1.04
GCN	55.14 $\pm$ 5.16	51.76 $\pm$ 3.06	27.32 $\pm$ 1.10	53.43 $\pm$ 2.01	64.82 $\pm$ 2.24	60.54 $\pm$ 5.30	76.50 $\pm$ 1.36	88.42 $\pm$ 0.50	86.98 $\pm$ 1.27
GAT	52.16 $\pm$ 6.63	49.41 $\pm$ 4.09	27.44 $\pm$ 0.89	40.72 $\pm$ 1.55	60.26 $\pm$ 2.50	61.89 $\pm$ 5.05	76.55 $\pm$ 1.23	87.30 $\pm$ 1.10	86.33 $\pm$ 0.48
MLP	80.81 $\pm$ 4.75	85.29 $\pm$ 3.31	36.53 $\pm$ 0.70	28.77 $\pm$ 1.56	46.21 $\pm$ 2.99	81.89 $\pm$ 6.40	74.02 $\pm$ 1.90	75.69 $\pm$ 2.00	87.16 $\pm$ 0.37

### C.11. Synthetic Benchmarks: Heterophily, Scalability, and Noise

In this subsection, we detail synthetic experiments that underpin the synthetic stress tests discussed in Table 4. All experiments use the synthetic data-generation procedure described in subsection C.2.1.

*Heterophily Sweeps.* To probe performance under controlled heterophily, we vary the heterophily coefficient  $het \in \{0, 0.25, 0.5, 0.75, 1\}$ , while keeping all other graph and feature parameters fixed. We consider both synthetic regimes introduced in (Caralt et al., 2024): (i) RiSNN-style: higher-dimensional features and a configuration mirroring the RiSNN experiments, and (ii) DIFF-style: lower-dimensional features and a configuration mirroring the diffusion-style experiments. For each regime we evaluate multiple class counts and average results over 5 synthetic graph realisations per configuration. We compare PolyNSD variants against MLP, GCN, VanillaSheaf, simple sheaf baselines, and the

RiSNN/JdSNN architectures. Figure 10 summarises the results as a  $4 \times 2$  grid (rows correspond to different numbers of classes, columns to the two synthetic regimes). Within each subplot, we plot test accuracy vs. *het* for all models. As heterophily increases, homophily-biased message passing (e.g., GCN) rapidly degrades towards MLP performance, confirming that edges become uninformative or adversarial. Sheaf-based models are more robust, and PolyNSD variants consistently occupy the top of the accuracy curves across all *het* values, especially in the bundle and general transport classes. This confirm the real-world findings in Table 4 under controlled conditions.

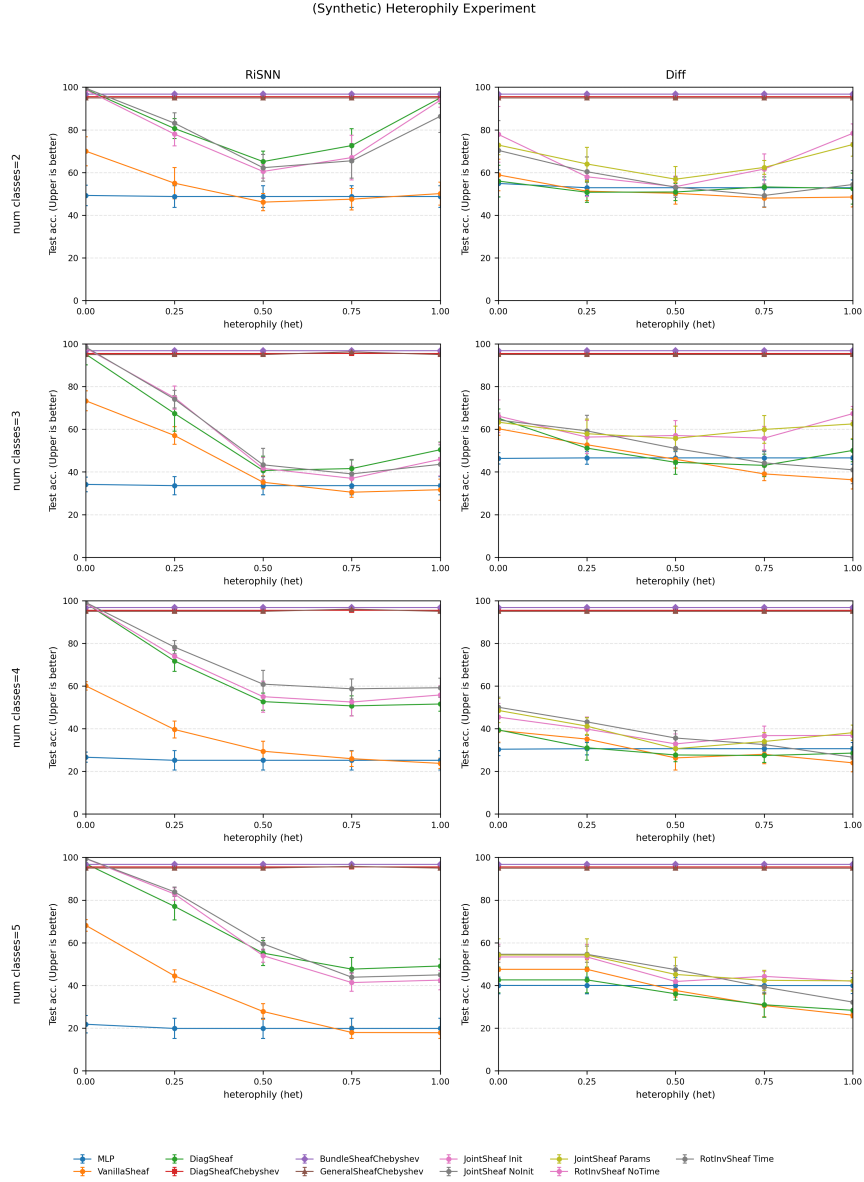


Figure 10. Synthetic heterophily sweeps. Each row corresponds to a different number of classes; columns distinguish the RiSNN and DIFF regimes. We sweep  $het \in \{0, 0.25, 0.5, 0.75, 1.0\}$ ; error bars show mean $\pm$ std over multiple random graph realisations.

**Data Scalability.** To study how PolyNSD scales with graph size and degree, we jointly vary the number of nodes  $N \in \{100, 500, 1000\}$  and the base degree  $K \in \{2, 6, 10\}$ , while keeping heterophily fixed at a high value ( $het = 0.9$ ). This setting acts as a stress test where edges are mostly cross-class and graphs become denser as  $K$  grows. For each  $(N, K)$  pair we generate a new synthetic graph in both the RiSNN and DIFF regimes and evaluate all models using the same training protocol as before. Figure 11 depicts the results as a grid with rows indexed by  $N$  and columns by  $K$ . Each subplot reports test accuracy for PolyNSD variants and baselines. Across both regimes, PolyNSD variants maintain near-saturated

## Polynomial Neural Sheaf Diffusion: A Spectral Filtering Approach on Cellular Sheaves

performance (often close to 98%) across all scales, whereas baseline methods improve more slowly or plateau at lower accuracies as  $N$  and  $K$  increase, indicating that PolyNSD scales favourably with both the number of nodes and edge density, and that its polynomial filters remain effective even as graphs become larger and more connected.

(Synthetic) Data Scalability Ablation Study

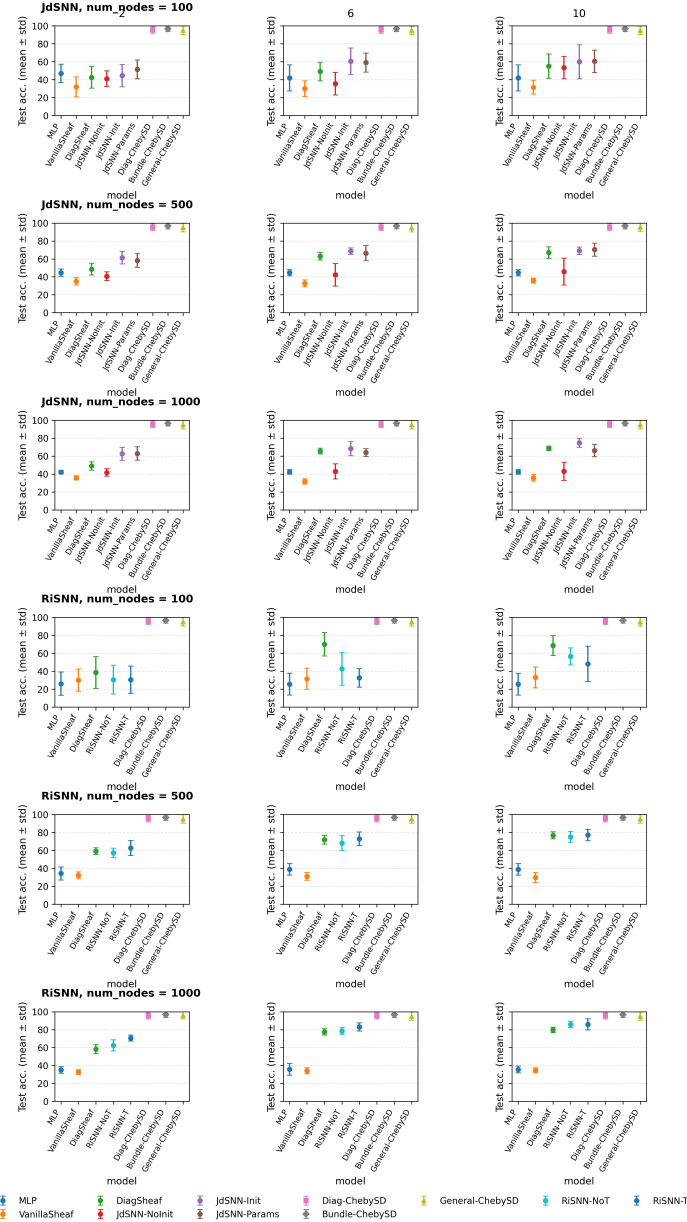


Figure 11. Data scalability ablation. Rows correspond to increasing number of nodes  $N \in \{100, 500, 1000\}$ ; columns to degree  $K \in \{2, 6, 10\}$  at fixed high heterophily  $het = 0.9$ . Top block: DIFF setup; bottom block: RiSNN setup. PolyNSD maintains near-saturated performance across scales, while baselines plateau at lower accuracies.

*Effect of Feature Noise.* Finally, we examine robustness to feature corruption by injecting i.i.d. Gaussian noise into node features while keeping the underlying graphs maximally heterophilous ( $het = 1$ ). This setting isolates the

effect of covariate noise from that of connectivity. We consider two noise sweeps: for the DIFF-style setup, we vary  $\text{feat\_noise} \in \{0.0, 0.2, 0.4, 0.6, 0.8, 1.0\}$ , while for the RISNN-style setup, we use finer-grained noise levels  $\text{feat\_noise} \in \{0.00, 0.05, 0.10, 0.15, 0.20, 0.25\}$ . For each noise level we generate multiple synthetic instances and average test accuracy over these realisations. Figure 12 summarises the results. As noise increases, GCN and other homophily-based message-passing models degrade rapidly, eventually approaching the performance of an MLP that ignores the graph. Sheaf-based models are more robust, and PolyNSD variants are consistently among the best-performing methods across all noise levels. The bundle and general transport classes, combined with spectral control, show the strongest robustness, retaining significant accuracy even at the highest noise levels. These findings support the interpretation of PolyNSD as a *structure-aware denoiser*: the sheaf transports align features in local fibres before comparison, while the spectral polynomial can attenuate high-frequency noise modes and preserve informative low- and mid-frequency components.

(Synthetic) Noise Effect Ablation Study

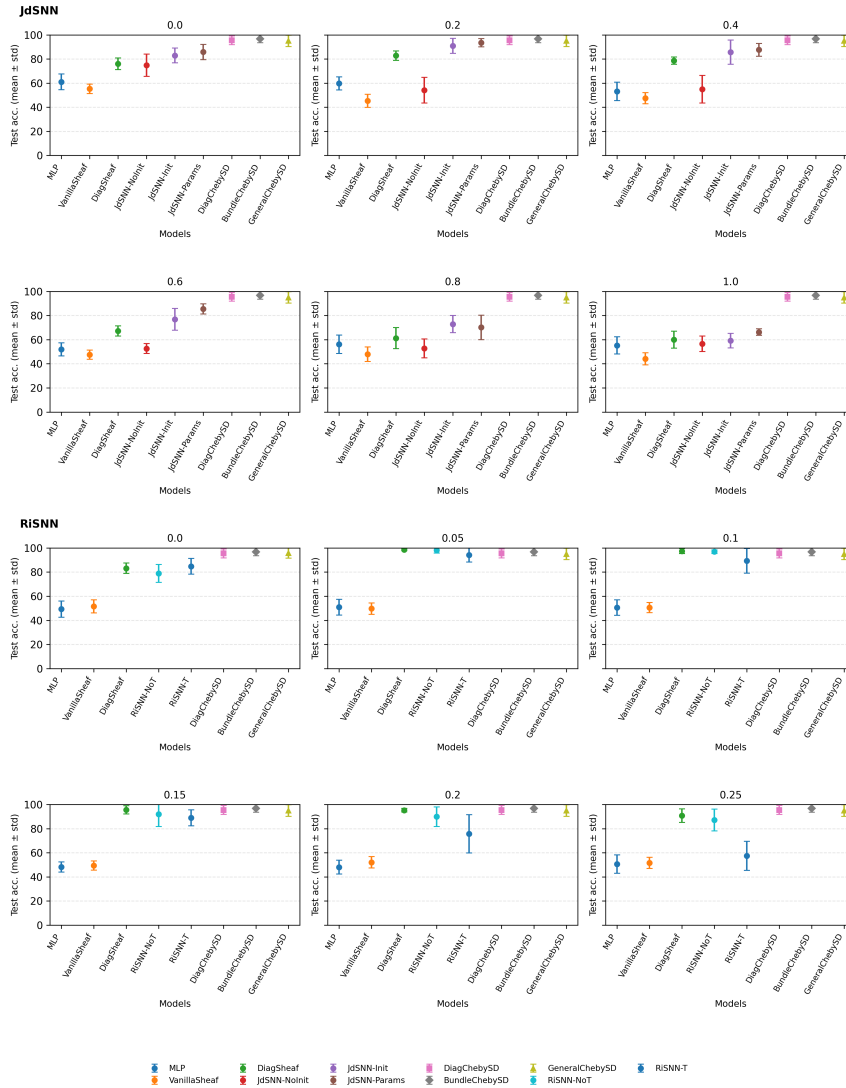


Figure 12. Effect of feature noise on synthetic tasks. Top two rows: DIFF-style setup with noise levels  $\{0.0, 0.2, 0.4, 0.6, 0.8, 1.0\}$ . Bottom two rows: RISNN-style setup with noise levels  $\{0.00, 0.05, 0.10, 0.15, 0.20, 0.25\}$ . PolyNSD variants remain among the most robust models, degrading more slowly and exhibiting smaller variance than baselines.